PHASE TRANSITIONS IN LIVING NEURAL NETWORKS

Rashid Vladimir Williams-García

Submitted to the faculty of the University Graduate School

in partial fulfillment of the requirements

for the degree

Doctor of Philosophy

in the Department of Physics,

Indiana University Bloomington

July 2016

Accepted by the Graduate Faculty, Indiana University, in partial fulfillment of the requirements for the degree of Doctor of Philosophy.

Doctoral Committee

John M. Beggs, Ph.D.

Gerardo Ortiz, Ph.D.

Robert de Ruyter van Steveninck, Ph.D.

Jorge V. José, Ph.D.

July 1, 2016

Copyright © 2016

Rashid Vladimir Williams-García

To my father, Marshall L. Williams (1941-2004), a mathematician, computer scientist, educator, and lifelong advocate for the underprivileged. Through great effort and sacrifice, he established the foundations on which I am now building my career. Among other things, he introduced me to the ideas of general systems theory and cybernetics, which greatly influenced my research and academic interests. He taught me to treat everything in life as a learning experience and to seek criticism to grow. Without him and his guidance, none of my accomplishments would have ever been possible.

> "We do not learn for school, but for life."
>
> – Lucius Annaeus Seneca

ACKNOWLEDGMENTS

I would like to recognize the contributions of the many people who have aided me throughout the years and made my dissertation possible. I am grateful to my undergraduate institution, the Department of Physics & Astronomy at the University of California, Los Angeles (UCLA) as well as my advisors there: Prof. Dolores Bozovic, Prof. George Grüner, Prof. James Rosenzweig, and Françoise Quéval, my undergraduate academic coordinator. Another warm acknowledgment goes to Prof. Stuart Brown, who first introduced me to condensed matter physics and whose contagious enthusiasm for the topic has remained with me all these years. To my classmates at UCLA, the members of the "Physics Rogue Squad", Gerardo Alvarado, Michael Erickson, Dr. Sean Huver, Daniel Maronde, and Alfonso Vergara, with whom I shared many evenings fraught with Prof. Per Kraus' quantum mechanics problems. A particularly warm acknowledgment goes to my long-time friend and blood brother, Dr. Alfonse N. Pham, whom I first met at UCLA and whose continuing friendship and loyalty have enriched my life throughout the years. I owe a great debt to Prof. Richard L. Weiss at the UCLA Department of Chemistry & Biochemistry, who advised me as a post-baccalaureate researcher under the National Institutes of Health's Post-baccalaureate Research and Education Program, and went above and beyond to help resolve a difficult housing situation.

At Indiana University Bloomington (IUB), I am grateful first to Rita DuCharme who, shortly after my move to Bloomington, surprised me by buying me a number of the books I continue to use for my research to this day. Next, I am grateful to Prof. James Glazier

from the IUB Department of Physics and the Biocomplexity Institute for their years of funding and to Prof. Robert de Ruyter van Steveninck who provided a year's worth of research funding. To Prof. John M. Beggs, whose straightforward explanations and deep understanding helped ease me into the world of neuroscience research, and who provided me the opportunity to work in his lab and encouraged me in all my efforts throughout the years. While in Prof. Beggs' lab, I was assisted by my undergraduate assistants, Rachel Pauplis and Dr. Sukriti Bansal, in the daily lab routine and I thank them immensely for their efforts. I would also like to acknowledge Dr. Marta S. Shocket, at the time a graduate student at the IUB Department of Biology, who provided her valuable expertise in applying various statistical methods in analyzing experimental data. A special thanks goes to my colleagues in the Beggs lab: Dr. Emily Miller, Ben Nicholson, Dr. Sunny Nigam, and Zach Tosi. To Edward J. Timko III for illuminating discussions on various mathematical topics throughout our time as roommates. And to Prof. Kevin M. Pilgrim from the IUB Department of Mathematics, with whom I collaborated on working to understand the behavior of my discrete map. Finally, my warmest thanks go to Prof. Gerardo Ortiz who tutored and mentored me in frequent one-on-one meetings and in joint meetings with Prof. Beggs, where he shared his often illuminating perspective. He provided indispensable guidance, motivation, and inspiration which has undoubtedly shaped my development as a researcher. It was through his keen insights that I finally discovered my place in the scientific community. I am grateful for the experiences and opportunities I have had in my academic career and hope continue working with such brilliant researchers as John and Gerardo for many years to come.

Rashid Vladimir Williams-García

PHASE TRANSITIONS IN LIVING NEURAL NETWORKS

Our nervous systems are composed of intricate webs of interconnected neurons interacting in complex ways. These complex interactions result in a wide range of collective behaviors with implications for features of brain function, e.g., information processing. Under certain conditions, such interactions can drive neural network dynamics towards critical phase transitions, where power-law scaling is conjectured to allow optimal behavior. Recent experimental evidence is consistent with this idea and it seems plausible that healthy neural networks would tend towards optimality. This hypothesis, however, is based on two problematic assumptions, which I describe and for which I present alternatives in this thesis. First, critical transitions may vanish due to the influence of an environment, e.g., a sensory stimulus, and so living neural networks may be incapable of achieving "critical" optimality. I develop a framework known as quasicriticality, in which a relative optimality can be achieved depending on the strength of the environmental influence. Second, the power-law scaling supporting this hypothesis is based on statistical analysis of cascades of activity known as neuronal avalanches, which conflate causal and non-causal activity, thus confounding important dynamical information. In this thesis, I present a new method to unveil causal links, known as causal webs, between neuronal activations, thus allowing for experimental tests of the quasicriticality hypothesis and other practical applications.

CONTENTS

1 Introduction **1**

2 Elements of Phase Transitions **19**

2.1 Equilibrium Transitions: The Ising Model 21

2.1.1 A Mean-Field Approximation 22

2.1.2 Landau Theory 27

2.2 Nonequilibrium Transitions: Directed Percolation 30

2.2.1 Mean-Field Directed Percolation 32

3 Self-Organized Criticality **35**

3.1 The Bak-Tang-Wiesenfeld Model 36

3.1.1 The Random-Neighbor Mean-Field Approximation 37

3.2 The Cortical Branching Model 38

3.2.1 Formal Description 39

3.2.2 Cellular Automata Rules 42

3.2.3 Avalanche Shape 44

3.2.4 Avalanche Branching Ratio 45

3.3 A Mean-Field Approximation of the CBM 46

4 The Quasicriticality Hypothesis **54**

4.1 The Strongly-Driven CBM 55

4.1.1 Quasicriticality in the Mean-Field CBM 56
4.1.2 The Nonequilibrium Widom Line 57
4.1.3 Simulation of Avalanche Physics 57
4.1.4 Optimal Information Transmission and the Widom Line 62

5 Causal Webs: Unveiling Dynamical Correlations 67

5.1 Mathematical Formalism 68
5.2 Tests of the Method 71
5.3 Determining the Network Structure: Transfer Entropy 72
5.4 Application to Experimental Data 77
5.5 Graphical Representations of Causal Webs 82

6 Conclusions and Outlook 85

6.1 The Quasicriticality Hypothesis 85
6.1.1 The Quasiperiodic Phase 87
6.2 Generalized CBMs 88
6.2.1 Network Structure 89
6.2.2 Neuronal Heterogeneity 90
6.3 Beyond the Mean Field 92
6.4 Impact and Potential Applications of Causal Webs 93

A Simulation and C-Web Algorithm Codes 96

A.1 MATLAB Cortical Branching Model Code 96
A.2 MATLAB Causal Webs Algorithm Code 101

B On the Quasiperiodic Phase of the CBM 107

B.1 Rouché's Theorem 107
B.2 Center Manifold Theorem 109

B.3 Expansion Entropy 113

C The Strongly-Driven BTW Model 115

D Sudden Quench Dynamics 116

E Generalized Cortical Branching Models 123

E.1 The Delayed-Transmission CBM 124

E.2 The Excitatory/Inhibitory CBM 125

E.2.1 Site Inhibition 126

E.2.2 Bond Inhibition 131

F Analysis of Somatosensory Cortex Data 134

G Generation of Biologically-Inspired Networks 138

Bibliography 140

Curriculum Vitae

CHAPTER 1

Introduction

In the universe, heterogeneity, disorder, and complexity reign supreme, and our brains are no exception. There are on the order of 100 billion specialized cells, known as **neurons**, bustling with activity in the human brain. Each of these neurons is connected via **synapses** to on the order of 10 thousand other neurons[1], with which they share information, as you might expect in a social network[1]. For the average adult human, this means nearly a quadrillion (i.e., 10^{15}) synapses. The brain is quite possibly the most complex organ in the human body and the electrically-excitable neurons which operate within it are also complex, belonging to a number of different neuron classes distinguished by differences in structure, function, and morphology. The brain is a **complex system**.

Although no standard definition exists, complex systems tend to involve large numbers of heterogeneous, interconnected components interacting in non-trivial ways (e.g., via threshold interactions, like in the case of neurons) amongst themselves and with an external environment. These interactions give rise to a broad range of behaviors including catastrophic transitions (e.g., epileptic seizures, earthquakes, and ecological collapse), collective phenomena (e.g., flocking and synchronization), emergence (e.g., pattern formation and self organization), and adaptation (e.g., synaptic plasticity and biological evolution).

---

[1] As of 2016, Facebook has 1.65 billion monthly active users, with the average Facebook user having around 340 friends [2, 3].

Complex systems theory seeks to understand how these microscopic interactions give rise to the macroscopic, qualitative behavior of these systems, in this sense complex systems is intimately related to nonequilibrium statistical physics. Complex systems also tend to operate far from thermodynamic equilibrium, have memory, and be stochastic, as opposed to deterministic—they are ruled by the laws of probability. Constituents of complex systems form intricate webs of interactions which readily lend themselves to a networks description. For example, cells [4], the nervous system [5], ecosystems [6], and even the global climate [7] have all been described in this context. These **complex networks** lie somewhere between regular lattices and complete randomness: they exhibit non-trivial topologies, e.g., hubs, communities, and hierarchical structure [8]. For example, airports and social networks form complex networks which are commonly known to exhibit these features.

Given their complexity, these systems have eluded the mechanistic descriptions typically found in an undergraduate-level physics course. But in the second half of the 20th century, a glimmer of hope emerged from the ubiquitous appearance of power-law scaling in a variety of natural phenomena: earthquakes [9], forest fires [10], solar flares and gamma-ray bursts [11], landslides and avalanches [12], biological evolution [13], neuronal avalanches [14], and economic fluctuations [15]. This signified a couple of important points which might bring these systems together. First, the apparent power-law scaling indicates that these systems may feature behavior which lacks a characteristic scale, i.e., they are scale-free, much like fractals. In the case of earthquakes, for example, there are immense earthquakes such as the 1960 Valdivia earthquake (the largest earthquake ever recorded, registering a 9.5 on the Richter scale[2]), mediocre earthquakes such as the 2010 Indiana earthquake (registering a 3.8 on the Richter scale[3], which felt more like the vibration caused by a fast moving semi-trailer truck than a shifting of geological plates), and everything in between[4]. Second, the apparent presence of scale-free behavior in these systems is important because it may reveal some common underlying processes which give rise to the observed power laws, such as the presence of **critical phenomena**.

---

[2] "Magnitude 8 and Greater Earthquakes Since 1900", U.S. Geological Survey, 2010.

[3] U.S. Geological Survey, 2010.

Critical phenomena correspond to the behavior characteristic of systems undergoing a specific class of phase transition known as a **critical phase transition**. Fig. 1.1 shows different classes of phase transitions, including a critical point, in a generic phase diagram. Generally, phase transitions result from a competition between the influences of the internal energy and entropy, which represent order and disorder, respectively—order dominates in the **ordered phase**, while disorder dominates in the **disordered phase**. In the Ehrenfest classification, phase transitions are grouped in terms of the analytic properties of the thermodynamic free energy, $F = U - TS$, the amount of energy which can be used to do work, where U is the internal energy, T the temperature, and S the entropy. Phase transitions in which the first-order derivative of the free energy is *discontinuous*, as in the case of the melting or freezing of water (see Fig. 1.2), are known as **first-order transitions** (or discontinuous transitions), since it is the *first-order* derivative of the free energy which becomes non-analytic at the transition. Similarly, phase transitions in which the free energy changes *continuously*, as in the case of a Curie transition (see Fig. 1.3), are known as **second-order transitions** (also known as continuous or critical phase transitions), since it is the *second-order* derivative of the free energy which becomes non-analytic.

Moreover, while disorder corresponds to symmetric states, the presence of order indicates a broken symmetry. Consider the solid-liquid transition of water: when frozen, water molecules form into a stable, regular hexagonal lattice (see Fig. 1.4A), however, when liquid, water molecules are in fluid motion (see Fig. 1.4B). Whereas the lattice is only

---

[4] The frequency of occurrence of these events approximately satisfies the scale-free behavior described by the Gutenberg-Richter law.

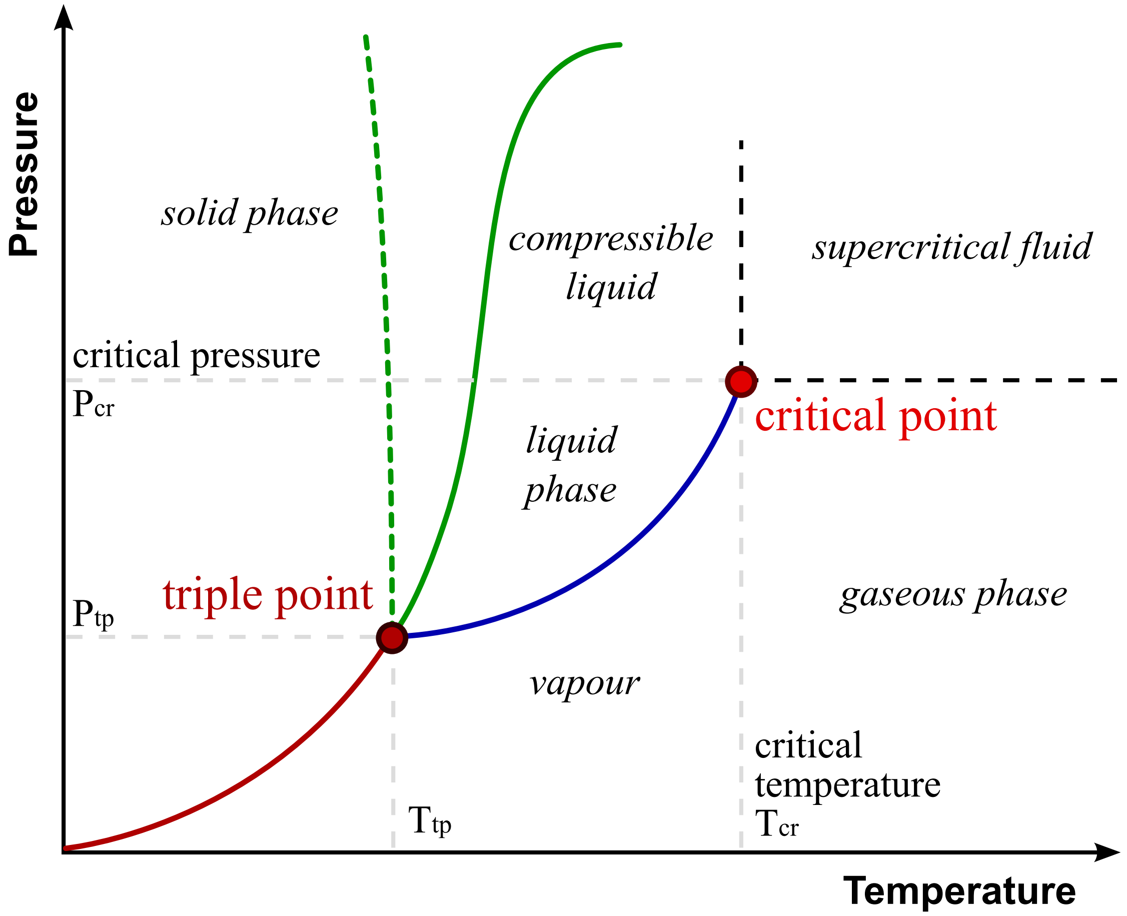
Pressure
solid phase
compressible liquid
supercritical fluid
critical pressure
P_{cr}
critical point
liquid phase
triple point
P_{tp}
gaseous phase
vapour
critical temperature
T_{cr}
T_{tp}
Temperature

Figure 1.1: A phase diagram showing triple and critical points, as well as liquid, gas, and solid phases separated by solid lines. The dotted green line indicates anomalous behavior of water. Figure created by Wikipedia user Magnus Manske and used under Creative Commons license CC-BY-SA-3.0-migrated: `https://commons.wikimedia.org/wiki/File:Phase-diag2.svg`.

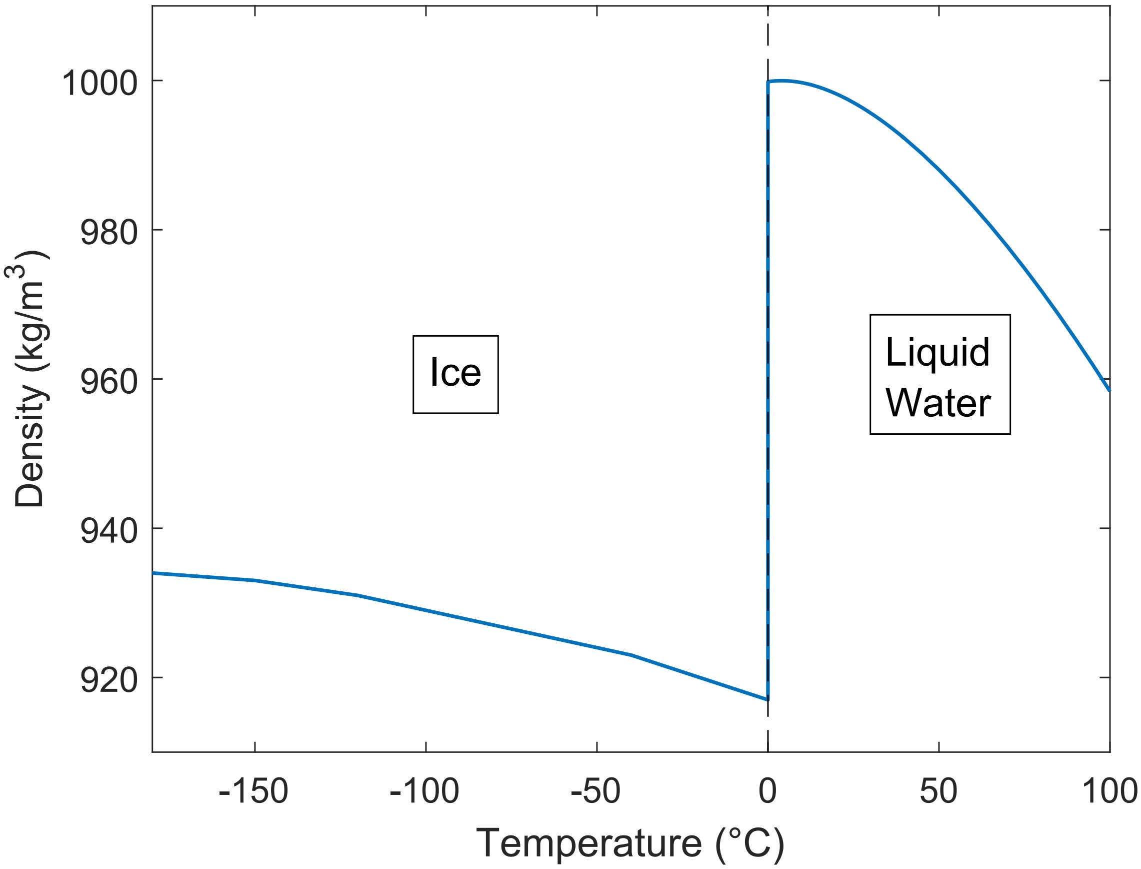

Figure 1.2: A singularity in a physically-observable quantity marks the phase transition. When melting or freezing, the density of water changes discontinuously at the $T = 0$°C transition, due to a similar jump discontinuity in the entropy—the size of this jump is the entropy of fusion. Data obtained from “Dichte von Eis und Wasser” by Wikipedia user Klaus-Dieter Keller under Creative Commons license CC-BY-SA-3.0: `https://commons.wikimedia.org/wiki/File:Density_of_ice_and_water_(en).svg`.

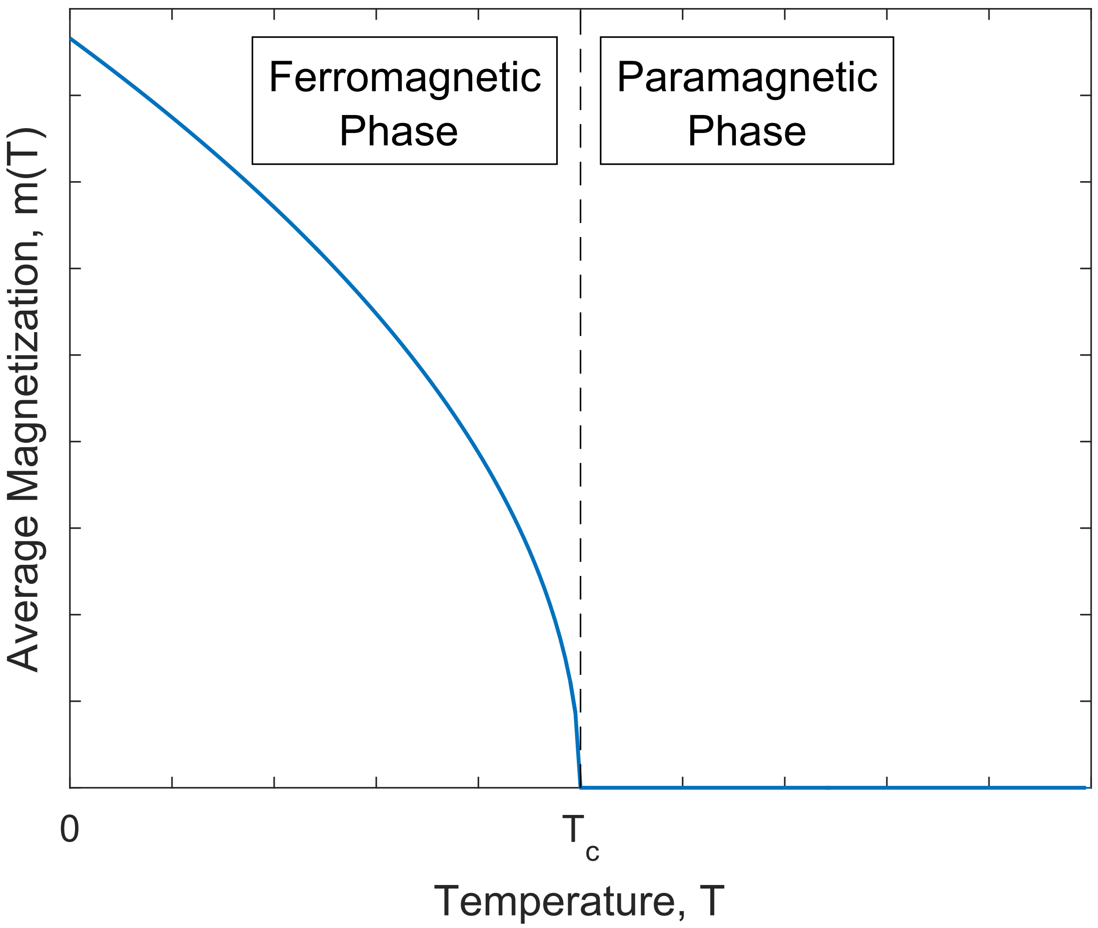

Figure 1.3: Mean-field approximation of a Curie transition as described by the Ising model. The order parameter is the average magnetization which continuously becomes zero at the transition temperature, T_c.

symmetric under rotations through integer multiples of 120° and is frozen in this configuration, the liquid is in constant motion and, over time, retains symmetries in the rotational and translational degrees of freedom of individual molecules. Hence, the regularity of the solid phase corresponds to a higher degree of order, but lower symmetry than the liquid phase. The solid phase of water is said to be a broken symmetry state and, indeed, phase transitions generally correspond to a **symmetry breaking**. An individual phase is then characterized by an **order parameter**, an observable which quantifies the degree of order in that phase; it is identically zero in the disordered phase and nonzero in the ordered phase. A relationship between the free energy and the order parameter can be established after considering the specific symmetries and conserved quantities involved, as is done in the Landau mean-field theory [16].

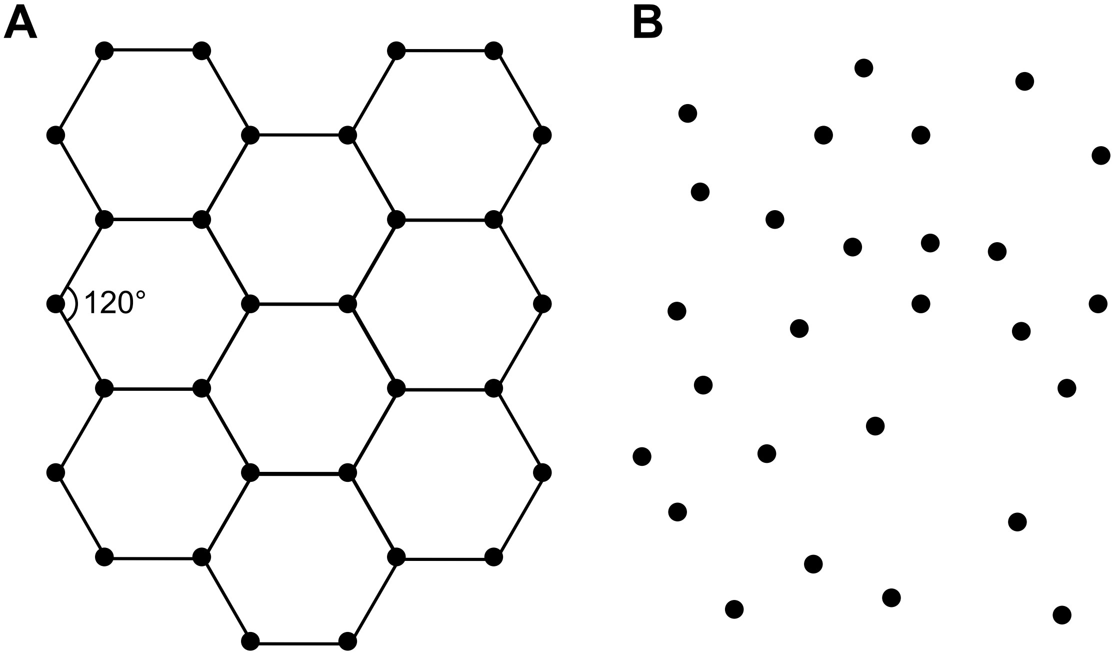

Figure 1.4: The structure of water is ordered into a hexagonal lattice with bond angle of 120° when frozen (A) and disordered when liquid (B). The order parameter for a solid-liquid transition is the spatial periodicity of the molecules.

At a critical point, the response of the system to small perturbations is great and so it can be difficult to tune a system precisely to a critical point in an experiment. This behavior is quantified by the susceptibility, which represents the response of the system to an external field which is *conjugate* to the order parameter, i.e., a field which influences the amount of order in a system[5]. For example, in a ferromagnetic system where the order parameter is the average magnetization m, an externally applied magnetic field h will influence its net magnetization; the magnetic susceptibility, defined by $\chi = m/h$, diverges at the critical temperature T_c when the applied field vanishes ($h \to 0$). Moreover, fluctuations at criticality occur at all length scales and hence these disturbances take a longer time to dissipate, i.e., the correlation length ξ and relaxation time τ_0 diverge, producing such curious phenomena as critical opalescence and critical slowing down, respectively. In critical opalescence, a fluid, such as water or ethanol (or alternatively a binary mixture of these or other fluids), is brought to its critical point, at which point density fluctuations of all length scales appear, including those comparable to the wavelengths of visible light. This situation corresponds to a sudden onset of an opalescent, or milky, appearance to the fluid and, if allowed to move beyond the critical point, the supercritical disappearance of the liquid-gas phase boundary.

In order to connect the power-law behavior of natural systems with critical phenomena, it is important to highlight the *universal* properties of critical phase transitions, which are characterized by **critical exponents** describing behavior close to a critical transition. Different systems exhibiting critical transitions fall into different **universality classes** depending on the values of their critical exponents, which are generically determined by the system's spatial dimension, nature of interactions, conserved quantities, and fundamental symmetries, but not any of the precise details. This means that systems within a certain universality class, which may be qualitatively very different away from a critical transition, behave very similarly at a critical transition. As mentioned previously, certain quantities diverge at a critical transition, and critical exponents describe *how sharply* these quantities diverge. In the case of the magnetic susceptibility, the critical exponents are γ and γ': $\chi \propto (T - T_c)^{-\gamma}$ for temperatures $T > T_c$ and $\chi \propto (T_c - T)^{-\gamma'}$ for temperatures $T < T_c$, where T_c is the critical temperature. Critical exponents are often related by simple **scaling relations**; scaling relations which also involve the dimension of the system are known as **hyperscaling relations**.

---

[5] A quantity related to the susceptibility is the dynamic range: often used in the context of sensory organs, it is the ratio of the largest to the smallest signals perceptible by a sensory system. Human hearing, for instance, typically features a dynamic range of well over 100 dB, i.e., a range spanning 10 orders of magnitude of audio power [17].

To study critical transitions and their associated phenomena (and indeed any physical phenomenon), it is best to start with an analytically tractable, minimal model encapsulating the behavior of the physical system. For example, the Ising model suitably describes the equilibrium Curie transition, in which a ferromagnet loses its magnetism as its temperature T is increased. In the two-dimensional Ising model, spin magnetic moments, which can either be pointing up $(+1)$ or down (-1), are located on the vertices of a square lattice in which they are only allowed to interact with their four nearest neighbors. The sum of all the lattice spin values corresponds to the magnetization. At temperatures below the critical point T_c, neighboring spins tend to align, inducing a nonzero magnetization; this is the ordered ferromagnetic phase. For $T > T_c$, entropy causes spins to no longer tend to align and the magnetization averages to zero; this is the disordered paramagnetic phase. Indeed, the order parameter here is the magnetization. As an example of the utility of universality, the three-dimensional Ising model shares a universality class with simple liquid-gas transitions, with lattice sites being interpreted as molecules instead of spins: a $+1$ indicates the presence of a molecule and a -1 indicates an absence. The order parameter is related to the average number of molecules per lattice site, i.e., the density.

Equilibrium systems like the one described in the Ising model are, however, the exception, not the rule, and as I have already stated, we are interested in nonequilibrium systems. The distinction between equilibrium and nonequilibrium systems can be understood in terms of flows of energy, particles, or other conserved quantities between the system and a reservoir, i.e., an environment; at equilibrium, the net flow is zero. Consider your cup of coffee: the moment you pour coffee into the cup, the liquid is alive with turbulent motion due to kinetic and convective forces, and thermal energy from the coffee begins to flow to the relatively cold cup. Of course, all this is happening while the coffee transfers energy and matter to the surrounding air in the form of steam; the coffee is out of thermal equilibrium. After a sufficient amount of time, however, the turbulent motions of the coffee cease, the coffee is cold, and so is the cup; the coffee has reached thermal equilibrium. The nonequilibrium state described above is transient, only lasting while the cup approaches thermal equilibrium.

Biological organisms actively exchange matter and energy with their environments to maintain a state of nonequilbrium we call life. In the brain, individual neurons are kept from equilibrating with their surroundings by transmembrane proteins and ionic pumps which use chemical energy to maintain chemical and electrical gradients between the intracellular and extracellular media. Their central function involves summing up (or *integrating*) the influences from other neurons up to a threshold, at which point they produce an action potential, which then propagates throughout the neural network for other neurons to process. This neural processing approximately falls under a key universality class of nonequilibrium phase transitions known as **directed percolation** [18, 19]. To explain directed percolation, another cup of coffee is in order: let us consider the process of pulling an espresso shot. High-temperature water is forced through a densely-packed *puck* of ground coffee at high pressure; as the water percolates through the puck, it becomes espresso. The percolation transition is complete when the espresso traverses the width of the puck. This process is **irreversible** in that once the water has passed across a grain of ground coffee and extracted the caffeine, there is no going back; the entropy of the universe has increased. Because the system features microscopic processes which are irreversible, it is said to lack a **detailed balance**—a characteristic feature of nonequilibrium systems. A bond percolation model can be used to describe the transition, with grains of coffee sitting at the vertices of a regular lattice. As the water begins to flow through the puck, each vertex is irreversibly connected by a directed edge (an arrow) to a neighbor with probability p and the percolation transition occurs at a critical value p_c (see Fig. 1.5).

As with the equilibrium case, nonequilibrium critical transitions also feature universal critical behavior and some of the same approaches used in equilibrium situations can be extended to nonequilibrium transitions. The theory of equilibrium and nonequilibrium phase transitions is presented along with detailed descriptions of the Ising and directed percolation models in Chapter 2, while keeping a focus on the external field (i.e., the environment), and its influence on the presence of a phase transition.

Because of the feature of universality, the idea that many natural systems are operating at a critical phase transition is an alluring one, since we need only determine the appropriate universality class to describe their behavior. It can be difficult, however, to bring an experimental system to criticality and this critical state is even harder to maintain due to fluctuations associated with criticality. If natural systems are always operating at criticality, some mechanism must be at play, which allows for criticality in the absence of *fine-tuning*. It was proposed that in such systems, criticality *emerges* from the intrinsic dynamics, i.e., they *self-organize* to criticality.

To determine the features necessary to exhibit **self-organized criticality** (SOC), a simple model, the Bak-Tang-Wiesenfeld (BTW) sandpile model, was put forth in Per Bak

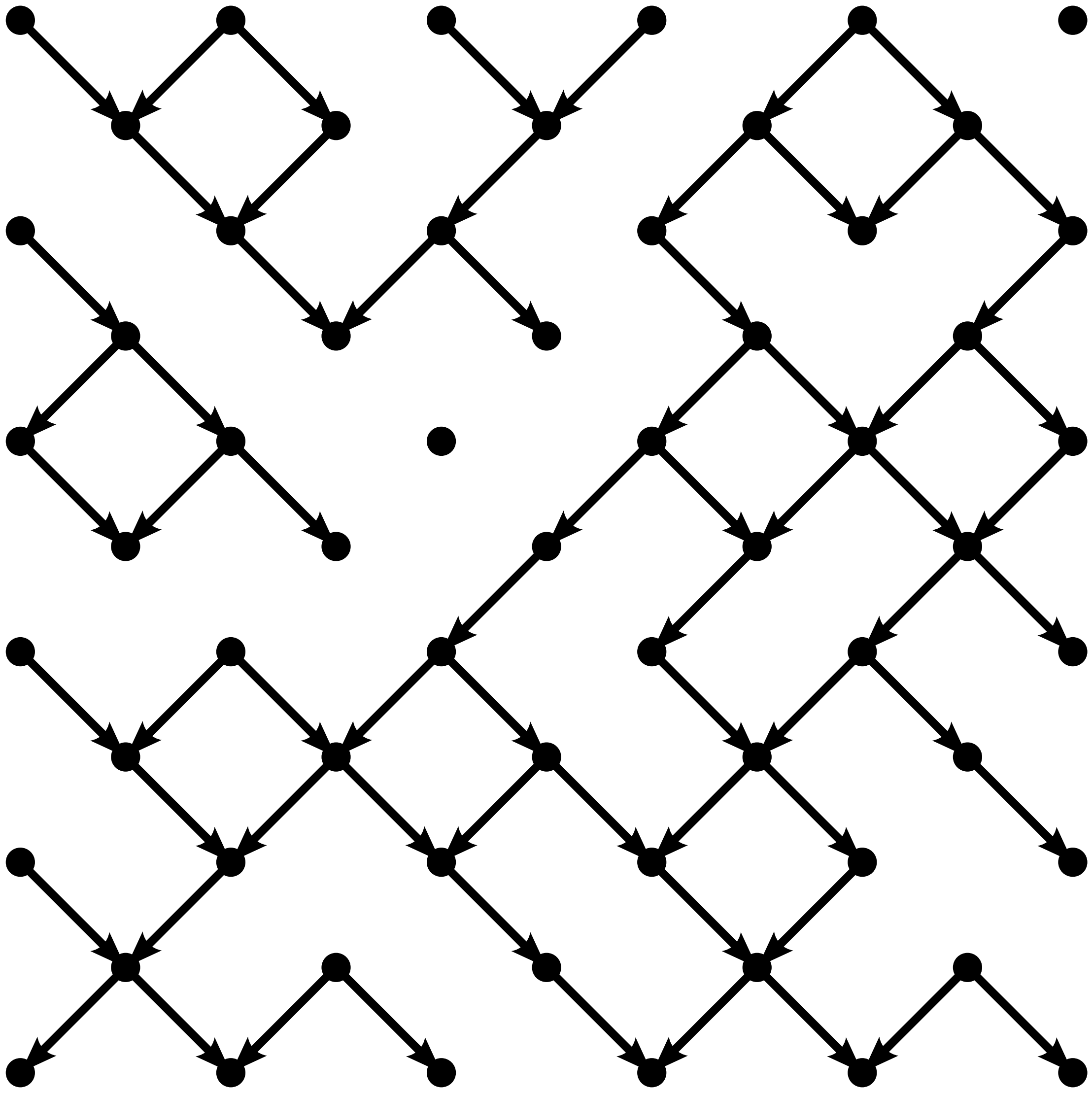

Figure 1.5: Bond directed percolation. Figure adapted from “Bond directed percolation” by Wikipedia user Lokal_Profil under Creative Commons license CC-BY-SA-2.5: `https://commons.wikimedia.org/wiki/File:Bond_Directed_Percolation.svg`.

et al.'s seminal work [20]. In the two-dimensional case, grains of sand are dropped one at a time on random lattice sites on a two-dimensional lattice and a pile of sand begins to emerge. When the sand pile at a given site reaches a threshold height, the pile topples, spilling its grains onto neighboring sites, potentially inducing further topplings. Successive topplings are thus causally related, with each new toppling having been induced by another which came before. Together, these topplings form a spatiotemporal event known as an **avalanche**, with the **size** of such avalanche events being given by the number of sand grains which have toppled. If the slope of the pile is too shallow, small avalanches will be typical; if the slope is too steep, however, large avalanches will dominate. As this process is repeated, the pile eventually reaches a steady, nonequilibrium state, *self-organizing* to a *critical* slope where, as additional grains are dropped, avalanches of all sizes will be observed; the avalanche size probability distribution exhibits power-law scaling, as one would expect at criticality. It is important to note that the grains are dropped at an infinitesimally slow rate such that the relaxation timescale, i.e., the duration of the avalanches, is much shorter than the time between grain drops. This **separation of timescales** is essential to the framework of SOC [21].

One of the many applications of the SOC framework is in understanding the complex networks of the nervous system [21]. Over the past twenty years, there have been a large number of theoretical and experimental attempts to connect activity in living neural networks to critical avalanches like those seen in the BTW sandpile model [20, 22]. Where we would have spoken of avalanches of sand grains in the BTW model, in a neural network avalanches correspond to cascades of spreading neuronal activation. And where in the BTW model, the ordered (disordered) phase may have corresponded to large (small) avalanches, in a neural network, the ordered (disordered) phase corresponds to cascades which are amplified (damped).

Indeed, SOC is an alluring idea not only because it could unify a seemingly disparate set of natural phenomena, but also because it brings up and potentially answers questions about why these systems are operating at criticality to begin with. Biological systems, for example, may have evolved to operate at a critical point to enhance their performance. Theoretical and numerical simulation work has suggested that neural networks poised at a critical point would feature optimal information transmission [14], information storage [23, 24], computational power [25, 26], dynamic range [26, 27, 28, 29, 30, 31, 32, 33], and learning capabilities [34], while providing flexible, yet stable dynamics [23, 35]. Several experiments claim results consistent with these predictions [36, 37, 38], lending plausibility to the **criticality hypothesis** of brain function[6]. To understand intuitively why a critical point may optimize the flow of information, consider the diverging correlation length at criticality; this is the point at which a signal introduced at one part of the system is most likely to be faithfully propagated through the entire system, whereas the signal would be lost to noise away from the critical point. Homeostatic mechanisms have been hypothesized to *tune* the brain to operate near a critical point [40, 41, 42, 43, 44].

These results are consequences of the discontinuities and power-law scaling associated with critical transitions. Note, however, that the appearance of power laws in these systems does not guarantee that the underlying physical system is critical; it is a necessary, but insufficient condition for criticality. In living neural networks, power laws may arise incidentally, in the absence of criticality, due to a filtering of electrical signals through extracellular media [45], stochastic dynamics [46], or undersampling effects [47]. There are also inherent problems in identifying power laws: a system's proximity to a critical point [48], inherent difficulty in identifying true power laws [49, 50], not to mention the finite sizes of living systems, which prevents true singularities in quantities such as the susceptibility—although this last point can be addressed by performing a finite-size scaling.

---

[6] Generally, the criticality hypothesis states that "living systems will self-organize to operate near a critical point" [39].

In Chapter 3, I elaborate on the framework of SOC, the BTW model, and a neural network analog of the BTW model, known as the cortical branching model (CBM) [14].To the uninitiated, my implementation of the CBM [19] might seem naive at best, however, the model relies on a physical interpretation of probability. If we are talking about flipping a coin or rolling a die, a large number of variables affect the outcome: every molecule colliding with the volant object, its shape, the air resistance, temperature, pressure, etc., all affecting it in minuscule and imperceptible ways, which accumulate to produce qualitative changes in the outcome. But this process, due to its complexity, is shrouded in mystery—we are *a priori* unable to predict the outcomes—and so instead of burying our heads deep in the thicket, we assign probabilities. In this sense, the assignment of probability corresponds to a lack of knowledge: there is a "black box" in our possession, producing some outcome every time we interact with it, which is only predictable in a statistical sense, if at all, i.e., after many, many measurements. In my implementation CBM, neurons are modeled as "black boxes" which produce an outcome, i.e., an action potential, stochastically, depending on their state and the state of the network of which they are part.

The CBM represents individual neurons as stochastic elements (called nodes) embedded on a directed graph whose edges correspond to the axons and dendrites of a living neural network. Each node can be in a number of integer-valued states $z \in \{0, 1, 2, 3, ...\}$ representing neuronal quiescence ($z = 0$), firing of an action potential ($z = 1$), and refractory states ($z > 1$). A node becomes active stochastically due to the influence of its neighbors, i.e., its afferents, which are represented by directed edges pointing towards the node—the strength of the connection is represented by an activity transmission probability: the higher the probability, the stronger the connection. Note that actual neurons are quiescent until their membrane potential reaches a threshold voltage, at which point they fire an action potential, before returning to quiescence after a brief refractory period—the CBM represents a sort of coarse-graining of these details, a metaphor for true neural network dynamics. Despite its simplicity, the CBM has been successful in reproducing statistics of neuronal avalanches in living neural networks, demonstrating power-law scaling, and thus potentially critical dynamics.

A single event can be used to trigger a neuronal avalanche, which is allowed time to terminate before another avalanche is triggered. In this way, the CBM is said to be *slowly driven* and *interaction dominated*, thus maintaining the separation of timescales necessary for SOC [51]. When the average synaptic strength is small, the CBM exists in a phase where neuronal avalanches are quickly extinguished; when the average synaptic strength is great, neuronal avalanches continue for a long time and may not terminate. A transition occurs at an average synaptic strength corresponding to an average number of descendant activations equal to 1—this is described by a **branching parameter**, κ. Using a mean-field approximation, an analytical description of the transition can be explored in the thermodynamic limit, i.e., in the limit that the system size is infinitely large. The order parameter is the density of active nodes and the corresponding *dynamical* susceptibility diverges at $\kappa = 1$, as suspected. Moreover, the mean-field critical transition belongs to the mean-field directed percolation universality class [19].

Many complex systems, including living systems, however, cannot be said to be *slowly driven* or *interaction dominated*, meaning a lack of a separation of timescales, and thus no SOC. External environments do not wait for the fluctuations in a system to cease before continuing their influence the system—the influence is ever-present—and so the driving and interaction timescales are not at all separate. At all times, the brain is under the influence of its environment and this has a drastic effect on its behavior which cannot be ignored, e.g., touch, sound, the diurnal cycle which controls our circadian rhythms, or even our gut microbiota, which has been shown to influence our cognitive functions [52]. This is analogous to the cooling coffee cup exchanging energy with the thermodynamic heat bath of a room. To model these influences, a generalized version of the CBM is presented in Chapter 4, where nodes are allowed to become active spontaneously with some probability. This turns out to be a useful generalization, since spontaneous activations can also model intrinsic properties of neurons, e.g., neurons which are tonically active can be modeled as nodes with high spontaneous activation probabilities and distributions of spontaneous events with means corresponding to the neurons' average firing rates. The result of including this influence is a loss of the critical point, which is replaced with a cross-over region where the dynamical susceptibility no longer diverges [19].

As a consequence of not having a separation of timescales due to external influences and their definition, neuronal avalanches may conflate unrelated events, which may confound their statistics. For example, consider an ongoing avalanche during which an environment introduces additional activations or two distinct avalanches which are joined only incidentally due to a spontaneous activation which occurs between them. The size distribution will consequently contain additional avalanches of larger size which do not reflect the underlying dynamics. An even more confused situation will arise if interactions feature delays, as they do in neural networks with synaptic delays. These issues call for a more meticulous analysis of neural network dynamics, which considers causal relations between activations. Such causal relations can be made by considering the network structure and synaptic delays, and the resulting set of causal relations form intricate descriptions of neuronal cascades, which we have named **causal webs**, or c-webs. An added benefit of this analysis is the separation of exogenous events caused by outside influences from those which are endogenous and due to the network structure and internal dynamics. That is, we are now able to measure the spontaneous activation probability *from experimental data*. This is a key step in being able to characterize what is called **dynamical disorder** in a living neural network—we can now measure how this external influence changes with time or with certain stimuli, how different neurons feature different spontaneous activation probabilities (e.g., tonically firing neurons), and, potentially, what the sources of these spontaneous activations are. Moreover, we can use this information to improve simulations of living neural networks and test the quasicriticality hypothesis. I describe causal webs, their properties, and the method used to determine them in Chapter 5. Finally, I outline the impact my work has made on the field and present additional questions for future research in Chapter 6.

Papers Associated with this Thesis

- R. V. Williams-García, M. Moore, J. M. Beggs, & G. Ortiz, "Quasicritical brain dynamics on a nonequilibrium Widom line", Physical Review E **90**, 062714 (2014).
- R. V. Williams-García, J. M. Beggs, & G. Ortiz, "Unveiling causal activity of complex networks", Physical Review Letters (under review).

CHAPTER 2

Elements of Phase Transitions

Presented here is the theory of second-order (i.e., critical) phase transitions in the context of magnetic spin and percolating systems to address equilibrium and nonequilibrium situations, respectively. The typical model used to describe equilibrium critical transitions is the Ising model, which presents a simplified picture of a ferromagnet. In this picture, atoms—each of which feature a spin degree of freedom—are arranged on a simple, regular lattice, interacting only with their respective nearest neighbors, and an externally-applied magnetic field.

The Ising model represents an equilibrium magnetic system at a fixed temperature and can be solved exactly in up to two dimensions, although I will only review mean-field approximations here [16]. Prior to the development of exact solutions[1], various methods were developed to approximately solve the two-dimensional Ising model. One of these focuses on the behavior of a single atom under the influence of a *mean field*, i.e., the averaged (or *mean*) behavior of the rest of the system. In this way, a solution can be found which is analytical and exhibits the same symmetries as the original system. I describe an additional mean-field approximation based on the fundamental symmetries of the Ising model to produce the same results. The mean-field approach yields behavior which is equivalent to that of the original system in the thermodynamic limit, i.e., in the limit of an infinite system size. I have placed the emphasis on mean-field approximations, as this approach can be fruitfully applied to more complex models presented later in Chapter 4; I also highlight the influence an external magnetic field has on the presence of a critical point. As part of the analysis, I derive the critical exponents β, γ, and γ', corresponding to the scaling behavior of the magnetization $m(T)$ and magnetic susceptibility $\chi(T)$ near the critical temperature $T = T_c$: $m(T) \propto (T_c - T)^{\beta}$ and $\chi(T) \propto (T_c - T)^{-\gamma'}$ for $T < T_c$, as well as $\chi(T) \propto (T - T_c)^{-\gamma}$ for $T > T_c$.

---

[1] Based on the transfer matrix method developed by Lars Onsager in 1944 [53].

In Section 2.2, I describe a model of directed percolation (DP), which exhibits a nonequilibrium critical phase transition, and present a simple mean-field approximation [54]. Whereas in the Ising model, *faux* dynamics may be performed, e.g., via Monte Carlo methods, to arrive at a distribution of states satisfying the equilibrium canonical ensemble, in DP, we must simulate the actual dynamics. Moreover, instead of having a time-independent Hamiltonian, we must rely on a master equation; DP is a type of reaction-diffusion process in which, e.g., wet lattice sites *interact* with dry ones to produce additional wet sites with probability p. DP belongs to one of the most important universality classes of nonequilibrium phase transitions, and which bears its name: the **DP universality class**. The phase transition exhibited by DP at a critical value $p = p_c$ separates an **absorbing phase** from an **active phase**. The absorbing phase is akin to the previously-described equilibrium disordered phases, so named because such a system is unable to escape the absorbing phase once it has been reached; this is intimately related to the irreversibility of nonequilibrium processes. For example, if the system starts with a single active site which does not propagate its activity, then the system remains inactive. In the active phase, however, active sites will produce further activation and activity tends to grow with time; such a nonequilibrium phase is analogous to the equilibrium ordered phase. Both active and absorbing phases may feature fluctuating dynamics, e.g., avalanches.

Nonequilbrium phase transitions also feature critical behavior and universality, but with additional critical exponents which involve the passage of time t, e.g., those associated with the **correlation time**, $\xi_{\parallel} \propto (p - p_c)^{\nu_{\parallel}}$, and the growth of the spatial **correlation length**, $\xi_{\perp}(t) \propto t^{1/z}$, where z is the **dynamical critical exponent**[2]. These exponents also have corresponding scaling relations, e.g., $z = \nu_{\parallel}/\nu_{\perp}$, where $\nu_{\perp}$ is associated with the correlation length, $\xi_{\perp} \propto (p - p_c)^{\nu_{\perp}}$. An alternative set of exponents associated with features of the fluctuations may be used, e.g., τ, which is associated with the size of an active cluster. The **Janssen-Grassberger conjecture** [55, 56] speculates that a model should belong to the DP universality class if

1. there is a continuous transition separating the absorbing and active phases,
2. the transition is characterized by a non-negative, single-component order parameter,
3. the interactions are short-ranged, and
4. there are no unconventional symmetries, conservation laws, or quenched randomness.

2.1 Equilibrium Transitions: The Ising Model

Consider a two-dimensional square lattice whereupon atoms are organized on the vertices and bonds between atoms are represented by edges. At each vertex i, a magnetic spin s_i associated with the atom at that site can be either up or down, i.e., $s_i \in \{-1, +1\}$, representing a degree of freedom with bond interactions which respect a $\mathbb{Z}_2$ symmetry.

In a ferromagnet, neighboring spins align to minimize the thermodynamic free energy; in the case of an antiferromagnet, adjacent spins prefer to anti-align. There is hence an energy cost associated with each pair of spins $\langle i, j \rangle$ in a ferromagnetic system, which is modeled as $-Js_is_j$, where $J > 0$ is the coupling strength. When $s_i = s_j$, the energy cost is minimized; whereas if $s_i \neq s_j$, the cost is greater than zero—an unfavorable situation. Indeed, for each configuration of spins $\{s_i\}$, there is an associated energy cost $H = F[\{s_i\}]$. In the Ising model, we write this cost as the Hamiltonian

---

[2] The dynamical critical exponent z dictates the divergence of the relaxation time at criticality, $\tau_0 \propto \xi_{\perp}^{z}$, a phenomenon otherwise known as **critical slowing down**.

$$H = -\sum_{\langle i,j \rangle} J_{ij} s_i s_j - \sum_{i=1}^{N} h_i s_i, \tag{2.1}$$

where the first sum is taken over all pairs of neighboring spins and N is the total number of lattice sites. Generally, the interactions J_{ij} may be random variables, but for simplicity, we will consider $J_{ij} = J$ for all spin pairs $\langle i, j \rangle$. We have also here included an external field h which causes spins to align toward it. I will forgo a description of Onsager's exact solution in favor of describing two important mean-field approaches in the following sections. A complete description of Onsager's exact solution as well as approximation methods beyond the mean field, such as the Bethe-Peierls approximation, can be found in [16].

2.1.1 A Mean-Field Approximation

In the mean field, we focus our attention to a single spin at site i and its nearest neighbors j, which we consider to feature only small deviations from the mean magnetization m, i.e., $m \approx \langle s_j \rangle$. The Ising Hamiltonian (Equation 2.1) thus becomes

$$H \approx -\left(Jmz + h\right) \sum_{i=1}^{N} s_i, \tag{2.2}$$

where z is the coordination number[3] and we are assuming a translational invariance such that $H \approx \sum_i H_i$. Each spin is essentially treated independently since we have removed all interaction terms between spins and replaced them with an *effective field*, given by Jmz, which surrounds each spin. We can now calculate the magnetization m, by solving the *self-consistent relation* stating that $m = \langle s_i \rangle$, where the angled brackets correspond to a

---

[3] Not to be confused with the node dynamical state variable z, which we introduce in Chapter 3.

thermal average over all possible configurations of the spin s_i, i.e.,

$$m = \frac{1}{Z} \sum_{s_i=\pm 1} s_i e^{-\beta H_i} = \frac{\sum\limits_{s_i=\pm 1} s_i e^{\beta(Jmz+h)s_i}}{\sum\limits_{s_i=\pm 1} e^{\beta(Jmz+h)s_i}}, \tag{2.3}$$

where Z is the partition function, $\beta = 1/k_B T$ (not to be confused with the critical exponent β), with k_B being the Boltzmann constant (which I will typically take as 1, for simplicity), and T is the temperature. Evaluating the sums, we arrive at the equation of state

$$m = \tanh \beta(Jmz + h), \tag{2.4}$$

a transcendental equation which can be solved numerically (see Figure 2.1). Solutions correspond to intersections between the black line ($y = m$) and the colored curves ($y = \tanh \beta(Jmz + h)$), with stability determined by the slope of the colored lines at a crossing. The situation in the absence of an external field, i.e., when $h = 0$, is presented qualitatively in Figure 2.1A. When $\beta Jz \leq 1$, the only stable solution is $m = 0$. When $\beta Jz > 1$, three solutions appear, but only the non-vanishing solutions are stable and the system converges to one of these depending on the starting conditions, i.e., whether $h = 0$ is approached from below ($h \to 0^-$) or above ($h \to 0^+$). This situation is known as a *spontaneous magnetization*; the magnetization suddenly becomes nonzero as the temperature reaches T_c (see Figure 2.2).

To determine values of the mean-field critical exponents, we need not exactly solve the self-consistent relation in Equation 2.4, since we can limit our analysis to behavior near the critical temperature $T_c = Jz$ and in the limit $h \to 0$ (since this is necessary to observe critical behavior, as I have demonstrated). At this point, $m \approx 0$ and so we can expand the relation in this limit, thus yielding

$$m = \beta Jmz - \frac{1}{3}(\beta Jmz)^3 + \mathcal{O}(m^5). \tag{2.5}$$

Considering only terms up to third order in m, we arrive at

$$m \approx \frac{1}{\beta Jz} \sqrt{\frac{Jz - T}{Jz}}. \tag{2.6}$$

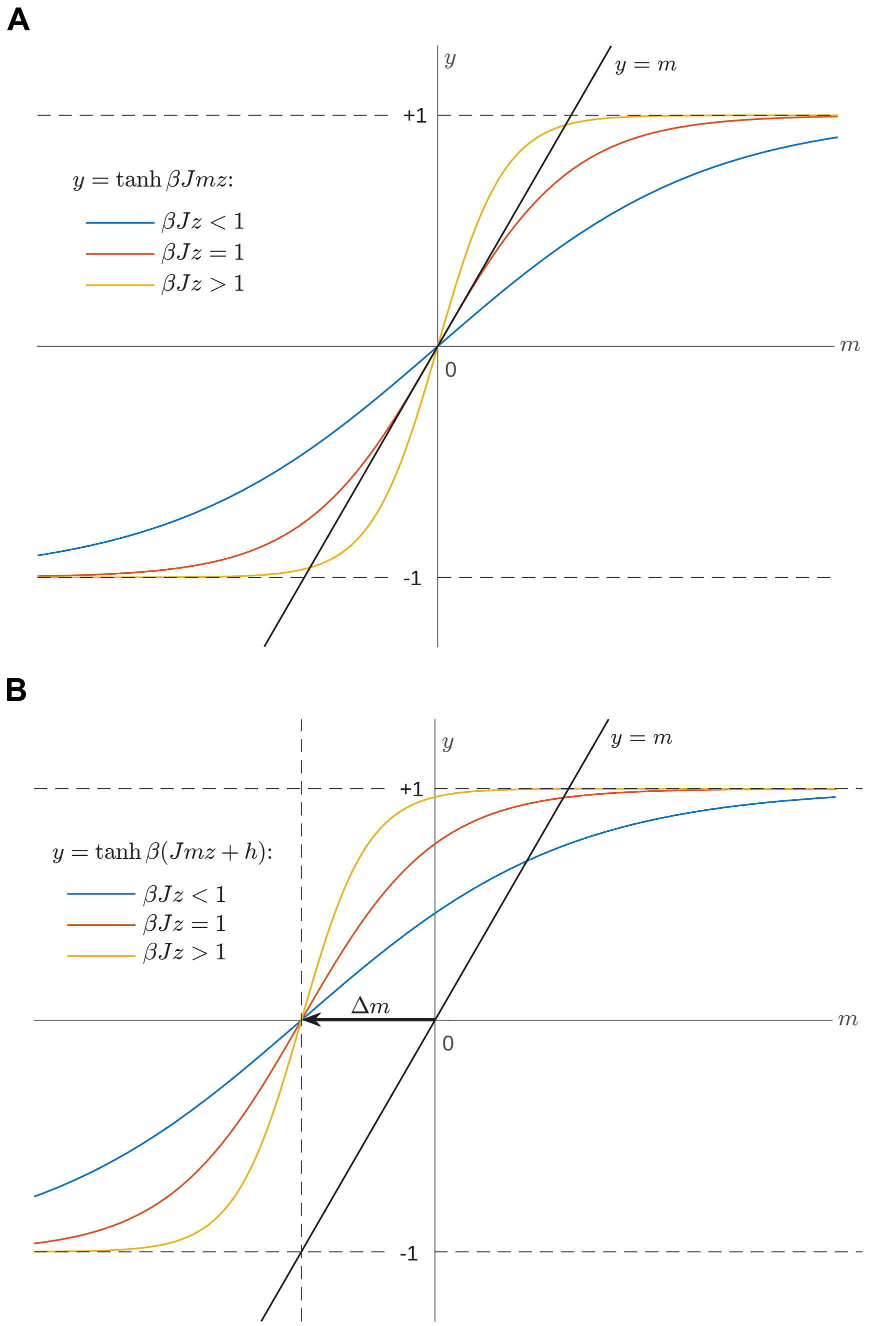

Figure 2.1: Solutions to Equation 2.4 correspond to intersections of the black and colored lines. **A.** When $h = 0$, the $m = 0$ state is viable so long as $\beta Jz \leq 1$, but a spontaneous magnetization appears as βJz is increased. **B.** When $h > 0$, the colored curves are shifted by $\Delta m = h/Jz$, and so the $m = 0$ state represents a solution only asymptotically in the limit $T \to \infty$; the phase transition has been eliminated by the influence of the environment.

When $T = T_c$, $\beta Jz = 1$, and we arrive at the desired scaling behavior $m(T) \propto (T_c - T)^\beta$, where $\beta = 1/2$, not to be confused with the inverse temperature β. Note that this is only valid for $T < T_c$ (see Figure 2.2).

In the disordered phase ($T > T_c$), a magnetization emerges in response to an externally-applied magnetic field, quickly growing near T_c. This behavior is quantified by the **magnetic susceptibility**, χ, which diverges at the critical point (see Figure 2.2B). It is defined through the relation $m = \chi h + \mathcal{O}(h^3)$, or alternatively,

$$\chi = \lim_{h \to 0} \frac{\partial m}{\partial h}, \tag{2.7}$$

which quantifies the receptiveness of the system to an infinitesimally-small, externally-applied magnetic field h. Evaluating the equation of state (Equation 2.4) near the critical point, i.e., with $m \approx 0$ and $h \approx 0$, we arrive at $m = \beta(Jmz + h) + \mathcal{O}(m^3)$. Then, applying the corresponding relation $m = \chi h$:

$$\chi \approx \frac{\beta}{1 - \beta Jz} = \frac{1}{T - T_c}, \tag{2.8}$$

and so the value of the critical exponent is $\gamma = 1$ for the case $T > T_c$. To evaluate the critical exponent γ' corresponding to the behavior of the susceptibility below the critical point, i.e., for $T < T_c$, we differentiate Equation 2.4 with respect to h, and take the limit $h \to 0$ to solve for χ:

$$\chi = \frac{\beta \operatorname{sech}^2 \beta Jmz}{1 - \beta Jz \operatorname{sech}^2 \beta Jmz}. \tag{2.9}$$

Approaching the critical point from $T < T_c$, the magnetization takes the form given in Equation 2.6, but is nearly zero in the vicinity of the critical point, and so, to second-order in m, the above expression becomes

$$\chi \approx \frac{\beta(1 - (\beta Jmz)^2)}{1 - \beta Jz(1 - (\beta Jmz)^2)}. \tag{2.10}$$

Finally, we have the scaling behavior:

$$\chi \propto \frac{1}{T_c - T}, \tag{2.11}$$

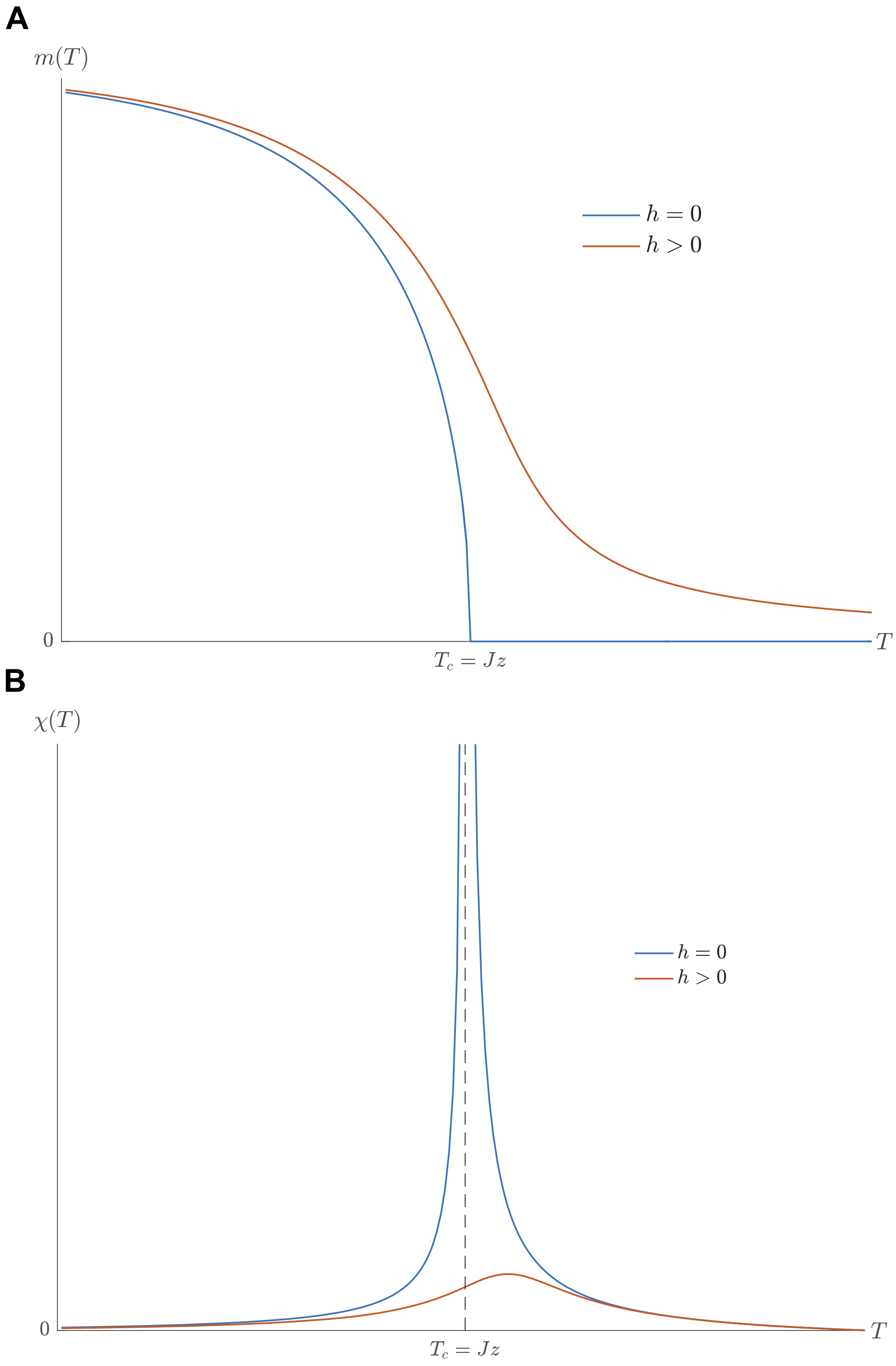

Figure 2.2: A phase transition in the Ising model is allowed only when $h = 0$. When $h \neq 0$, the critical transition is replaced with a crossover region.

where we have employed the approximation $\beta Jz \approx 1$ on account of being in proximity of $T_c = Jz$, thus giving the value of the critical exponent $\gamma' = 1$.

The Crossover Region and the Equilibrium Widom Line

In the presence of an external field, i.e., when $h \neq 0$, the situation changes dramatically (see Figure 2.1B). If the field $h > 0$ is strong enough, prior solutions corresponding to $m < 0$ are no longer viable, and the only solutions correspond to $m > 0$ (see Figure 2.1B). As a consequence, the state corresponding to $m = 0$ is no longer allowed, and thus the critical transition at $T = T_c$ disappears, being replaced by a **crossover region** wherein the magnetization gradually changes from $m = 1$ at $T = 0$ to $m = 0$ asymptotically as T approaches infinity (see Figure 2.2A). Similarly, the magnetic susceptibility no longer diverges, although it still features a peak at temperatures $T_w(h)$, depending on the magnitude of the external magnetic field h; these temperatures define an **equilibrium Widom line** separating ferromagnetic-like, for $T < T_w(h)$, from paramagnetic-like, for $T > T_w(h)$, states of the system. We can find an equation for the Widom line by extremizing the susceptibility in Equation 2.7 with respect to the temperature T. Using Equation 2.4, we arrive at the expression

$$\frac{\partial m}{\partial h} = \frac{\beta \operatorname{sech}^2 \beta(Jmz + h)}{1 - \beta Jz \operatorname{sech}^2 \beta(Jmz + h)}, \tag{2.12}$$

which we maximize, yielding a transcendental equation for the Widom line, $T_w(h)$:

$$T_w(h) = 2(Jmz + h) \tanh \frac{Jmz + h}{T_w(h)} + Jz \operatorname{sech}^2 \frac{Jmz + h}{T_w(h)} \tag{2.13}$$

2.1.2 Landau Theory

In 1937, Lev Davidovich Landau presented a general model of second-order phase transitions, which demonstrates the power of symmetry arguments in the context of understanding critical transitions [57]. In this variation on the mean-field approximation, the free energy

f can be written as a series expansion in powers of the magnetization m so long as we are close to the critical point, where $m \approx 0$. Due to the global $\mathbb{Z}_2$ symmetry in the Ising model, flipping the signs on all the spin should cause no change in the free energy, and so the free energy should involve only even powers of m,

$$f = f_0 + am^2 + bm^4 + ..., \tag{2.14}$$

where f_0, a, and b are constants independent of m. Thermodynamic equilibrium corresponds to a state of minimization of the free energy; if $b < 0$, then the minimum f would be at $m \to \pm\infty$, presenting an instability. Minimizing the free energy with $b > 0$ gives two possible equilibrium states:

$$m = \begin{cases} \pm\sqrt{-\dfrac{a}{2b}}, & \text{for } a < 0 \\ 0, & \text{for } a \geq 0 \end{cases} \tag{2.15}$$

From this we can gleam that $a \propto T - T_c$ and that, hence, the critical exponent $\beta = 1/2$—recall that $m \propto (T - T_c)^\beta$ close to the critical point. Note that when $a < 0$, only one of the two available minima is actually realized, and so the $\mathbb{Z}_2$ symmetry is broken, whereas it is preserved when $a \geq 0$ and the system is in the disordered state: this is an example of a **spontaneous symmetry breaking** (see Figure 2.3A). To obtain critical exponents γ and γ', we compute the magnetic susceptibility χ, which is defined as

$$\chi = \lim_{h \to 0} \frac{\partial m}{\partial h}, \tag{2.16}$$

where h is the external magnetic field. Recall that $\chi \propto (T - T_c)^{-\gamma}$ for $T > T_c$ and $\chi \propto (T_c - T)^{-\gamma'}$ for $T < T_c$. We hence modify the Landau free energy expansion as follows

$$f = f_0 - hm + am^2 + bm^4 + ..., \tag{2.17}$$

where you will notice that the presence of an external field breaks the $\mathbb{Z}_2$ symmetry from the outset, tilting the free energy, and favoring alignment of the spins with the external

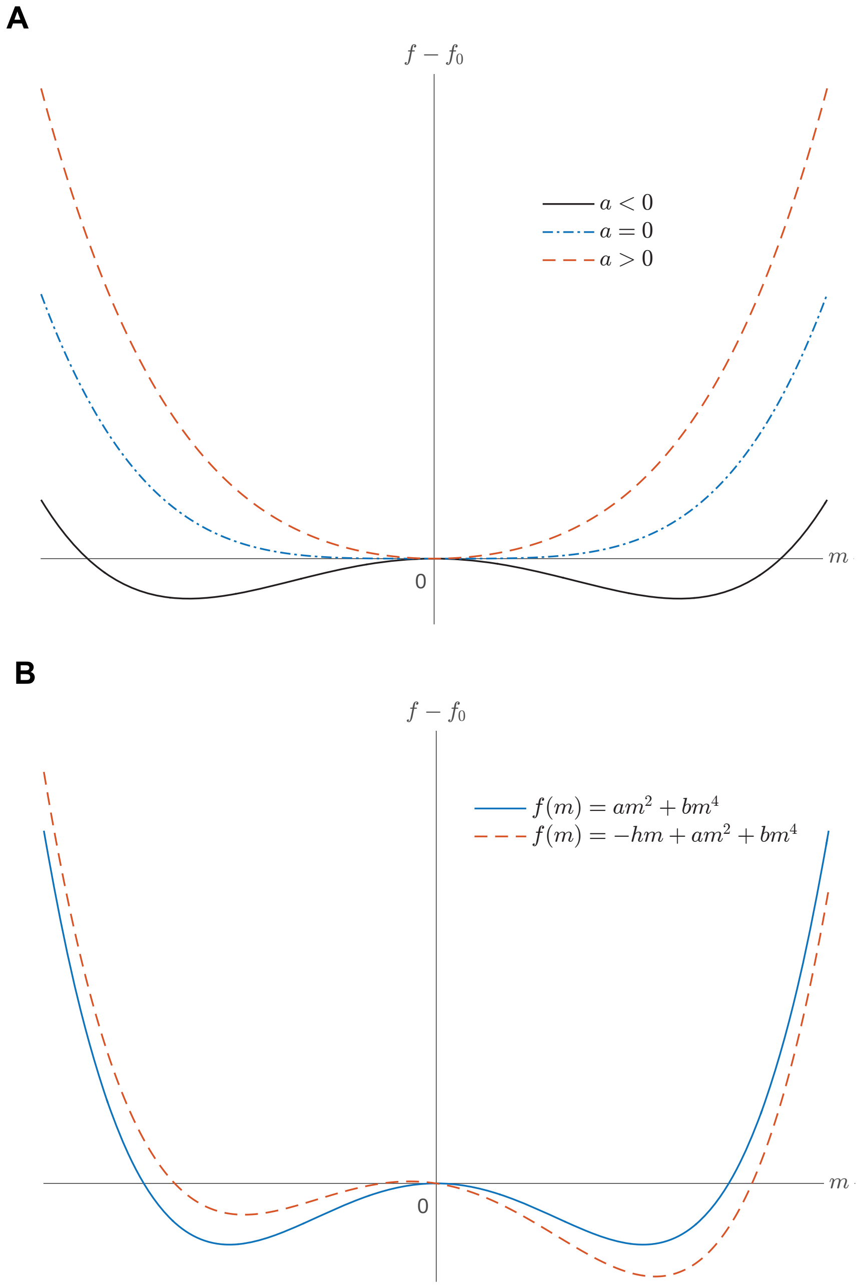

Figure 2.3: **A.** Landau free energy $f - f_0$ plotted against the Landau order parameter m with $b > 0$. A spontaneous symmetry breaking occurs when $a = 0$, at which point the free energy acquires two minima, as a is decreased. **B.** Landau free energy $f - f_0$ with $a < 0$ and external field $h > 0$. The $\mathbb{Z}_2$ symmetry in this ordered equilibrium state is explicitly broken in the presence of the external field; notice the lower minimum on the right.

field; this is an example of an **explicit symmetry breaking** (see Figure 2.3B). We thus have

$$\frac{\partial f}{\partial m} = -h + 2am + 4bm^3 = 0, \tag{2.18}$$

which after differentiating with respect to h gives

$$\frac{\partial m}{\partial h} = \frac{1}{2a + 12bm^2}. \tag{2.19}$$

Because we are interested in the $h \to 0$ limit, we utilize the zero-field equilibrium magnetizations given in Equation 2.15 to find $\gamma = \gamma' = 1$. These agree with the mean-field exponents found in Section 2.1.1.

2.2 Nonequilibrium Transitions: Directed Percolation

Directed percolation refers to the phenomena associated with the movement of fluids through porous media, i.e., filters [54]. The paradigmatic model for this kind of phenomena involves a network of nodes and edges connecting the nodes. Nodes represent pores in filters and edges represent channels connecting pores. Due to irregularities in the filter, these channels may be blocked or open, and so in the model, edges are open with a probability p (see Figure 2.4A). This is describing **bond directed percolation**, which features an irregular lattice topology upon which the dynamics can play out. We might want to ask how p influences the macroscopic permeability of the filter. As the number of pores approaches infinity, i.e., in the thermodynamic limit, a continuous phase transition occurs at a value $p = p_c$ separating a phase where the filter is permeable and another where the filter is not.

Unlike the equilibrium Ising model, where the Hamiltonian is known and is a *constant of the motion*, directed percolation is a nonequilibrium model which evolves in time, i.e., there are dynamics and no guarantee of detailed balance; the number of "particles" and the energy are allowed to vary. Such a model is best described by the reactions which take

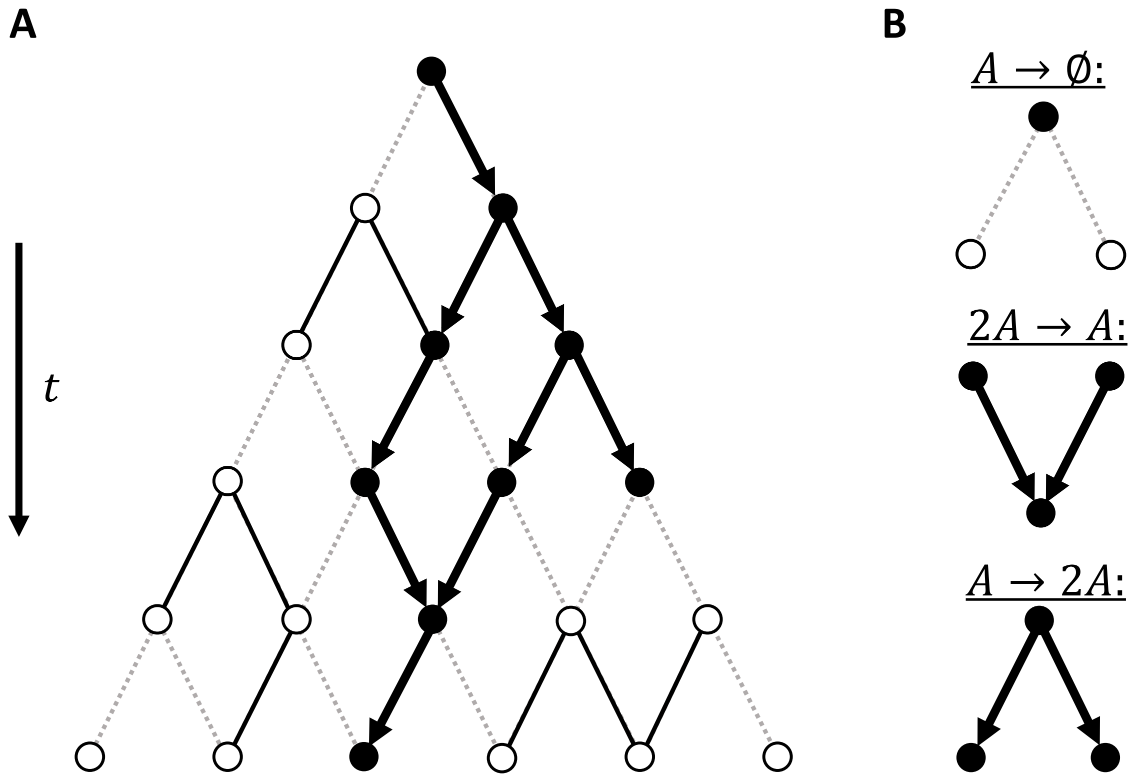

Figure 2.4: Bond directed percolation. **A.** Percolation of a fluid through a filter is represented by a triangular lattice with vertices representing pores and edges representing channels between pores. Channels have been randomly closed (dashed lines) or left open (solid lines) for particles (solid circles) to diffuse along; particle diffusion is represented by arrows. **B.** The allowed reactions are particle removal ($A \to \emptyset$), coalescence ($2A \to A$), and particle production ($A \to 2A$).

place within it and this is done with a master equation and to construct such an equation, we must be familiar with the involved reaction rates. Generally, we can write a master equation as

$$\frac{\partial P(x)}{\partial t} = \sum_{z} \left(W(z \to x)P(z) - W(x \to z)P(x) \right), \tag{2.20}$$

where $W(z \to x)$ and $W(x \to z)$ are the transition probabilities into and out of state x from another possible state z, some of which may depend on the probabilities $P(x)$ and $P(z)$, depending on the reaction. The probabilities $P(x)$ and $P(z)$ to find the system in states x and z, respectively, may be used to approximate corresponding population densities in a mean-field treatment. The master equation can thus be used to describe population dynamics for each of the involved species x. Because the movement of fluid through the filter is what we are interested in, the "involved species" are the wet sites A, which we interpret as particles undergoing reaction-diffusion processes: **particle removal** $A \to \emptyset$, in which a site with no open outbound channels becomes wet, and thus cannot wet any additional sites; **coalescence** $2A \to A$, in which two wet sites propagate to a single site, but only one particle is allowed per site (a site cannot be *doubly* wet); and **production** $A \to 2A$, where a single wet site produces two additional wet sites through its open outbound channels (see Figure 2.4B). To each of these situations, we assign reaction rates to arrive at an expression describing the particle density $\rho \equiv P(A)$ as a function of time t. We next develop the master equation in the mean field.

2.2.1 Mean-Field Directed Percolation

In the mean field, we assume translational invariance and approximate state probabilities by the appropriate particle densities. We are interested in the density of wet sites $P(A)$ and evaluate Equation 2.20 by considering each of the ways a site can become wet:

$$\frac{\partial \rho}{\partial t} = \mu_p \rho(t) - \mu_r \rho(t) - \mu_c \rho^2(t) + (1 - \rho(t))h, \tag{2.21}$$

where μ_p is the particle production rate, μ_r the particle removal rate, and μ_c the rate of coalescence; I have included here an external field h conjugate to $\rho(t)$ to allow for a treatment analogous to that presented in Section 2.1. From this expression, we determine fixed points ρ^*, corresponding to long-term behavior of the differential equation, to characterize the phases of the model and perform a stability analysis to determine the location of the phase transition. We determine fixed points of the differential equation by setting $\partial_t \rho(t)|_{\rho(t)=\rho^*} = 0$ and solving for ρ^*:

$$\rho^*_{\pm} = \frac{\tau - h \pm \sqrt{4gh + (h-\tau)^2}}{2g}, \tag{2.22}$$

where $\tau \equiv \mu_p - \mu_r$, $g \equiv \mu_c$. Stability of the fixed points is also determined in the usual way by taking the derivative of the right-hand side of Equation 2.21 with respect to $\rho(t)$, evaluating the resulting expression at $\rho(t) = \rho^*_{\pm}$, and determining the sign of the resulting expression. When $h = 0$, we find

$$\rho^* = \begin{cases} 0, & \text{when } \tau < \tau_c \\ \tau/g, & \text{when } \tau > \tau_c, \end{cases} \tag{2.23}$$

with $\tau_c = 0$. We have thus identified the absorbing phase where $\rho^* = \rho^*_- = 0$ and the active phase where $\rho^* = \rho^*_+ = \tau/g$, and the control parameter τ with which we can find our system in these phases. When $h \neq 0$, the only stable fixed point is ρ^*_+, i.e., the absorbing phase has disappeared and only an active phase remains for all values of τ. In analogy to the definition of the magnetic susceptibility given in Equation 2.7, we write the **dynamical susceptibility** as

$$\chi = \lim_{h \to 0} \frac{\partial \rho^*}{\partial h}. \tag{2.24}$$

Using

$$\frac{\partial \rho^*_+}{\partial h} = -\frac{1}{2g}\left(1 - \frac{2g + (h-\tau)}{\sqrt{4gh + (h-\tau)^2}}\right), \tag{2.25}$$

we arrive at $\chi \propto |\tau|^{-1}$, and so the value of the associated mean-field exponents is $\gamma = \gamma' = 1$. We have thus determined that the **absorbing phase transition** occurs at $\tau = \tau_c$ with order parameter ρ^* when $h = 0$. The mean-field critical exponent β is determined directly from Equation 2.23, where we note that $\rho^* \propto (\mu_p - \mu_r)^\beta$ for $\mu_p > \mu_r$, and thus $\beta = 1$.

As in Section 2.1, we find here that the dynamical susceptibility still features a peak when $h \neq 0$, finding a **nonequilibrium Widom line** given by $\tau_w(h) = -h$. We have thus presented the meaning of critical phase transitions in both equilibrium and nonequilibrium systems, demonstrating that our equilibrium analysis can be extended to nonequilibrium systems—a nontrivial result. We will employ these concepts in subsequent chapters as we examine nonequilibrium neural network models in both weakly-driven ($h = 0$, as in self-organized criticality) and strongly-driven ($h \neq 0$, as in quasicriticality) regimes.

CHAPTER 3

Self-Organized Criticality

Self-organized criticality (SOC) is a framework which has been proposed to explain the ubiquitous scale-free behavior observed in a large variety of natural phenomena. These systems were purported to *self-organize* to critical points, such as those presented in Chapter 2, via interactions between their elements and their intrinsic dynamics. In other words, a critical point served as an attractor of the dynamics of these systems. In the context of neural network dynamics, the SOC framework was used to develop the **criticality hypothesis**, which has been stated as

> "Living systems will self-organize to operate near a critical point."

The criticality hypothesis had been based on simulation and modeling work which predicted such behavior as well as experimental evidence which appeared to support it [39]. In this chapter, we will review two models which exhibit nonequilibrium critical phase transitions, the first of which does so within the framework of SOC. The Bak-Tang-Wiesenfeld (BTW) sandpile model describes the emergence of a critical slope in a growing pile of sand, and serves as a "hydrogen atom" of SOC, i.e., a simplified, analytically-tractable toy model. Other models exhibiting SOC exist, including the Olami-Feder-Christensen earthquake model, the Oslo ricepile model, and a number of forest-fire models [22]. These models played a key role in the development of the SOC framework.

The second model, the cortical branching model (CBM), describes a stochastic branching process in a cortical neural network. In contrast to mechanistic models of neural network dynamics, the CBM initially represented a “parsimonious approach” for describing mesoscopic neural network dynamics, such as those observed using microelectrode arrays, i.e., individual elements in the model represented individual microelectrodes [23]. In the latest manifestations of the CBM, the model is extended to describe microscopic dynamics and interactions between individual neurons [19, 58]. The CBM is not capable of *self-organizing* to a critical point; as I will demonstrate, it must be fine-tuned to a critical point and hence it does not strictly fall under the SOC framework.

Realizations of both of these models in this chapter will feature a full separation of driving and relaxation timescales, as this is a fundamental requirement for SOC; a generalization of the CBM which does not feature a complete separation of timescales will be explored in Chapter 4.

3.1 The Bak-Tang-Wiesenfeld Model

The BTW model is a cellular automaton which exhibits SOC in $d \geq 2$ dimensions [20, 22, 51]. Conceptually, the model works by dropping “grains” of sand on a square lattice[1], where each lattice site i is allowed to accumulate these “grains” up to a certain threshold height z^{th}, at which point the site will topple its grains to its neighboring sites $\mathcal{N}(i)$, which may induce further topplings. These topplings constitute **avalanches**, whose sizes are given by the number of topplings involved in such a relaxation event. In the thermodynamic limit, avalanche sizes obey power-law scaling and thus fluctuations occur over all length scales, suggesting a diverging correlation length, which may indicate criticality [20]. The algorithm for the conservative two-dimensional case (also known as the 2D Abelian sandpile model) is presented below:

---

[1] The BTW model produces similar results, with identical critical exponents in a triangular lattice [59].

1. *Initialization.* Start board in random configuration $z_i \leq z^{th}$.

2. *Drive.* Drop a grain on a random site i: $z_i \rightarrow z_i + 1$.

3. *Relaxation.* For all sites i with $z_i \geq z^{th}$, topple one grain to each of its neighboring sites: $z_i \rightarrow z_i - 4$ and $z_{\mathcal{N}(i)} \rightarrow z_{\mathcal{N}(i)} + 1$. Grains are conserved within the bulk, where each site has four neighbors, but not at the edges, where sites can have as few as two neighbors. Continue until $z_i \leq z^{th}$ for all sites i.

4. *Iteration.* Return to **2.**

There are two key details to emphasize here. First, there is a separation of timescales in that driving occurs at a rate much slower than the relaxation and grains are only dropped after the previous avalanche has finished. Second, there is a direct causal relation between toppling events and subsequent toppling events are separated by a single timestep.

3.1.1 The Random-Neighbor Mean-Field Approximation

In developing a mean-field approximation, it is useful to employ the random-neighbor variant of the Abelian sandpile model. Instead of choosing the neighbors $\mathcal{N}(i)$ of site i depending on the location of that site, i.e., at the edges or in the bulk, we implement a translational invariance by considering each site to have $|\mathcal{N}| = 4$, randomly-chosen neighbors. This situation is compatible with the thermodynamic limit. We desire a master equation to describe the dynamics and determine the steady state behavior. Such an equation would allow us to determine the fractions of sites with z grains at a time t; in the thermodynamic limit, these are approximated by the probabilities $P_z(t)$. The master equation takes the form

$$P_z(t+1) = \sum_{z'} \left(W(z' \rightarrow z) P_{z'}(t) - W(z \rightarrow z') P_z(t) \right), \tag{3.1}$$

where $W(z' \to z)$ is the fraction of sites whose heights change from some z' to z, and $W(z \to z')$ is the fraction of sites whose heights change from z to z'. Restricting our analysis to $z < z^{th}$, $W(z \to z')$ is proportional to the number of times a site is chosen as a random neighbor, which means that, in the thermodynamic limit, $W(z \to z') \approx 0$.

The probability that a single toppling will induce n additional topplings will depend on the states of neighboring sites, specifically it will depend on the probability $P(z^{th} - 1)$ that the site has n neighbors with a height of $z^{th} - 1$:

$$p_n = \binom{|\mathcal{N}|}{n} (P(z^{th} - 1))^n (1 - P(z^{th} - 1))^{|\mathcal{N}| - n}. \tag{3.2}$$

Since all the heights are randomly established with $z < z^{th}$ at the outset, we have that $P_z = 1/z^{th}$ for any $z < z^{th}$, and so $P(z^{th} - 1) = 1/z^{th}$.

3.2 The Cortical Branching Model

The cortical branching model (CBM) is a nonequilibrium stochastic cellular automata model of cortical dynamics which has proven useful in capturing many features of neural network data [19, 23, 24, 60, 58]. In the CBM, model neurons, which are called **nodes**, lie at the vertices of a directed graph representing a neural network. Each node can be in a number of different states: quiescent, active, or refractory. To become active, a node must first be quiescent; following activation, the node immediately becomes refractory for some amount of time. The presence of refractory periods indicates the CBM features non-Markov dynamics, i.e., the state of a node depends on not only the prior timestep, but a number of timesteps before the present, depending on the duration of the refractory period; the CBM has memory. Modeling non-Markov dynamics can be difficult, however, in this case, we can circumvent these difficulties by adding into the model additional states to create a Markovian model. Each node can hence be in a number of states, two of which represent **quiescence** and the firing of an action potential (i.e., **activation**), with additional states to represent the duration of neuronal refractory periods. Neuronal states are thus modeled as *clock* degrees of freedom, i.e., from quiescence follows activation, followed by a series of refractory states during which the node cannot become active, and concluding with an eventual return to quiescence. In the mean time, neuronal activity spreads through probabilistic model synapses, represented by the edges of the directed graph. The CBM is a "top-down" model in that it is not microscopically accurate, instead it provides a metaphor of neural network dynamics which relies on fundamental aspects of neural network dynamics.

Inhibitory nodes might be modeled as contributing to dynamical, heterogeneous spontaneous activation probabilities and connections. Further enhancements might include dynamical refractory periods whose durations would depend on the recent state of the network; refractory periods and levels of inhibition would increase during bursts of activity. This dynamical disorder then presents a fluctuating bottleneck which may amplify small signals, but prevents runaway activity.

3.2.1 Formal Description

What follows is a formal description of the CBM [19]. Consider a random directed network of N nodes, where connections and their relative strengths are established at the outset and kept fixed throughout the dynamics, as in quenched disorder. Random networks can either be *strongly-connected*—in which case there exists a path (never running anti-parallel through directed connections) from any node in the network to any other node on the network (through possibly many intermediaries)—or *weakly-connected*—in which case the network contains disjoint subgraphs and is said to not be fully-connected. Networks are generated randomly and tested for connectedness by examining the corresponding adjacency matrix associated with its graph. In this study, only strongly-connected networks are considered, i.e. those with *irreducible* adjacency matrices [61]. See Figure 3.1 for a sample network.

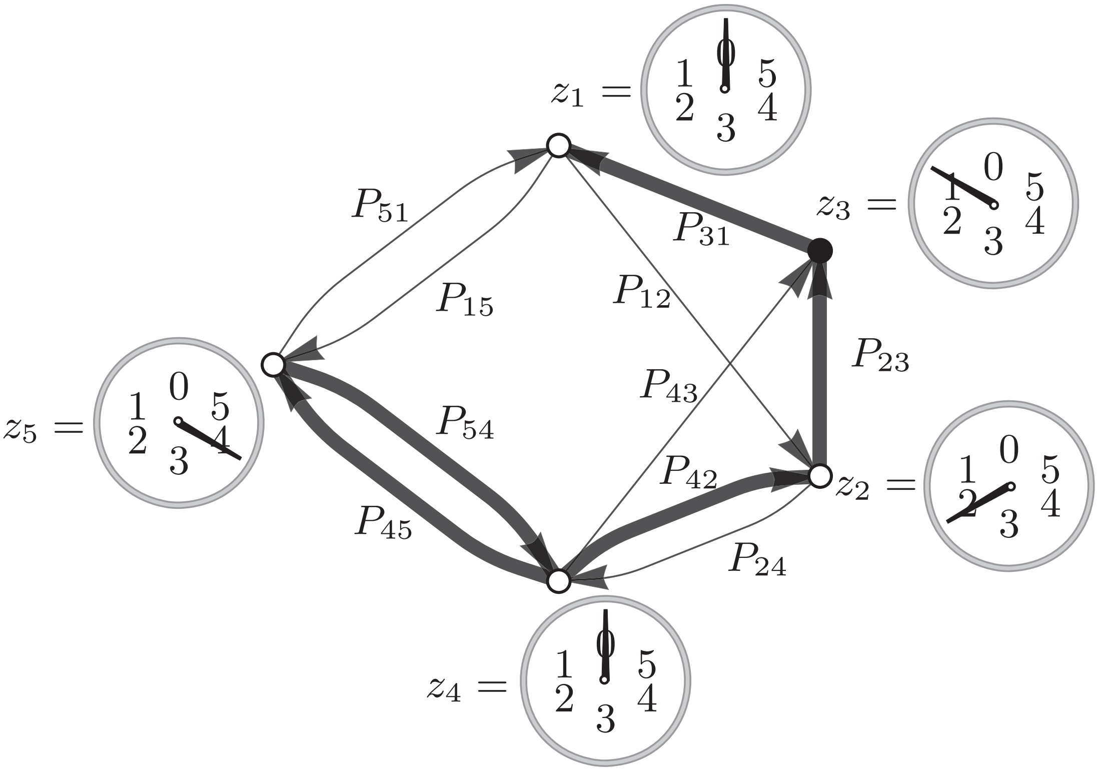
$z_1 =$
$z_2 =$
$z_3 =$
$z_4 =$
$z_5 =$
0
1
2
3
4
5
P_{51}
P_{15}
P_{31}
P_{12}
P_{23}
P_{43}
P_{54}
P_{42}
P_{45}
P_{24}

Figure 3.1: A randomly-generated network of $N = 5$ nodes (vertices). Each node has $k_{in} = 2$ incoming connections (edges), each of which are weighted; the thickness of the edges illustrate the connection strengths P_{ij}. Node 3 is active ($z_3 = 1$); nodes 1 and 4 are quiescent ($z_i = 0$ for $i = 1, 4$); and nodes 2 and 5 are refractory.

The network structure is described by the weighted adjacency matrix P, with elements $0 \leq P_{ij} \leq 1$ representing the probability that a connection from node i to node j will transmit activity. In principle, the P_{ij}'s can be any of any value so long as they are probabilities, but in order to facilitate control of activity spreading, we require that, for any site i,

$$\sum_{k=1}^{k_{out}^{(i)}} P_{in_i(k)} = \kappa, \tag{3.3}$$

where κ is the branching parameter, i.e., the spectral radius of the matrix P, $k_{out}^{(i)}$ is the out-degree of node i, and $n_i(k)$ is the kth element of the set $n_i = \{j_k\}$ containing indeces of nodes postsynaptic to node i, i.e., $k_{out}^{(i)} = |n_i|$. For example, in Figure 3.1, node 2 has $k_{out}^{(2)} = 2$ outgoing connections, one to node 3 and the other to node 4, and so $n_i = \{3, 4\}$.

In our implementation of the CBM, we consider random networks connecting nodes with a fixed in-degree k_{in}, i.e., each model neuron has a fixed number of presynaptic model neurons. This is done to facilitate not only generation of the networks, but also quantitative analysis in the mean field. Network connections are generated randomly, so we expect the average out-degrees $k_{out}^{(i)}$ for each node i will equal the fixed in-degree, i.e., $\langle k_{out}^{(i)} \rangle_i = k_{in}$. Each connection is then weighted according to the following function:

$$P_{ij} = \kappa p_{n_{ij}} = \kappa \frac{e^{-Bn_{ij}}}{\sum_{n=1}^{k_{in}} e^{-Bn}}, \tag{3.4}$$

where k_{in} is the in-degree at each node (which we constrain to be fixed), B is the connection bias, and $n_{ij} \in \{1, \cdots, k_{in}\}$ in an integer which ranks each connection inbound at node j by strength, e.g., $n_{ij} = 1$ corresponds to the strongest connection from node i to node j. The branching parameter κ must be restricted to the range $[0, \kappa_{max}]$ such that all P_{ij}'s remain well-defined as probabilities. The upper bound is then given by $\kappa_{max} = e^{B} \sum_{n=1}^{k_{in}} e^{-Bn}$ and the lower bound corresponds to a fully-disconnected network. Close to $\kappa = \kappa_{max}$, the CBM produces constant activity. It had previously been determined that for a network of $N = 60$ nodes, each with a fixed $k_{in} = 10$, that the values $B = 1.2$ and $B = 1.6$ allowed for a reasonable fit to the local field potential (LFP) dynamics recorded from living neural networks [24]; my primary simulation results have been obtained using $B = 1.4$ and $k_{in} = 3$.

3.2.2 Cellular Automata Rules

The state of each node i is described by a dynamical state variable $z_i \in S$, where $S = \{0, 1, 2, \ldots, \tau_r\}$, $\tau_r \geq 1$ is the integer-valued refractory period, i.e. the number of timesteps following activation during which a node cannot be made to activate. For example, in Figure 3.1, $\tau_r = 5$. The configuration space of the CBM is given by $\mathcal{C} = \{Z = (z_1, z_2, \ldots, z_N)|z_i \in S\}_{i=1,N}$, where $|\mathcal{C}| = (\tau_r + 1)^N$; for example, $\mathcal{C} = \{(0,0); (0,1); (1,0); (1,1)\}$ for a system of $N = 2$ and $\tau_r = 1$. A node i is said to be *active* when $z_i = 1$, *inactive* (i.e. quiescent) when $z_i = 0$, and *refractory* at any other value. Nodes can only be active for a single timestep at a time and can be activated spontaneously with probability p_s or driven to activate by the active nodes in the previous timestep.

The number of timesteps between spontaneous activations, Δt_s, is determined by a discrete probability distribution of our choice. A Poisson distribution with rate $1/(p_s N)$, i.e.,

$$P(\Delta t_s) = \frac{e^{-1/p_s N}}{(p_s N)^{\Delta t_s} \ \Delta t_s!}, \tag{3.5}$$

allows for a greater separation of driving and relaxation timescales, such as that seen in instances of SOC [51, 62], thus minimizing the occurrence of overlapping avalanches. By using a geometric distribution with success probability $p_s N$, i.e.,

$$P(\Delta t_s) = (1 - p_s N)^{\Delta t_s - 1} p_s N, \tag{3.6}$$

avalanches are, however, more likely to overlap and contain a mixture of spontaneous and driven events. Simulation results presented in Chapter 4 utilize Poisson-distributed spontaneous events to generate avalanches, in an approximation to SOC.

Nodes can also be driven to activate by the nodes connected to it with probabilities of the form given in Equation 3.4, but only if the driving node was active and the driven node quiescent in the preceding timestep. A node's dynamical variable z_i changes deterministically following activation, increasing by 1 every timestep until $z_i = \tau_r$ is reached, after which the node becomes quiescent ($z_i = 0$) until it is stochastically activated once again. Thus, each state variable z_i represents a *clock* degree of freedom. For example, consider a node i with $\tau_r = 3$: following the timestep during which it was active, this node will become refractory, its state deterministically changing from $z_i = 2$ to $z_i = 3$, and finally to $z_i = 0$. The CBM is summarized in the following algorithm:

1. *Initialization.* Prepare nearest neighbor connections by randomly assigning connections between nodes while keeping the in-degree k_{in} fixed (parallel connections are allowed; loops are not) and prepare connection strengths P_{ij} as given by Equation (3.4). Initialize the system in the only stable configuration, i.e., $z_i = 0$ for all nodes i. Prepare the first spontaneous activation(s) at $t = 1$ and subsequent spontaneous activation times by drawing inter-activation intervals Δt_s from a specified distribution.

2. *Drive.* For each spontaneous activation time equal to the current time step t, randomly select a node j to activate, $z_j(t) \rightarrow 1$; if however node j was not initially quiescent (i.e. $z_j(t) = 0$), then spontaneous activation does not occur at node j.

3. *Relaxation.* Any nodes i for which $z_i(t-1) \neq 0$: $z_i(t) = z_i(t-1) + 1$. If $z_i(t) > \tau_r$, then $z_i(t) \rightarrow 0$. Node j, having been active at time step t, will influence the activity of a neighboring node k at time step $t+1$ with probability P_{jk}, but only if $z_k(t+1) = 0$: $z_k(t+1) \rightarrow z_k(t+1) + 1$.

4. *Iteration.* Start the next time step: Return to **2.**

The CBM features its own neural network analog of the avalanches seen in the BTW model, called **neuronal avalanches**, which may occur spontaneously (when the spontaneous activation probability, p_s, is non-zero) or may be triggered by a single activation (in this way simulating the case $p_s = 0$). In this chapter, only the case of triggered avalanches will be considered, while a CBM with spontaneous events is considered in Chapter 4. Neuronal avalanches exhibited by the CBM mimic spatiotemporal patterns observed in living neural networks [23, 24], where they were defined as periods of neuronal activity spanning a number of adjacent time windows whose width were determined by the MEA amplifier sampling rate—typically 250 Hz to 1 kHz, corresponding to 1 ms to 4 ms long windows. Neuronal avalanches correspond to fluctuations in the **density of active nodes**, $\rho_1(t)$, defined as

$$\rho_1(t) = \frac{1}{N} \sum_{i=1}^{N} \delta_{z_i(t),1}, \tag{3.7}$$

at time t. We will return to this quantity, as it will be determined to be an order parameter of the CBM. Features and properties of neuronal avalanches are described below. See Appendix A.1 for a MATLAB code to run simulations of the CBM.

3.2.3 Avalanche Shape

Many properties of neuronal avalanches are encoded in the **avalanche shape**, which we define as the density of active nodes over the duration of an avalanche, resembling definitions given in previous studies [63]. The avalanche shape vector X_q gives the shape of the qth avalanche:

$$X_q(\phi) = \sum_{i=1}^{N} \delta_{z_i(t_q^0+\phi-1),1}, \tag{3.8}$$

where t_q^0 is the avalanche starting time, d_q is its **duration**, and $\phi = [1, d_q] \in \mathbb{Z}^+$ indexes the number of timesteps within the avalanche. From this, the **size** of the qth avalanche is written as $s_q = \sum_{\phi=1}^{d_q} X_q(\phi)$, which corresponds to the number of MEA electrodes participating in the avalanche.

Avalanche size and duration probability distributions have been conjectured [14] to follow power laws, $P(s) \propto s^{-\tau}$ and $P(d) \propto d^{-\alpha}$. In simulated and living neural networks, values of these exponents have been found to be $\tau \approx 1.5$ and $\alpha \approx 2$ for LFP data and $\tau \approx 1.6$ and $\alpha \approx 1.7$ for neuronal spike data; results which have been used to support the criticality hypothesis [23, 64, 65].

3.2.4 Avalanche Branching Ratio

Here I briefly discuss two different definitions of the branching ratio which I have encountered in the literature. In the context of living neural networks, the **branching ratio** σ has been defined as the average number of descendant activations within an avalanche [14]. This is the analog of the definition given in the context of the BTW sandpile model [51, 66]. For a particular avalanche q, this corresponds to the total number of events in the timesteps $\phi \in [2, d_q]$ divided by the duration of the avalanche d_q, i.e.,

$$\sigma_q = \frac{1}{d_q} \sum_{\phi=1}^{d_q - 1} X_q(\phi + 1). \tag{3.9}$$

For a particular node i, the average number of descendants is approximately equal to the sum of the transmission probabilities P_{ij} emanating from i and so σ_q is, on average, equal to the Perron-Frobenius eigenvalue κ if $P_{ij} = \kappa p_j$ and $\sum_j p_j = 1$ for all pairs of nodes (i, j). We can then approximate the branching ratio using information of the network structure:

$$\sigma_q \approx \frac{1}{s_q} \sum_{\mu=1}^{s_q} \sum_{j=1}^{k_{out}^{(x_\mu(1))}} P_{x_\mu(1), j}, \tag{3.10}$$

where the first sum is taken over the elements of the set of activations within avalanche q, $A(q) = \{x_\mu\}$, where $x_\mu = (i, \phi)$ is an ordered set indicating activation of node i at timestep ϕ within the avalanche; $x_\mu(1) = i$. The cardinality of the set $A(q)$ is equivalent to the size of the avalanche s_q. As defined in [65] and used in [23], however, the branching ratio is defined as the ratio of the number of activations between adjacent timesteps, i.e.,

$$\sigma_q = \frac{1}{d_q} \sum_{\phi=1}^{d_q - 1} \frac{X_q(\phi+1)}{X_q(\phi)}. \tag{3.11}$$

If we consider only tree-like avalanches initiated by a single activation, i.e., those with $X(1) = 1$, with the above restrictions on the P_{ij}'s, then this expression becomes a sum in powers of κ,

$$\sigma_q = \frac{1}{d_q} \sum_{\phi=1}^{d_q - 1} \frac{\kappa^{\phi}}{\kappa^{\phi-1}}, \tag{3.12}$$

which reduces to $\sigma_q = \kappa$ in the thermodynamic limit and hence the two are asymptotically equivalent. Strictly speaking, however, the definitions given in Equations 3.9 and 3.11 are not equivalent. In order to address this discrepancy, we must return to the motivation behind the definition of such a quantity, i.e., to quantitatively describe the excitability of a network by counting the average number of activations which follow from a single event. When using neural network data, however, this is not straightforward, as detailed information of the network and causal structure of the dynamics is necessary to accurately define such a quantity, particularly in the presence of synaptic delays and absence of a separation of timescales. This is addressed in Chapter 5, where I define the **branching fraction** of an alternative to neuronal avalanches, termed causal webs.

3.3 A Mean-Field Approximation of the CBM

To gain a deeper understanding of our CBM and its nonequilibrium phase diagram, we next develop an analytical mean-field approximation. In the mean-field approximation, a typical, *representative* node and its local neighborhood of interaction (i.e. the k_{in} sites which directly influence its behavior) are used to approximate the behavior of the network as a whole—the key presumption here being that transition probabilities are translationally invariant in the thermodynamic limit and beyond the upper critical dimension. We would expect the mean-field approach to represent a faithful approximation of the simulation results when the simulated graph is **irreducible**, i.e., the probability for an excitation originating at one node to influence any other node in the network is nonzero. The simulated graphs then contain no subgraphs which are inaccessible; the graph can be said to be *fully connected* [61]. It is an extremely interesting question to explore the cases where the graph is reducible, but this is beyond the scope of this work.

The cellular automaton rules of the CBM (described above in Section 3.2) are approximated by a Markovian stochastic process and so the probability that a particular node will be in a specific state is given by the Chapman-Kolmogorov equation [67]:

$$P(z_r(k+1)=z) = \sum_{\mathbf{z}\in S^{k_{in}+1}} W(\mathbf{z}\to z)\prod_{i=0}^{k_{in}} P(z_i(k)), \tag{3.13}$$

where z is an element in the state space $S = \{0, ..., \tau_r\}$, $r \in \{0, ..., k_{in}\}$ identifies the nodes (with $r = 0$ corresponding to the representative node), $\mathbf{z} = (z_0, ..., z_{k_{in}})$ is the configuration of the system (i.e. a vector whose elements are the states of the representative node and its local neighborhood of interaction), and $W(\mathbf{z} \to z)$ is the probability that the $r = 0$ node will transition into state z given the system configuration $\mathbf{z}$. At a particular iteration of the mean-field map, k, the probability that a node r is in state z is equivalent to the fraction of nodes $x_z(k)$ in state z, i.e.,

$$P(z_r(k)=z) = x_z(k) = \frac{1}{k_{in}+1}\sum_{i=0}^{k_{in}} \delta_{z_i(k),z}. \tag{3.14}$$

Additionally, because we are primarily interested in the density of active nodes x_1 and because a node must be quiescent at k to become active at $k+1$, we rewrite Equation 3.13 as

$$x_1(k+1) = x_0(k)\sum_{\mathbf{z}'\in S^{k_{in}}} W(\mathbf{z}'\to 1)\prod_{j=1}^{k_{in}} x_{z_j}(k), \tag{3.15}$$

where $\mathbf{z}'$ is the configuration of the local neighborhood *excluding* the representative node, i.e. $\mathbf{z}' = (z_1, ..., z_{k_{in}})$. We write a general expression for the transition probabilities $W(\mathbf{z}' \to 1)$

as one minus the probability that a node will remain quiescent, or

$$W(\mathbf{z}' \to 1) = 1 - \prod_{j=1}^{k_{in}} (1 - \kappa p_j \delta_{z_j,1}), \tag{3.16}$$

where the connection strengths p_j are of the form given by Equation 3.4. Because z varies deterministically following activation, $x_z(k+1) = x_{z-1}(k)$ for $z \in \{2, ..., \tau_r\}$.

Along with Equation 3.15, these equations form a nonlinear, autonomous $(\tau_r + 1)$-dimensional map of first order (i.e. Markovian). By including the restriction that, at any iteration t, $\sum_{z=0}^{\tau_r} x_z(k) = 1$, we reduce the dimension to τ_r. This map then allows us to calculate the mean-field densities of quiescent ($z = 0$), active ($z = 1$), and refractory nodes ($z > 1$). As I have mentioned previously, an equivalent mean-field approximation can be formulated as a non-Markovian τ_rth-order map in one dimension. Finally, we note that increasing the refractory period by a single timestep increases the number of equations by one; whereas increasing k_{in} increases the order of polynomial to be solved. Fixed points x_1^* of this map give approximate densities of active sites, i.e. mean-field approximations to Equation 3.7. Stability of each fixed point is determined as usual by calculating the eigenvalues of the $\tau_r \times \tau_r$ Jacobian matrix J associated with the map, which will have the form

$$J = \begin{pmatrix} A & B & B & \cdots & B & B \\ 1 & 0 & 0 & \cdots & 0 & 0 \\ 0 & 1 & 0 & \cdots & 0 & 0 \\ \vdots & \vdots & \vdots & \ddots & \vdots & \vdots \\ 0 & 0 & 0 & \cdots & 1 & 0 \end{pmatrix}, \tag{3.17}$$

where $A = \partial x_1(k+1)/\partial x_1(k)$ and $B = \partial x_1(k+1)/\partial x_z(k)$ for $z \in \{2, ..., \tau_r\}$. If each of the eigenvalues of J when evaluated at a certain fixed point x_1^* have modulus less than one, then that fixed point is stable.

We first consider the simplest case, i.e., that with $k_{in} = 1$. The mean-field approximation in this case is given by the quadratic map

$$\begin{aligned} x_1(k+1) &= \left(1 - \sum_{z=1}^{\tau_r} x_z(k)\right) c\, x_1(k) \\ x_z(k+1) &= x_{z-1}(k), \text{ for } z = \{2, \cdots, \tau_r\}, \end{aligned} \tag{3.18}$$

where $c = \kappa p_1(1 - p_s)$, i.e., $c = \kappa p_1$ when $p_s = 0$. This yields two fixed points: $x_1^* = 0$ and $x_1^* = (1 - 1/\kappa p_1)/\tau_r$. The vanishing fixed point becomes unstable when $\kappa > 1$ and so the stable fixed point acts as a Landau order parameter, i.e. $\bar{\rho}_1 = 0$ for $\kappa < \kappa_c$ and $\bar{\rho}_1 > 0$ for $\kappa > \kappa_c$, with the critical point at $\kappa_c = 1$. We find the critical exponent $\beta = 1$: $x_1^* \propto (\kappa - \kappa_c)^\beta$ for $\kappa > \kappa_c$. As in Equation 2.7, we write the susceptibility

$$\chi = \lim_{p_s \to 0} \frac{\partial \bar{\rho}_1}{\partial p_s}, \tag{3.19}$$

finding that it diverges at κ_c with exponent $\gamma' = 1$ for $\kappa < \kappa_c$: $\chi \propto (\kappa_c - \kappa)^{-\gamma'}$. For $\kappa > \kappa_c$, it diverges with exponent $\gamma = 1$: $\chi \propto (\kappa - \kappa_c)^{-\gamma}$.

It is remarkable to note that the $k_{in} = 1$ CBM mean-field approximation is the discrete-time equivalent of the directed percolation mean-field equation when $\tau_r = 1$:

$$\partial_t \rho_1(t) = -c\rho_1(t)^2 + (c - 1 - p_s)\rho_1(t) + p_s \tag{3.20}$$

as given in [54] and presented in Section 2.2, where p_s plays the role of the external field. These two seemingly different processes are therefore related even when $p_s \neq 0$. We note that the CBM has a continuous phase transition when $p_s = 0$, characterized by the order parameter $\bar{\rho}_1$, but that transition disappears when $p_s \neq 0$, as will be demonstrated in Chapter 4. The case $p_s = 0$ is consistent with the Janssen-Grassberger conjecture [55, 56], which states that a model with a continuous phase transition should belong to the DP universality class if the transition is characterized by a non-negative one-component order parameter, among other conditions (cf. Section 2.2).

In the case $k_{in} = 2$, the mean-field approximation produces the following cubic map:

$$x_1(k+1) = \left(1 - \sum_{z=1}^{\tau_r} x_z(k)\right) \left(-\kappa^2 p_1 p_2 x_1^2(k) + \kappa x_1(k)\right)$$

$$x_z(k+1) = x_{z-1}(k), \text{ for } z = \{2, \cdots, \tau_r\}. \tag{3.21}$$

where we again have a vanishing fixed point, $x_1^* = 0$, but now also a pair of real, non-zero fixed points given by

$$x_{1\pm}^* = \frac{\kappa p_1 p_2 + \tau_r \pm \sqrt{(\kappa p_1 p_2 + \tau_r)^2 - 4 p_1 p_2 \tau_r (\kappa - 1)}}{2\kappa p_1 p_2 \tau_r}. \tag{3.22}$$

Stability of the fixed points again changes at $\kappa_c = 1$. The fixed point $x_1^* = 0$ is stable when $\kappa < \kappa_c$ for any value of τ_r; this defines the *disordered phase.* Stability shifts to the fixed point x_{1-}^* when $\kappa > \kappa_c$—defining the *ordered phase*—but only for small values of τ_r. Expanding x_{1-}^* around $\kappa = \kappa_c$, we again find $x_{1-}^* \propto (\kappa - \kappa_c)^\beta$ with $\beta = 1$. The zero-field dynamical susceptibility is then found to be

$$\chi(\kappa) = \frac{f}{g(p_s = 0, \kappa)}, \tag{3.23}$$

where $f = 1 + (p_1 p_2 - 1)x^* - p_1 p_2 x^{*3}$ and $g(p_s, \kappa) = (1 - \kappa) + (1 + \kappa)p_s - 2(\kappa + p_1 p_2)(p_s - 1)x^* + 3 p_1 p_2 (p_s - 1)x^{*2}$, where x^* is 0 below the critical point ($\kappa < \kappa_c$) and x_{1-}^* above it ($\kappa > \kappa_c$). Critical exponents of $\chi(\kappa)$ below and above the critical point are hence found to be $\gamma' = 1$ and $\gamma = 1$, respectively. Note that $\chi(\kappa)$ diverges at $\kappa_c = 1$ only when $p_s = 0$.

With $B = 0.5$, $\kappa = 1.6$, and $\tau_r \geq 9$, the fixed point x_{1-}^* loses stability via a pair of complex conjugate eigenvalues crossing the unit circle, as in a Neimark-Sacker bifurcation (see Appendix B. Indeed this defines a new phase boundary which separates the ordered phase from an *entirely different* phase, where no stable fixed points exist, and the CBM exhibits **quasiperiodic** behavior (see Figure 3.2). In fact, for large τ_r, all fixed points of the $k_{in} = 2$ mean-field lose stability and the mean-field density of active nodes $x_1(k)$ subsequently exhibits oscillatory behavior as presented in Figure 3.3; similar quasiperiodic oscillations have

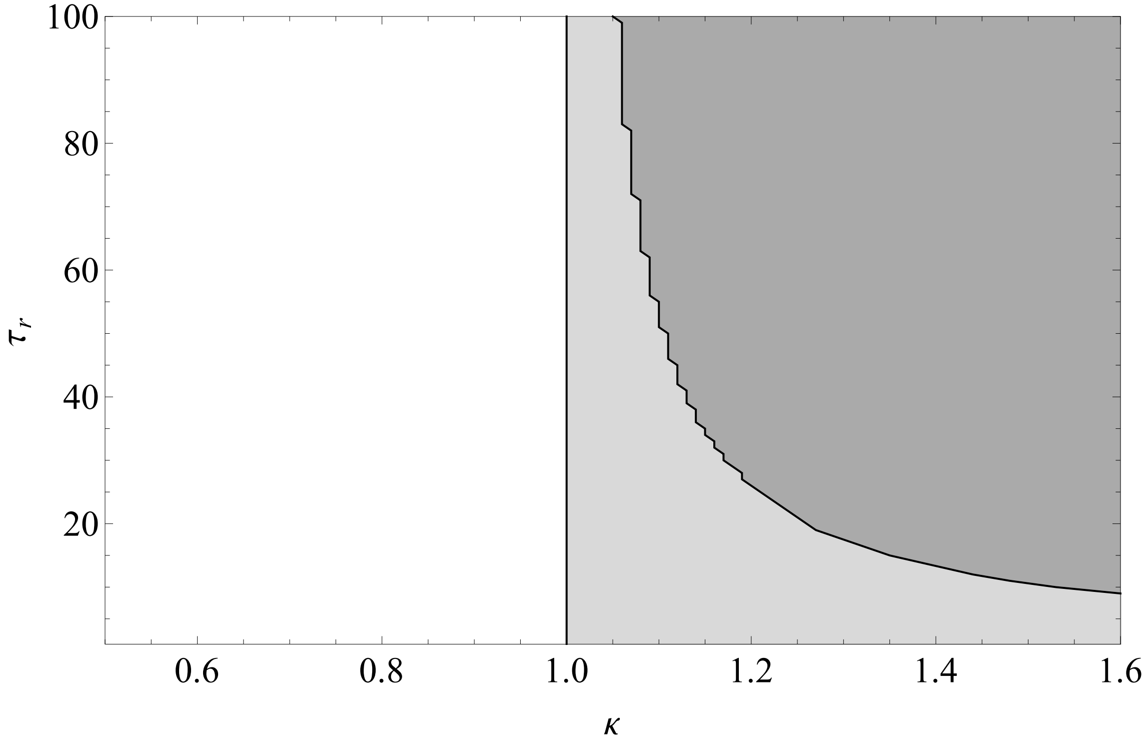

Figure 3.2: Nonequilibrium mean-field phase diagram for $k_{in} = 2$, at $p_s = 0$. The white region corresponds to the subcritical disordered phase with a vanishing stable fixed point; the light-gray region corresponds to the supercritical ordered phase with a nonzero stable fixed point; the dark-gray region corresponds to an "oscillatory" quasiperiodic phase, where all fixed points are unstable. Solid black lines are lines of non-analyticity and thus represent phase boundaries.

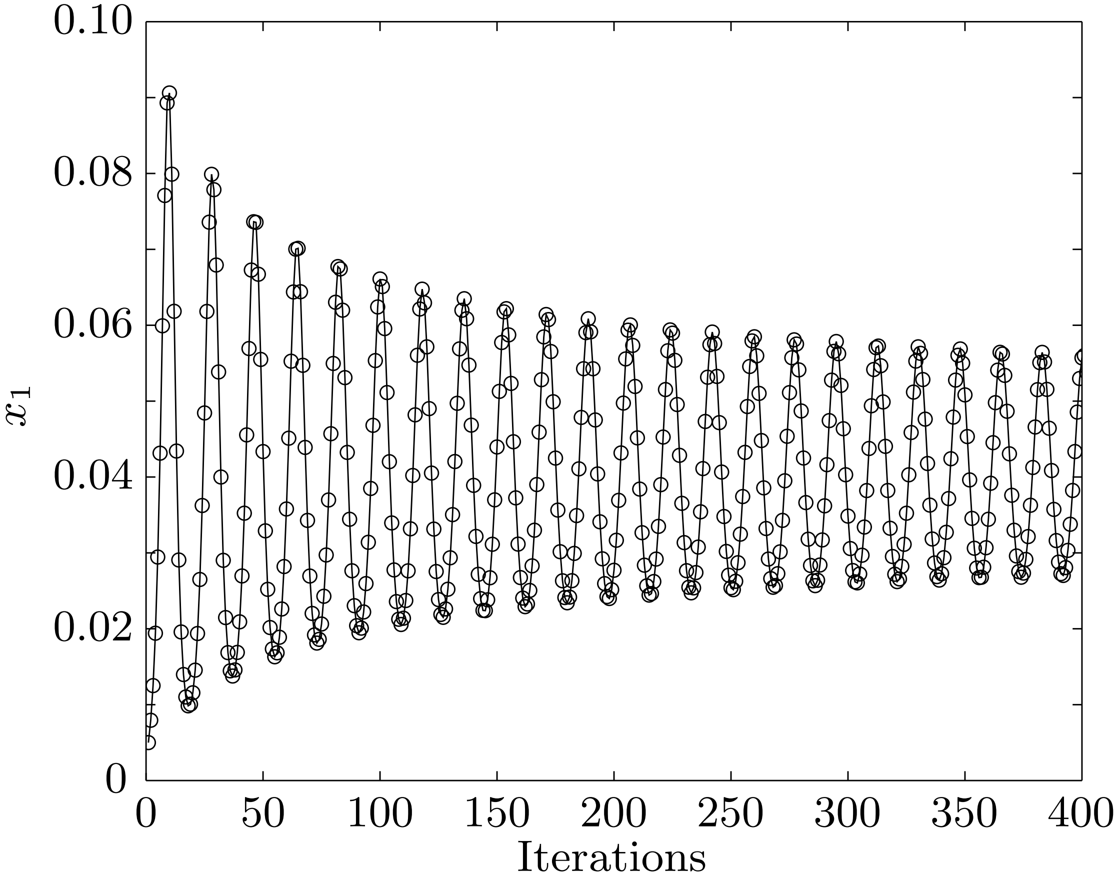

Figure 3.3: CBM mean-field density of active nodes over 400 iterations to show detail of the quasiperiodic behavior; $k_{in} = 2$, $B = 0.5$, $\kappa = 1.60$, $\tau_r = 9$, $p_s = 0$. The oscillations continue indefinitely.

previously been observed in SIRS-like models [68]. Within this quasiperiodic phase, $x_1(k)$ does not converge to a fixed-point and periodic points are not present; the oscillations are hence "quasiperiodic". The envelope of $x_1(k)$ is, however, sinusoidal here (see Figure 3.3). Oscillatory behavior emerging at large refractory periods had previously been observed in neural network models [27, 69, 70], but the quasiperiodic behavior observed here and in [68] was not found. It should be noted that Curtu and Ermentrout's model involved both excitatory and inhibitory elements whereas the CBM only involves excitatory elements [70].

At similar parameter values, simulations of the CBM exhibit oscillatory behavior when

$p_s \neq 0$. In the following chapter, I describe this generalization of the CBM which does not feature a critical transition. A more detailed analysis of the quasiperiodic phase can be found in Appendix B.

CHAPTER 4

The Quasicriticality Hypothesis

In this chapter, I will consider situations where there is no longer a separation of timescales. Specifically, I will explore the behavior of the BTW model (in Appendix C) and CBM when driving can occur during relaxation, i.e., in the case of a *strongly-driven* system. SOC should not be expected in such situations since, as shown in Section 2.1, the presence of an external influence induces an explicit symmetry breaking, and the subsequent disappearance of criticality. In the following sections, the external influences will be modeled as events which occur randomly according to some spontaneous activation probability, p_s. These events can be distributed to precisely control the degree to which the driving and relaxation timescales are mixed. When the external driving is present, we indeed find that the phase transition disappears and hence argue that criticality is not attainable by living neural networks, or any living system in general. We developed a more rigorous quantitative formulation and extension of the criticality hypothesis of Chapter 3 to open systems featuring a mixture of driving and relaxation timescales, known as the **quasicriticality hypothesis**:

> Living systems tend to self-organize along a nonequilibrium Widom line, where proximity to critical optimality is dictated by the strength of the influence of their environments.

Our quasicriticality hypothesis involves a nonequilibrium Widom line of maximum (though finite) dynamical susceptibility along which the correlation length and, as demonstrated in Section 4.1.4, mutual information are expected to be maximal. Quasicritical dynamics are observed along this line: for instance, distributions of neuronal avalanches are nearly power-law and avalanche shape collapses can be approximately performed to yield approximate scaling exponents [71, 72]. This suggests that, while "critical optimality" is not accessible due to essential coupling to an environment, a relative optimality may be achieved along the nonequilibrium Widom line. Moreover, this nonequilibrium Widom line framework quantifies the notion of proximity to the unattainable nonequilibrium critical point and can perhaps be used to drive the system towards or away from its optimal behavior, by manipulating the relevant parameters.

4.1 The Strongly-Driven CBM

We now examine the CBM driven by the spontaneous activation of its nodes, which occurs with probability p_s for each node. Simulations presented in this chapter utilize Poisson-distributed spontaneous events to generate avalanches, to allow for close comparison to SOC (see Section 3.2). Because each node can now become spontaneously active with probability p_s, and can spread this activity to other nodes depending on their activity transmission probabilities P_{ij}'s, periods of inactivity ($\rho_1 = 0$) are punctuated by spontaneous periods of activity ($\rho_1 \neq 0$) which constitute avalanches. Whereas in the $p_s = 0$ case, the order parameter was the long-time density of active nodes, when $p_s \neq 0$, we cannot expect this to be the case. We will, however, still be interested in calculating the density of active nodes and will consider its time average:

$$\bar{\rho}_1 = \langle \rho_1(t) \rangle_t = \frac{1}{N_T} \sum_{t=1}^{N_T} \rho_1(t), \tag{4.1}$$

where N_T is the total number of simulated time steps. The behavior of the dynamical susceptibility χ will also be considered:

$$\chi = N[\langle \rho_1^2(t) \rangle_t - (\bar{\rho}_1)^2], \tag{4.2}$$

where the factor of N is included to ensure appropriate scaling in the $N \to \infty$ limit. I will now describe the mean-field approximation of the CBM with $p_s \neq 0$ to demonstrate that the critical transition occurs (in the thermodynamic limit) only when the external driving is absent.

4.1.1 Quasicriticality in the Mean-Field CBM

With a nonzero spontaneous activation probability, Equation 3.16 becomes

$$W(\mathbf{z}' \to 1) = 1 - (1 - p_s) \prod_{j=1}^{k_{in}} (1 - \kappa p_j \delta_{z_j,1}). \tag{4.3}$$

The $k_{in} = 1$ CBM map given in Equation 3.18 becomes

$$\begin{aligned} x_1(k+1) &= \left(1 - \sum_{z=1}^{\tau_r} x_z(k)\right) (\kappa(1-p_s)\, x_1(k) + p_s) \\ x_z(k+1) &= x_{z-1}(k), \text{ for } z = \{2, \cdots, \tau_r\}. \end{aligned} \tag{4.4}$$

This map produces no vanishing fixed points, but instead, a pair of real, non-zero fixed points given by

$$x_{1\pm}^* = \frac{\kappa(1-p_s) - (1+p_s\tau_r) \pm \sqrt{(\kappa(1-p_s) - (1+p_s\tau_r))^2 - 4\kappa p_s(1-p_s)\tau_r}}{2\kappa(1-p_s)\tau_r}.$$

In the case $k_{in} = 2$, the mean-field approximation produces the following cubic map:

$$\begin{aligned} x_1(k+1) &= \left(1 - \sum_{z=1}^{\tau_r} x_z(k)\right) \left(-a x_1^2(k) + b x_1(k) + p_s\right) \\ x_z(k+1) &= x_{z-1}(k), \text{ for } z = \{2, \cdots, \tau_r\}, \end{aligned} \tag{4.5}$$

where $a = \kappa^2 p_1 p_2 (1-p_s)$ and $b = \kappa(1-p_s)$. Again, no vanishing solutions.

4.1.2 The Nonequilibrium Widom Line

When $p_s \neq 0$ (and for small values of τ_r), x^*_{1-} is stable across $\kappa = 1$ and the dynamical susceptibility χ no longer diverges, i.e. the phase transition disappears, giving way to a crossover region (see Figure 4.1). To give an idea of the shape of χ, we have included light-blue bubbles with diameter logarithmically-scaled to its magnitude, and blue horizontal lines indicating its width at half-maximum which encompasses the *quasicritical* region. We have used the value $B = 0.5$ for presentation purposes, as it allows for a better view of the extent of the quasiperiodic phase boundary when κ is large; note that with $k_{in} = 2$, $\kappa_{max}(B = 1.4) \approx 1.247$ while $\kappa_{max}(B = 0.5) \approx 1.607$. Changes in B had no discernible impact on the phase diagram. For a fixed value of τ_r, we can identify the peak in the susceptibility (and correlation length), defining a nonequilibrium Widom line in the τ_r–κ plane; for the equivalent equilibrium Widom line see [73]. The nonequilibrium Widom line in the p_s–κ plane is presented in Figure 4.2.

4.1.3 Simulation of Avalanche Physics

We now go beyond the mean-field and present results from CBM simulations which demonstrate the presence of a nonequilibrium Widom line, a nonequilibrium phase diagram qualitatively similar to the mean-field nonequilibrium phase diagram, and a quasiperiodic phase. Because the mean-field approximation eliminates the fluctuations responsible for avalanches, it is not useful in analyzing the statistics of the avalanches associated with our model and so we also utilize results from our CBM simulations to study the avalanche physics and prepare avalanche size distributions. We re-emphasize the use of irreducible graphs in simulating the CBM.

We performed simulations using system sizes of 32, 64, 96, and 128 nodes, with spontaneous activation probabilities of 10^{-5}, 10^{-4}, and 10^{-3} at each value of $\kappa = [0.8, 1.3]$ with

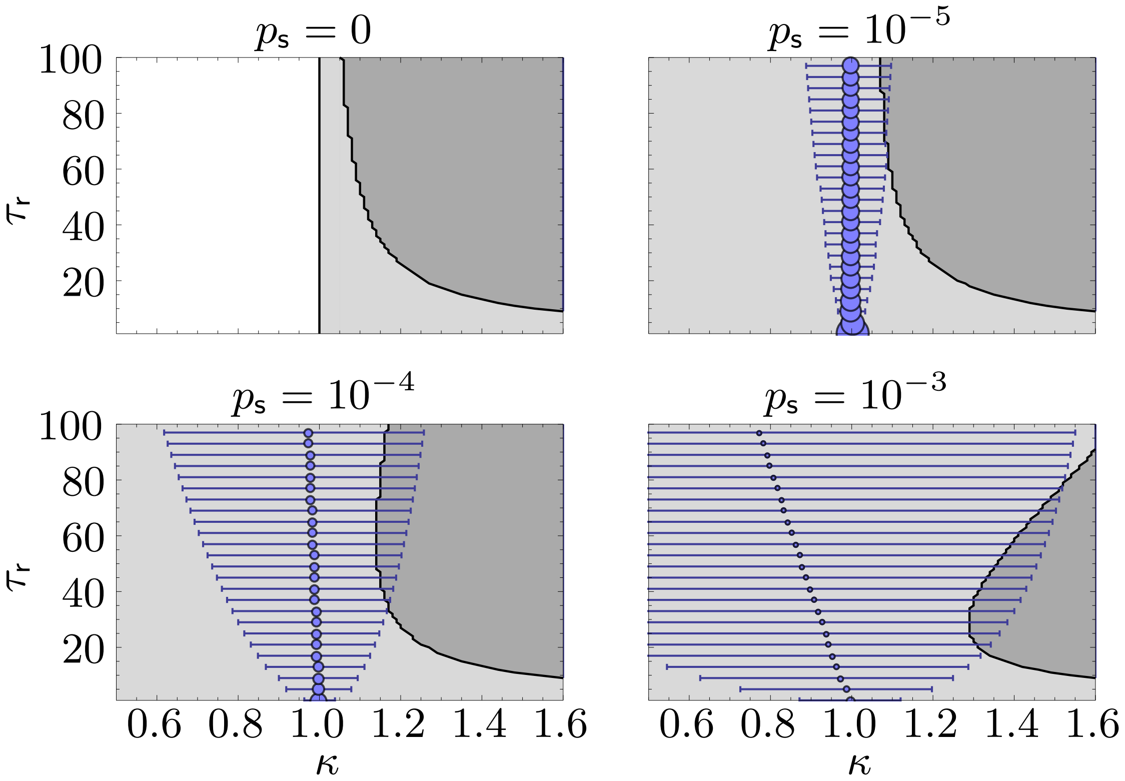

Figure 4.1: Nonequilibrium mean-field phase diagram for $k_{in} = 2$, at selected values of p_s. The light-gray region corresponds to the supercritical ordered phase with a nonzero stable fixed point and the dark-gray region corresponds to an oscillatory quasiperiodic phase, where all fixed points are unstable. Solid black lines are lines of non-analyticity and thus represent phase boundaries.

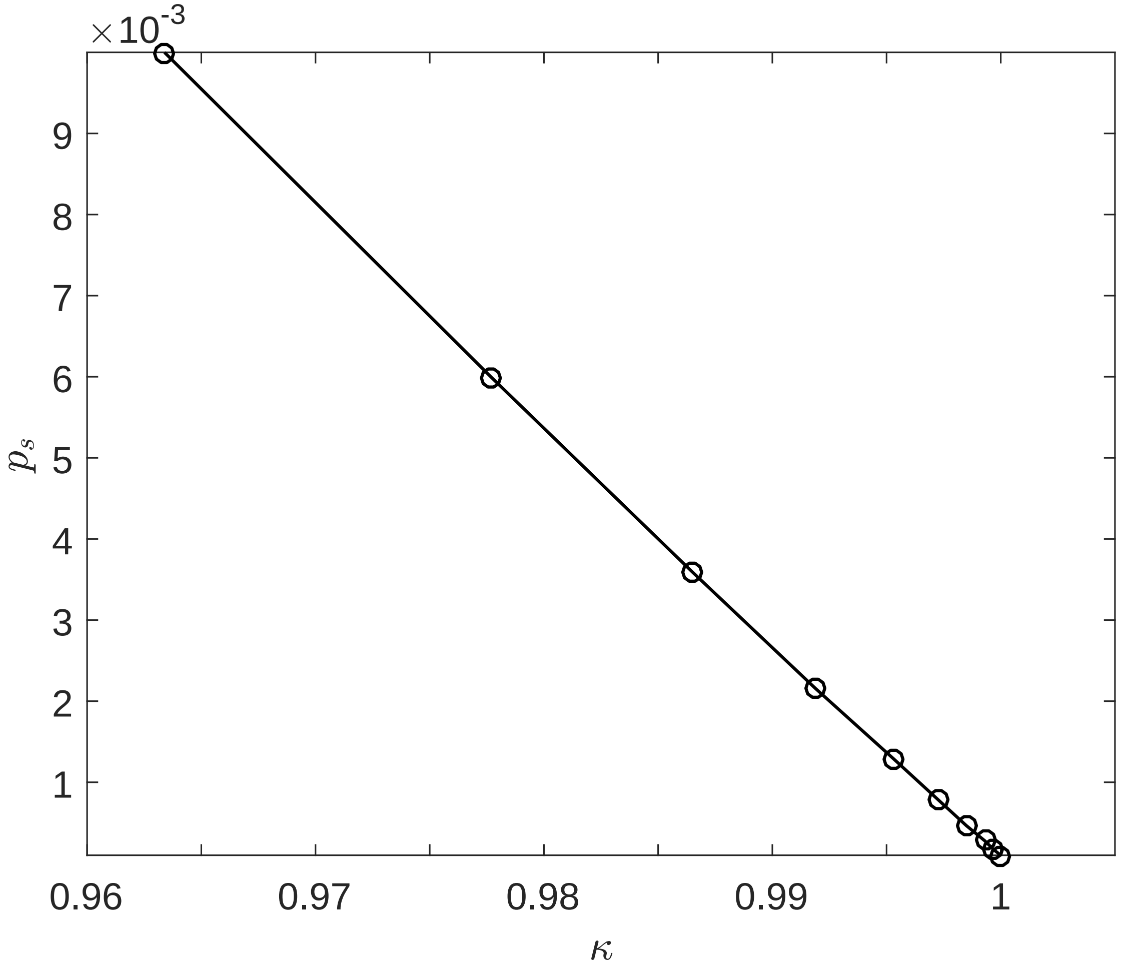

Figure 4.2: Nonequilibrium Widom line for the $k_{in} = 2$, $\tau_r = 1$ mean-field CBM evaluated over maximum number of 2000 iterations. The connection bias was $B = 1.4$.

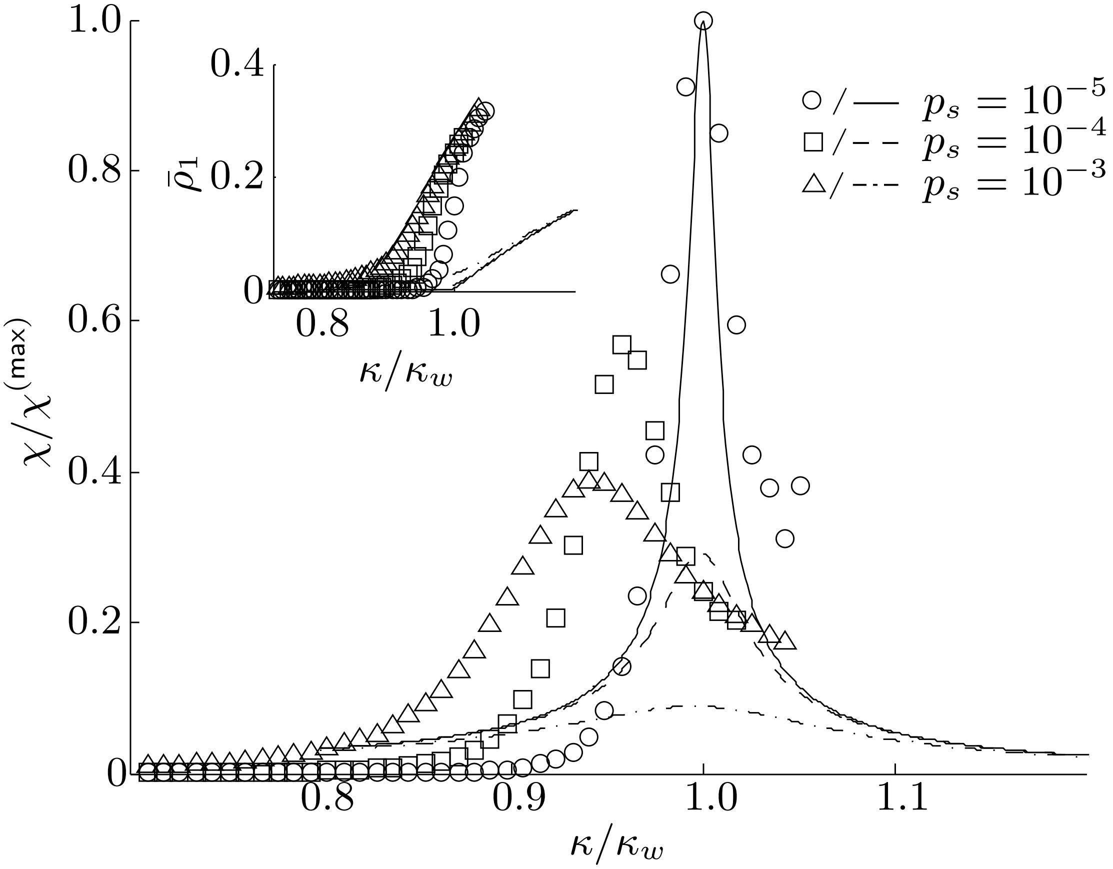

Figure 4.3: Dynamical susceptibility χ and $\bar{\rho}_1$ (inset) results from simulation with $N = 128$ (data markers) and mean-field approximation (lines). Results are normalized to their maximal values and plotted against κ normalized to the quasicritical point κ_w at $p_s = 10^{-5}$. For simulations, we find κ_w to be 1.10, 1.12, and 1.17 at $p_s = 10^{-3}$, 10^{-4}, and 10^{-5}, respectively. Curves of the dynamical susceptibility χ have been normalized to $\chi^{(\max)}$, the maximum dynamical susceptibility of the $p_s = 10^{-5}$ simulations. Similarly, values of the branching parameter, κ are normalized to the Widom line of the $p_s = 10^{-5}$ simulation, κ_w.

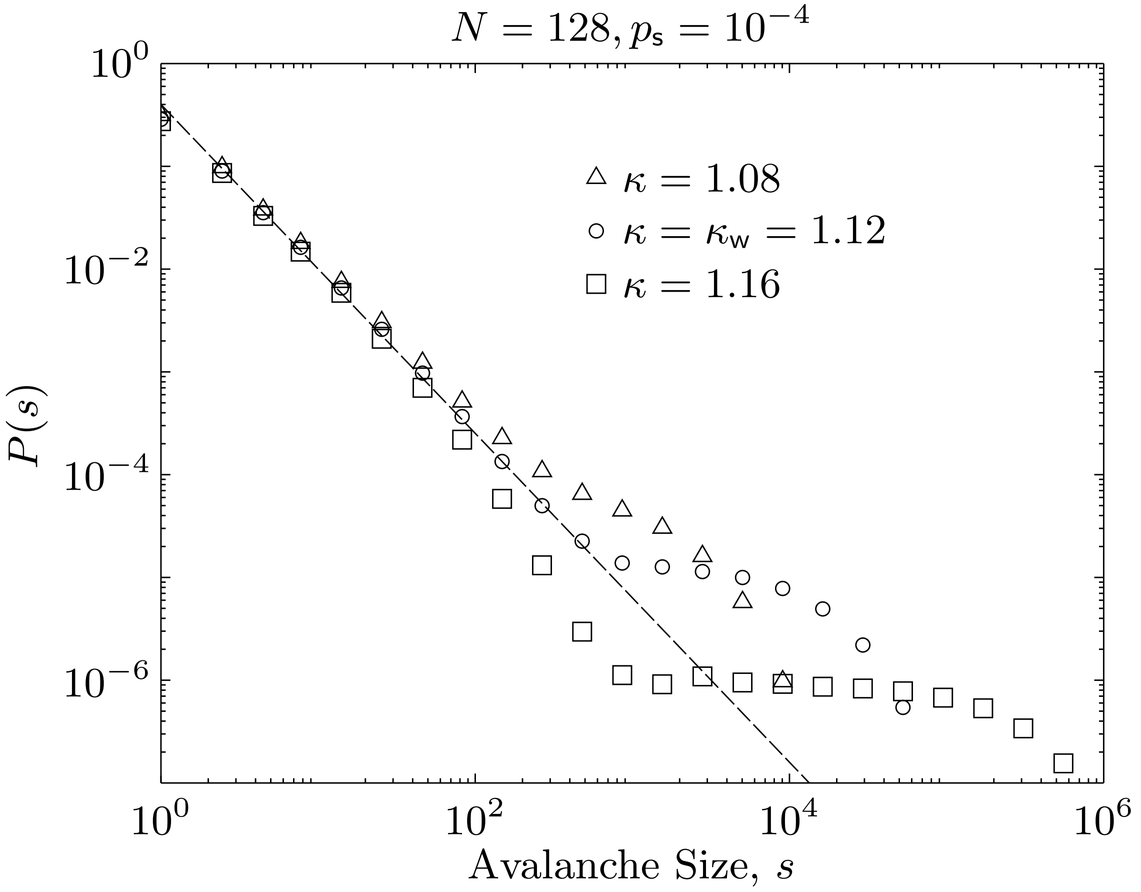

Figure 4.4: Logarithmically-binned avalanche size probability distributions $P(s)$ at various values of κ. The dashed line represents a power law with exponent $\tau = 1.6$.

a step size $\delta\kappa = 0.01$ and with $\tau_r = 1$. Simulations were performed on ten different random networks until 10^6 avalanches were generated at each value of κ; avalanche durations were limited to 10^5 time steps. Note that with $B = 1.4$ and $k_{in} = 3$, $\kappa_{max} \approx 1.307$. We determined the time-averaged density of active nodes $\bar{\rho}_1$ as well as the dynamical susceptibility χ, each as functions of κ for the various values of p_s for simulations and mean-field for comparison. The dynamical susceptibility peaks at quasicritical points κ_w defining a nonequilibrium Widom line in the p_s–κ plane (see Figure 4.3). Avalanche size distributions at these κ_w exhibit quasi-power-law behavior over a maximum number of decades (see Figure 4.4).

Much of the disagreement between the mean-field and simulation results is due to finite-size effects. If we were interested in the thermodynamic limit, however, we would need much larger system sizes which would require correspondingly large $k_{in} = \eta N$ for $0 < \eta \leq 1$ such that the simulated networks maintained irreducibility; this quickly becomes numerically-intensive and computationally-complex.

Quasiperiodicity Revisited

At values of τ_r and κ comparable to those at which the mean-field exhibits quasiperiodicity, an oscillatory synchronization phenomenon is observed in simulations (see Figure 4.5). At high κ and low τ_r, activity is nearly constant and very few avalanches are produced. As τ_r is increased, large populations of nodes activate and become refractory long enough for avalanches to be produced once again. Note that avalanches produced under these conditions are not scale-free, since the typical avalanche size approaches the system size. The quasiperiodic phase was found to diminish with increasing p_s, eventually disappearing at $p_s \approx 7 \times 10^{-3}$.

4.1.4 Optimal Information Transmission and the Widom Line

Mutual information has previously been used to measure information transmission in neural networks [74] and to demonstrate that information transmission is optimized at, or in the vicinity of phase transitions [14, 37, 75, 76]. To investigate this in the random networks of the CBM, we hence compute the mutual information $I_T(\mathsf{S};\mathsf{R})$ from an ensemble of stimulus patterns represented by the configuration of a subset of $N_\mathsf{S} < N$ nodes, $\mathcal{C}_\mathsf{S} = \{Z_\mathsf{S} = (z_{i_1}, z_{i_2}, \ldots, z_{i_{N_\mathsf{S}}}) | z_{i_k} \in S\}$ with $\dim \mathcal{C}_\mathsf{S} = (\tau_r + 1)^{N_\mathsf{S}}$, and an ensemble of corresponding response patterns represented by the configuration of a subset of $N_\mathsf{R} < N$ nodes, $\mathcal{C}_\mathsf{R} = \{Z_\mathsf{R} = (z_{j_1}, z_{j_2}, \ldots, z_{j_{N_\mathsf{R}}}) | z_{j_m} \in S\}$ with $\dim \mathcal{C}_\mathsf{R} = (\tau_r + 1)^{N_\mathsf{R}}$, where i_k and j_m belong to random, disjoint subsets (of dimensions N_S and N_R, respectively) of the set of all N nodes.

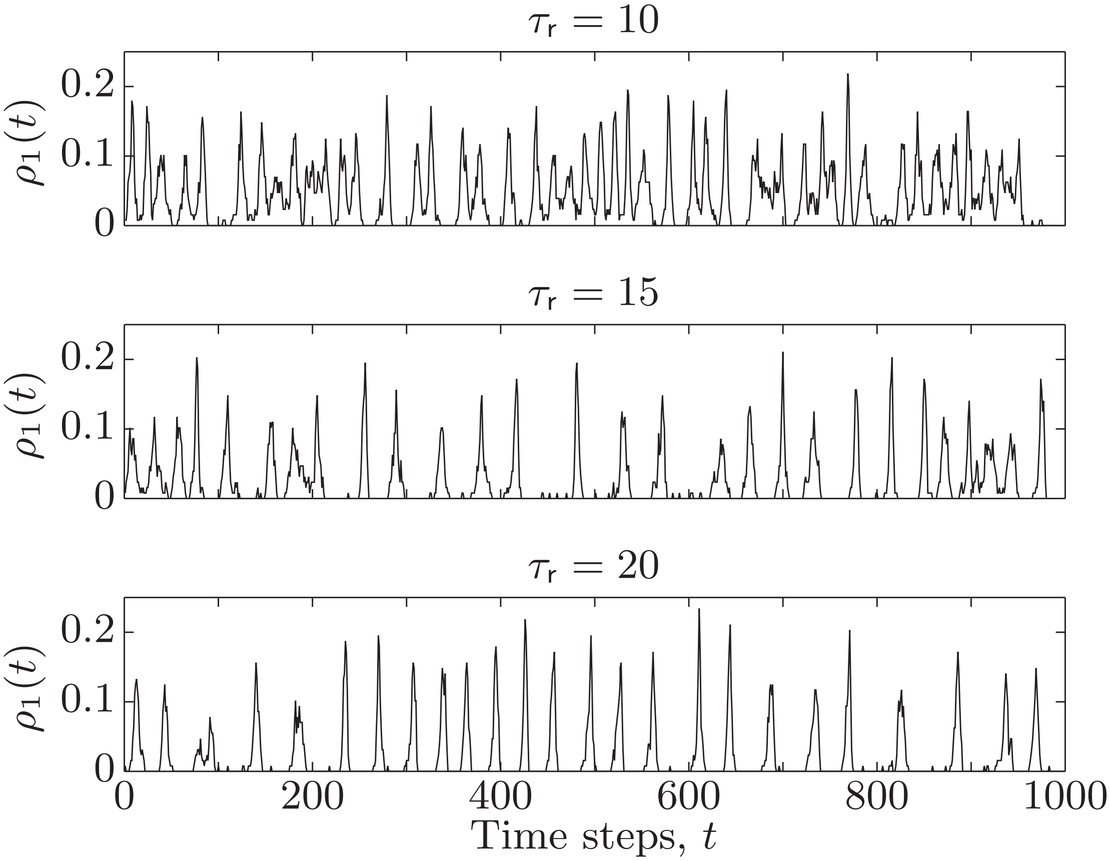

Figure 4.5: CBM simulation density of active nodes over 1000 time steps; $N = 128$, $k_{in} = 3$, $B = 0.5$, $\kappa = 1.60$, and $p_s = 10^{-3}$.

From [77], we have $I_T(\mathsf{S};\mathsf{R}) = H(\mathsf{R}) - H(\mathsf{R}|\mathsf{S})$, where

$$H(\mathsf{R}) = -\sum_{\mathcal{C}_\mathsf{R}} P(Z_\mathsf{R}) \log_2 P(Z_\mathsf{R}) \tag{4.6}$$

is the entropy (i.e., variability) of the responses with $P(Z_\mathsf{R}) = N_{Z_\mathsf{R}}/(\tau_r+1)^{N_\mathsf{R}} N_\mathsf{trials}$, and

$$H(\mathsf{R}|\mathsf{S}) = -\sum_{\mathcal{C}_\mathsf{R},\mathcal{C}_\mathsf{S}} P(Z_\mathsf{R}|Z_\mathsf{S}) \log_2 P(Z_\mathsf{R}|Z_\mathsf{S}) \tag{4.7}$$

is the entropy of the responses conditional on the stimuli with $P(Z_\mathsf{R}|Z_\mathsf{S}) = N_{Z_\mathsf{R}|Z_\mathsf{S}}/N_\mathsf{trials}$. In the equations above, N_{Z_R} corresponds to the number of times the configuration Z_R appears in the response and $N_{Z_\mathsf{R}|Z_\mathsf{S}}$ corresponds to the number of times the configuration Z_R appears in response only to the stimulus Z_S. The subscript T in the mutual information is an integer representing the number of time steps between the stimulus and the response.

We set $N_\mathsf{S} = N_\mathsf{R} = n$ and start a CBM simulation with an initial network configuration corresponding to an element of the stimulus configuration ensemble $\mathcal{C}_\mathsf{S}$; the resulting mutual information is computed using the configuration of the response nodes after some delay, i.e. some number of time steps T later. The average mutual information at a particular value of the branching ratio $I(\kappa)$ is determined after each element of the stimulus node configuration ensemble $\mathcal{C}_\mathsf{S}$ has been repeatedly applied N_trials times and averaged over the set of $T = \{T_\mathsf{min}, T_\mathsf{min} + \delta T, \ldots, T_\mathsf{max}\}$ delay times, i.e.

$$I(\kappa) = \frac{1}{N_\mathsf{delays}} \sum_{T=T_\mathsf{min}}^{T_\mathsf{max}} I_T(\mathsf{S};\mathsf{R}), \tag{4.8}$$

where $\delta T = T_\mathsf{min} + (T_\mathsf{max} - T_\mathsf{min})/(N_\mathsf{delays} - 1)$. Clearly, the task of computing $I(\kappa)$ quickly becomes numerically-intensive as n is increased. Using a system size of $N = 64$ and $N_\mathsf{trials} = 100$, we compute the mutual information for different sizes of input/output node sets $n = \{4, 6, 8\}$ averaged over the delays $T = \{60, ..., 120\}$ in steps of $\delta T = 10$ (so $T_\mathsf{min} = 60$, $T_\mathsf{max} = 120$, and $N_\mathsf{delays} = 7$) to demonstrate that the peak in $I(\kappa)$ converges towards the Widom line, i.e. the peak in the dynamical susceptibility at $\kappa_w \approx 1.22$, as n is increased (see

Figure 4.6). Peak locations for $I(\kappa)$ were determined by fitting to third-order polynomials and identifying κ values which corresponded to the maxima. As n approaches $N/2$ in the thermodynamic limit, we expect the $I(\kappa)$ and $\chi(\kappa)$ peaks to precisely overlap. We note that whereas mutual information has previously been shown to peak at the location of a phase transition in a variety of systems [75, 76], we argue based on our numerical evidence that generally the mutual information peaks along the nonequilibrium Widom line, thus supporting the quasicriticality hypothesis.

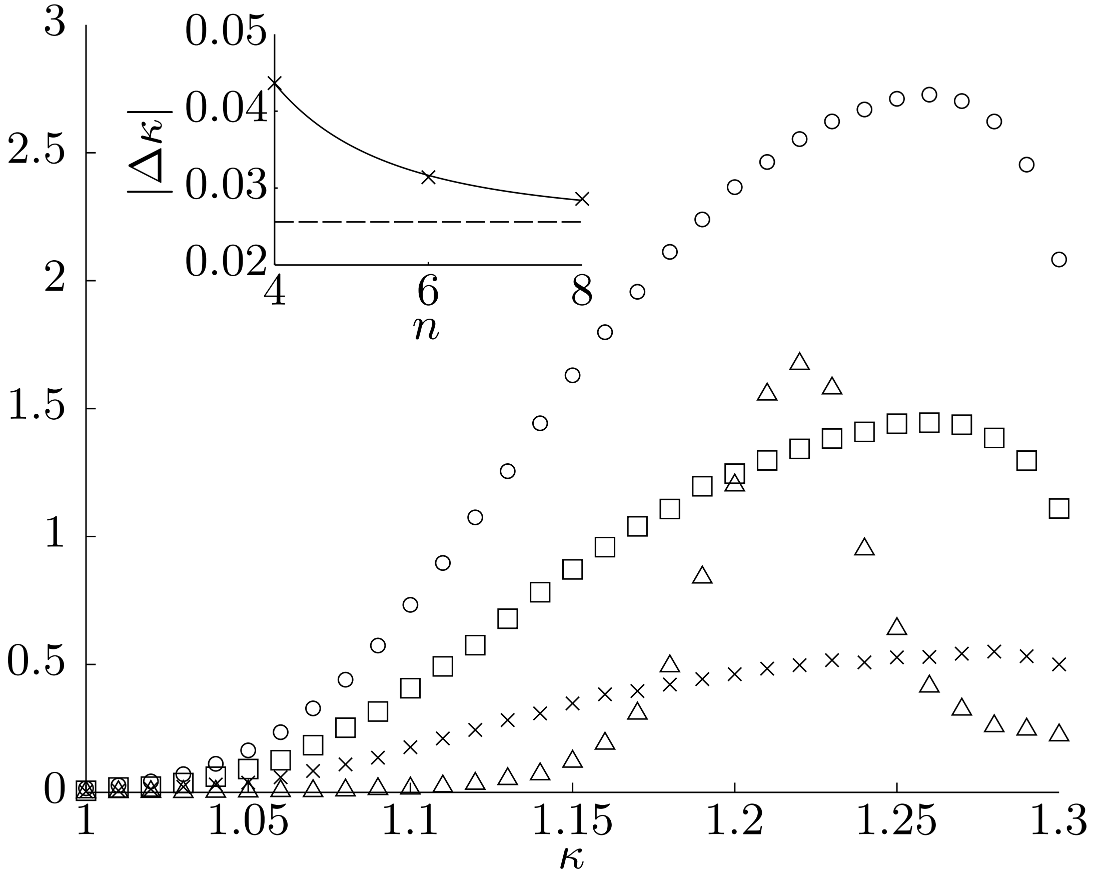

Figure 4.6: Dynamical susceptibility $\chi(\kappa)$ (triangles) and average mutual information $I(\kappa)$ (in bits). The mutual information is computed for values $n = \{4, 6, 8\}$, shown as crosses, squares, and circles, respectively (main figure). The discrepancy between the Widom line and average mutual information peaks, $|\Delta\kappa|$, is determined for each value of n (crosses) along with the line of best-fit (solid line: $|\Delta\kappa| = an^{-b} + c$) which approaches 0.026 (dashed line) as n is increased (inset).

CHAPTER 5

Causal Webs: Unveiling Dynamical Correlations

To test the quasicriticality hypothesis introduced in Chapter 4, we must have available experimental preparations in which the spontaneous activation probability and network strength of a living neural network can be precisely manipulated and observed. Such experiments are already being performed, for example, the *ex vivo* preparation used in [78]. Dynamical probes, such as the one presented in Appendix D, can be employed to examine the state of a living neural network and its closeness to criticality or the nonequilibrium Widom line in such an arrangement. Spontaneous activation rates, however, are not a part of the dominant paradigm for describing neural network dynamics. At present, "spontaneous activity" is taken to mean that activity of living tissue which has not been elicited by an explicitly applied stimulus, e.g., mechanical, electrical, or chemical stimulation. As used throughout this thesis, however, "spontaneous" suggests the absence of an observed *cause.* Hence, a method must be developed to infer the causal structure of neural network dynamics and separate spontaneous from driven events[1].

In this chapter, I introduce the notion of **causal webs** (or c-webs for short), a new emergent degree of freedom representing cascades of causally-related events, whose properties contrast and complement those of neuronal avalanches, which have been the standard for some time[2]. Whereas the latter are defined as spatiotemporal patterns of activation spanning a number of adjacent time steps framed by time steps lacking activity, c-webs explicitly depend on the network structure and temporal delays, thus accommodating the complex non-Markovian dynamics of living neural networks. Knowledge of the network structure and delay information is key, as it allows to distinguish between different spatiotemporal patterns of activation in a way which is not possible with avalanches (see Figure 5.1).

---

[1] I would be remiss if I failed to mention that the subject of causality is fraught with nuance and care must be taken to avoid making faulty conclusions—consider the old adage: "correlation does not imply causation". I hence suggest the reader to further explore the topic [79] and take the results presented here with the proverbial *grain of salt.*

Presented here is the so-called **deterministic causal webs** algorithm, which does not depend on connection strengths to establish a causal link between activations, i.e., a **causal pair** (MATLAB code is presented in Appendix A.2). An improved method, which has not been explored here, is the **stochastic causal webs** method, in which causal pairs are established stochastically, depending on the activity transmission probability between the two neurons.

5.1 Mathematical Formalism

The concept of c-webs is now formalized in the context of neural networks. Individual events are labeled $x = (i, t)$, representing the activation of neuron i at time t, or following the notation used in [19] and Section 3.2.2, $z_i(t) = 1$ ($z_i(t) = 0$ meant quiescence). We write the set of all events $A = \{x_\mu\}$, e.g., in Figure 5.1B, $A = \{a, b, c, d, e, f, g\}$. Formally, we define a c-web C as a set of correlated ordered pairs $(x_\nu^{(1)}, x_\nu^{(2)})$ of events (i.e., spikes), which we call **causal pairs**; quiescent neurons are not included in the set. The first and second entries, $x_\nu^{(1)}$ and $x_\nu^{(2)}$, of the νth causal pair represent causally-related presynaptic and postsynaptic events, respectively. (Despite causal relations being made in a pairwise fashion, we emphasize that this does not preclude multivariate interactions, as multiple

---

[2] A similar concept, known as causal polytrees, had previously been developed in a generic context along with an algorithm to recover causal structure from data [80].

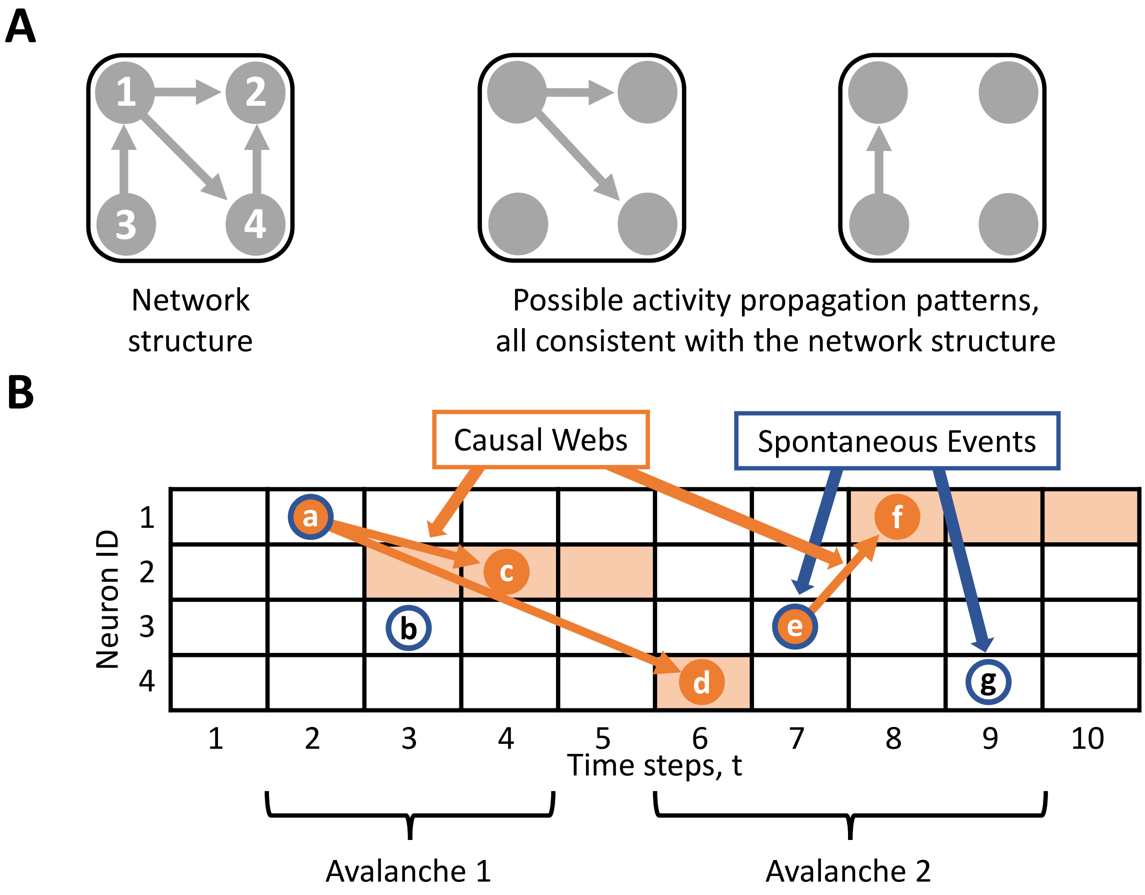
A
1
2
3
4
Network structure
Possible activity propagation patterns, all consistent with the network structure
B
Causal Webs
Spontaneous Events
Neuron ID
1
2
3
4
a
b
c
d
e
f
g
1
2
3
4
5
6
7
8
9
10
Time steps, t
Avalanche 1
Avalanche 2

Figure 5.1: Causal webs are distinct from neuronal avalanches in that they rely on network structure and synaptic delays. **A.** A network produces a variety of spatiotemporal activity patterns. **B.** Whereas only two neuronal avalanches are detected, a richer structure is revealed when spontaneous events (blue annuli) are separated from c-webs (orange disks); acceptance windows $W_{ij}(t)$ are shaded light-orange.

pairings can be made to a single event.) In the following, we show how to determine those causal pairs.

A complete set of causal pairs X is constructed by taking the Cartesian product of each event x_μ with its corresponding **dynamic postsynaptic events** $\mathcal{U}(x_\mu)$, i.e.,

$$X = \bigcup_{x_\mu \in A} x_\mu \times \mathcal{U}(x_\mu), \tag{5.1}$$

where $\mathcal{U}(x) \equiv \mathcal{U}(i,t)$ is the set given by

$$\mathcal{U}(i,t) = \{(j,t') \mid j \in N(i) \text{ and } t' \in W_{ij}(t)\}. \tag{5.2}$$

$N(i)$ refers to the set of all postsynaptic neurons j of neuron i, and $W_{ij}(t) = [t + d_{ij} - \Delta_{ij}, t + d_{ij} + \Delta_{ij}]$ is a predetermined dynamical **acceptance window**: if a postsynaptic neuron j is active within the acceptance window, then a causal link is inferred. The lower bound of the acceptance window is adjusted such that it is greater than t. We write the set of events in X as $A(X) \subseteq A$.

Synaptic delays d_{ij} associated with the connection from a presynaptic neuron i to a postsynaptic neuron j, are allowed to have some uncertainty Δ_{ij} due to variability in the postsynaptic spike timing. Later, in Section 5.3, I present a method by which this information can be determined from data; for the moment, we assume it is given. In Figure 5.1B, synaptic delays and their uncertainties are given for the connections in Figure 5.1A: $d_{12} = 2$, $d_{14} = 4$, $d_{31} = 2$, and $d_{42} = 1$, with $\Delta_{12} = 1$, $\Delta_{14} = 0$, $\Delta_{31} = 1$, and $\Delta_{42} = 1$. This information can be used to determine causal pairs, e.g., the event $a = (1,2)$ in Figure 5.1B has $\mathcal{U}(a) = \{c, d\}$, resulting in the causal pairs $a \times \mathcal{U}(a) = \{(a,c), (a,d)\}$. The complete set of causal pairs for the **spacetime graph** in Figure 5.1B is $X = \{(a,c), (a,d), (e,f)\}$ and so $A(X) = \{a, c, d, e, f\}$.

A causal web represents the connected components of a directed graph whose vertices and edges are $A(X)$ and X, respectively. The example in Figure 5.1B thus has two c-webs,

$C_1 = \{(a,c),(a,d)\}$ and $C_2 = \{(e,f)\}$. Note that spontaneous events initiate c-webs and may become part of ongoing c-webs. The **size** $s(C)$ of a c-web is defined as the total number of distinct events within it. Defining that set as $A(C)$, the size $s(C)$ is then given by its cardinality: $s(C) = |A(C)|$. Note that $A(C) \subseteq A(X)$. For example, $A(C_1) = \{a,c,d\}$ and $A(C_2) = \{e,f\}$ in Figure 5.1B, with $s(C_1) = 3$ and $s(C_2) = 2$, respectively.

The **duration** $D(C)$ of a c-web C can be defined in terms of its **chord**. The chord of a c-web $K(C)$ is the sequence of distinct time steps for which there are events belonging to that c-web, arranged in ascending order in time, with no repeated elements. That is, $K(C) = (t_1, t_2, ..., t_n)$, where t_1 and t_n are the times of the first and last events, respectively. In contrast to the definition of duration for avalanches, the length of a c-web's chord is not equal to the c-web duration. Instead, we define the duration of a c-web as a measure of its chord plus one, i.e., $D(C) = 1 + \lambda(K(C))$, where $\lambda(K(C)) = t_n - t_1$. The chords of the c-webs in Figure 5.1B, for example, are $K(C_1) = (2,4,6)$ and $K(C_2) = (7,8)$, with durations $D(C_1) = 5$ and $D(C_2) = 2$.

Finally, we define the **branching fraction** $\phi(C)$ of a c-web C as the average number of postsynaptic events associated with each presynaptic event, i.e., it is the average number of descendants, as given in Section 3.2.4:

$$\phi(C) = \frac{1}{s(C)} \sum_{\mu=1}^{|A(C)|} \sum_{\nu=1}^{|C|} \delta_{x_\mu(C), x_\nu^{(1)}(C)}, \tag{5.3}$$

where δ is the Kronecker delta. The first sum is evaluated over all events $x_\mu(C)$ of c-web C, while the second one is over all presynaptic events $x_\nu^{(1)}(C)$, given by $\beta(C) = \{x_\nu^{(1)}(C)\}$. For example, in Figure 5.1B, $\beta(C_1) = \{a\}$ and $\beta(C_2) = \{e\}$, with $\phi(C_1) = 2/3$ and $\phi(C_2) = 1/2$.

5.2 Tests of the Method

We performed tests of our method using simulations of the cortical branching model (CBM) [19]. Neuronal avalanches and c-webs should coincide as emergent cascades of correlated events in the limits $p_s \to 0$ and $d_{ij} = 1$ for all pairs of nodes (i, j). We simulated 10^6 avalanches on a network of $N = 243$ nodes, whose structure and synaptic weights were inspired by experimental data; all synaptic delays were set to a single time step. To simulate the $p_s \to 0$ limit (a separation of timescales), we initiated avalanches at single, random nodes, only starting a new avalanche when the previous one had finished; no spontaneous events or concurrent avalanches were allowed. The resulting avalanche and c-web size probability distributions were identical, as expected.

In another test, we constructed a random, reducible network of $N = 360$ nodes, each with an in-degree of $k_{in} = 3$, with a Perron-Frobenius eigenvalue of $\kappa = 0.23$, as in [19] and Section 4.1. Synaptic delays (in time steps) were drawn from a uniform distribution of integers in a closed interval, $d_{ij} \in [1, 16]$. Spontaneous activation probabilities for each node were drawn from a Gaussian distribution with mean and standard deviation of 10^{-4}; negative values were set to zero. The simulation was performed over 3.6×10^6 time steps. Spontaneous events detected by our method were used to construct a new spontaneous activation probability distribution, which we compared with the initial distribution using a Kolmogorov-Smirnov test: the distributions were in agreement at a 5% significance level with a p-value of 0.9955 [81]. We note that as the overall connectivity of the network (which we quantify by κ, as in [19]) is increased, spontaneous events become less prominent as c-webs begin to dominate the dynamics, leading to more driven activations and refractory nodes, thus preventing spontaneous events: neural network dynamics present a fluctuating bottleneck to the influence of an environment.

5.3 Determining the Network Structure: Transfer Entropy

We have hitherto assumed knowledge of the network structure and delay information, i.e., the d_{ij} and Δ_{ij}'s, however in practice, this information must be learned from experimental data. I describe in this section a method, based on delayed transfer entropy (dTE) [82, 83], by which this information can be established from high temporal resolution multiunit timeseries data. The use of dTE is not absolutely necessary; alternatives, such as computing conditional probabilities directly from data, may be applied so long as they provide a network structure and synaptic delays.

Transfer entropy (TE) is a non-parametric, asymmetric, information theoretic statistic of the information transfer between two random processes; in this context, the two processes correspond to the timeseries, $z_i(t)$ and $z_j(t)$, corresponding to the activity of two neurons i and j. Conceptually, TE is the information (measured in bits) gained by considering the past activity of $z_i(t)$, thus improving the prediction of $z_j(t)$ (see Figure 5.2).

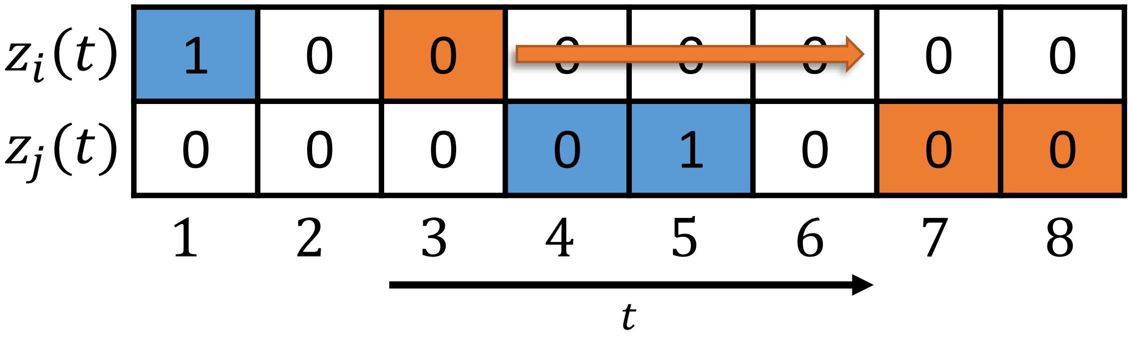

Figure 5.2: Transfer entropy is a measure of the information gained in predicting the future activity of one random process by considering the past activity of another. In delayed transfer entropy, a window (shaded boxes) encompassing $z_i(t-d)$, $z_j(t-1)$, and $z_j(t)$, is moved through the evolution of two random processes to determine the value of $T_{i\to j}(d)$.

In 2011, Ito et al. presented a generalization of TE, dTE, which accounted for activity transmission delays [82]. The transfer entropy $T_{i\to j}(d)$ is calculated for a particular pair of neurons (i,j) at a specific activity transmission delay d. If there is a connection from presynaptic neuron i to postsynaptic neuron j, then the dTE is expected to peak at a delay value $d = d_{ij}$ which corresponds to the activity transmission delay from neuron i to neuron

j—for example, in Figure 5.2, the dTE might peak at $d_{ij} = 4$. The width, Δ_{ij}, of the curve $T_{i\to j}(d)$ is used as a measure of the uncertainty in d_{ij} [82]. The dTE is defined as follows:

$$T_{i\to j}(d) = \sum_{\mathbf{z}_{i\to j}(d)} p(z_j(t-1), z_j(t), z_i(t-d)) \log_2 \left(\frac{p(z_j(t)|z_j(t-1), z_i(t-d))}{p(z_j(t)|z_j(t-1))} \right), \tag{5.4}$$

where $\mathbf{z}_{i\to j}(d) = \{z_j(t-1), z_j(t), z_i(t-d)\}$ indicates that the sum is performed over all possible configurations of the variables $z_j(t-1)$, $z_j(t)$, and $z_i(t-d)$. Considering only binary variables, i.e., the case $\tau_r = 1$, this amounts to a sum over eight configurations $\mathbf{z}_{i\to j}(d)$, each occurring with frequencies quantified by the probabilities $p(z_j(t-1), z_j(t), z_i(t-d))$. To measure these probabilities, we can pass a window through the time-evolutions of two processes, recording the frequency with which each configuration appears (see Figure 5.2). The $t = 5$ window is shown as blue shaded boxes and the $t = 8$ window corresponds to the orange boxes, both at $d = 4$. In practice, however, we would prefer a more efficient algorithm in which all joint probabilities are computed except for $p(0, 0, 0)$, which can be determined by subtracting 1 from the sum of the others. This would likely involve two subroutines, one which finds all configurations $\{z_j(t-1), z_j(t), 1\}$ followed by another for configurations $\{z_j(t-1), z_j(t), 0\}$, which uses information from the first subroutine to minimize the work of the second. Conditional probabilities in Equation 5.4 are also estimated from timeseries data [82].

Elimination of Spurious Connections

As in [84], we eliminated spurious connections using delay information produced by dTE. We account for two specific kinds of spurious connections, **common drive** and **transitive**, which confound our TE analysis (see Figure 5.3). The common drive effect occurs when two neurons, B and C, share a common presynaptic neuron A: if neuron A fires, both B and C are expected to fire at later times depending on their respective synaptic delays. In this situation, dTE may detect a spurious connection between neuron B and C as shown in Figure 5.3A. The transitive effect occurs when a neuron A connects to neuron C, which then connects to neuron B; dTE may detect a spurious connection from A to B with a delay equal to the sum of the synaptic delays from A to C and C to B (see Figure 5.3B). These connections can be removed by locating such neuronal trios and eliminating spurious connections based on delay information.

Mean-Field Approximation: Converting $T_{i\to j}$ to P_{ij}

Because the CBM is based on stochastic activity propagation, we must convert TE values to activity transmission probabilities to maintain compatibility with our stochastic view of neural network dynamics. A mean-field approximation is utilized to make this conversion and is described in the supplemental materials of [71]. Recalling the mean-field treatment of Section 4.1.1, consider the probability $p_1^{(j)}(t)$ for the postsynaptic neuron j to be active (i.e., in state $z = 1$) at timestep t:

$$\begin{aligned} p_1^{(j)}(t) &= p_0^{(j)}(t-1)(p_s^{(j)} + P_{ij}p_1^{(i)}(t-d)) + p_1^{(j)}(t-1)(p_s^{(j)} + P_{ij}p_1^{(i)}(t-d)) \\ &= p_s^{(j)} + P_{ij}p_1^{(i)}(t-d), \end{aligned} \tag{5.5}$$

where $p_0^{(j)}(t-1)$ is the probability that neuron j is quiescent at timestep $t-1$, $p_s^{(j)}$ is the spontaneous activation probability of neuron j, P_{ij} is the activity transmission probability from neuron i to j, and $p_1^{(i)}(t-d)$ is the probability that neuron i is active at timestep $t-d$. Note that despite the cellular automata rules we have defined for our models, the data may show two adjacent activations of a single neuron from time to time, and so we have accounted for this possibility here. For an examination of a similar delayed CBM mean-field approximation, refer to Appendix E.1. The probability of observing each configuration $\{z_j(t-1), z_j(t), z_i(t-d)\}$ can then be determined by evaluating $p(z_j(t-1), z_j(t), z_i(t-d)) = p^{(j)}_{z_j(t-1)}(t-1)p^{(j)}_{z_j(t)}(t)p^{(i)}_{z_i(t-d)}(t-d)$, e.g., for the configuration $\{0, 1, 0\}$, we have $p(0, 1, 0) = (1-p_s^{(j)})p_1^{(j)}(t)(1-p_1^{(i)}(t-d))$. As a consequence of the approximation given in Equation 5.5,

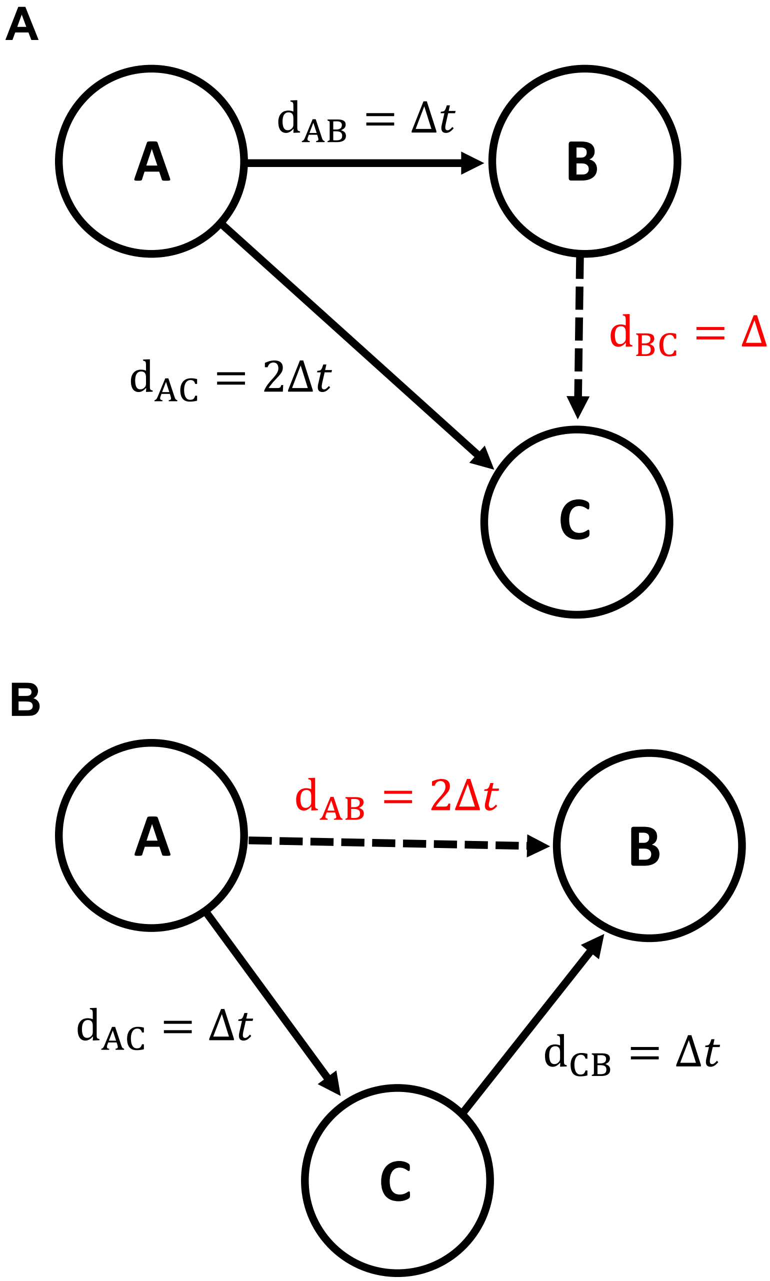
A
A
B
C
$d_{AB} = \Delta t$
$d_{BC} = \Delta t$
$d_{AC} = 2\Delta t$
B
A
B
C
$d_{AB} = 2\Delta t$
$d_{AC} = \Delta t$
$d_{CB} = \Delta t$

Figure 5.3: Spurious connections, of common drive (A) and transitive (B) types, confound TE analysis, but can be removed using synaptic delay information.

the function $T_{i\to j}(d)$ (cf. Equation 5.4), is proportional to P_{ij}, and hence we can estimate P_{ij} using the delayed TE calculated from experimental data.

5.4 Application to Experimental Data

We next demonstrate the utility of our method when applied to experimental data (see Figure 5.4). For our demonstration, we have used ten data sets from [85], which were collected *in vitro* from organotypic cultures of mouse somatosensory cortex using a 512-microelectrode array with a 60 μm electrode spacing and a 20 kHz sampling rate over an hour-long recording [86, 87]. Data were spike-sorted to identify individual neurons then down-sampled to 1 kHz; spurious connections have been removed, as in [84]. Using our method, spontaneous events (dark blue) were disentangled from c-webs (orange) to illustrate their qualitative differences. In Figure 5.4A, we present an activity time raster (top panel) and corresponding timeseries of the activity (bottom panel), on which we have performed a moving average with a $\Delta t = 100$ ms window: $y(t) = \sum_{t'=0}^{\Delta t-1} x(t-t')/\Delta t$, where $x(t) = \sum_{i=1}^{N} \delta_{z_i(t),1}$ [88]. In Figure 5.4B, we plot logarithmically-binned avalanche and c-web size probability distributions to demonstrate that while neuronal avalanches may exhibit approximate power-law scaling, thus suggesting underlying critical behavior, the use of c-webs reveals potentially quasicritical, non-power-law behavior, as predicted in [19]. Although we have not determined whether the network operates at or near the nonequilibrium Widom line ($\kappa_w = 1.12$ at $p_s = 10^{-4}$ for the simulated network), the qualitative shape of the c-web size distribution agrees with $d_{ij} = 1$ simulations of the CBM performed (Figure 5.4B inset), indicating that the activity in Figure 5.4B is potentially not critical. Six of the ten data sets examined displayed similar behavior.

To demonstrate that this result is not anecdotal, and to further illustrate this discrepancy between c-webs and avalanches in real data, I have plotted both the c-web and

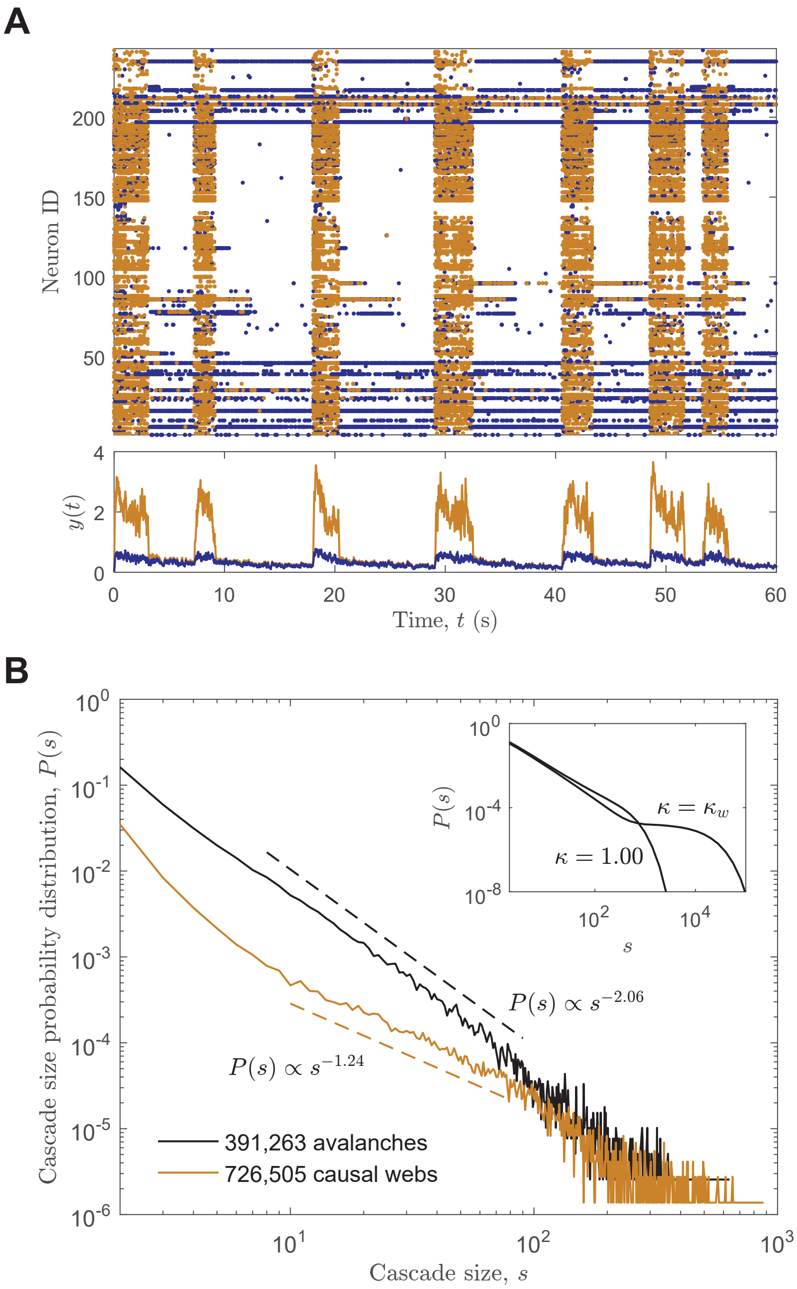

Figure 5.4: Application of the c-web method on experimental data. **A.** Time raster of one minute of neural network activity recorded from somatosensory cortex, processed to separate spontaneous events (dark blue) from c-webs (orange). Note that tonically-active neurons mainly produce spontaneous events. **B.** Avalanches binned at 1 ms (black) and c-webs (orange) exhibit different statistical properties and scaling; experimental data qualitatively agrees with simulations from [19] (inset).

avalanche size and duration probability distributions using aggregated somatosensory cortex data in Figure 5.5. Event size probability distributions (Figure 5.5A) show a clear discrepancy between c-webs and avalanches for all but the largest events; event duration distributions (Figure 5.5B) show a clear discrepancy for shorter events. The size distributions appear to be most sensitive to the presence of spontaneous activations, whereas the duration distributions appear to be most sensitive to the presence of synaptic delays. Avalanche durations from experimental data followed approximate power laws with exponents in a range of $[1.83, 3.38]$ and a median of 2.35; c-web duration distributions only marginally exhibited power-law behavior.

Distributions of c-web branching fractions determined for the aggregated data were found to follow an approximate power law with exponent -3.56 ± 0.19 (see Figure 5.6A), while neuronal avalanche branching ratios (as determined using Equation 3.11) for the same data were roughly Gaussian-distributed about a mean of 0.82 ± 0.19 with a standard deviation of 0.38 ± 0.20 (see Figure 5.6B). The avalanche branching ratio distribution, being roughly distributed close to a branching ratio σ close to 1, had lent credibility to the criticality hypothesis, which relied on self-organized critical models with critical points at $\sigma = 1$. But as demonstrated in this chapter, neuronal avalanches potentially conflate unrelated activity, and therefore this result may be misleading. The c-web branching fraction distribution, on the other hand, seems to be strongly influenced by the out-degree distribution (see Figure F.2 in Appendix F), and thus more closely reflects the features of the network structure and dynamics. One would expect the average number of descendant activations (i.e., the c-web branching fraction) to be dominated, at least to some degree, by the network structure and this is what I have demonstrated here.

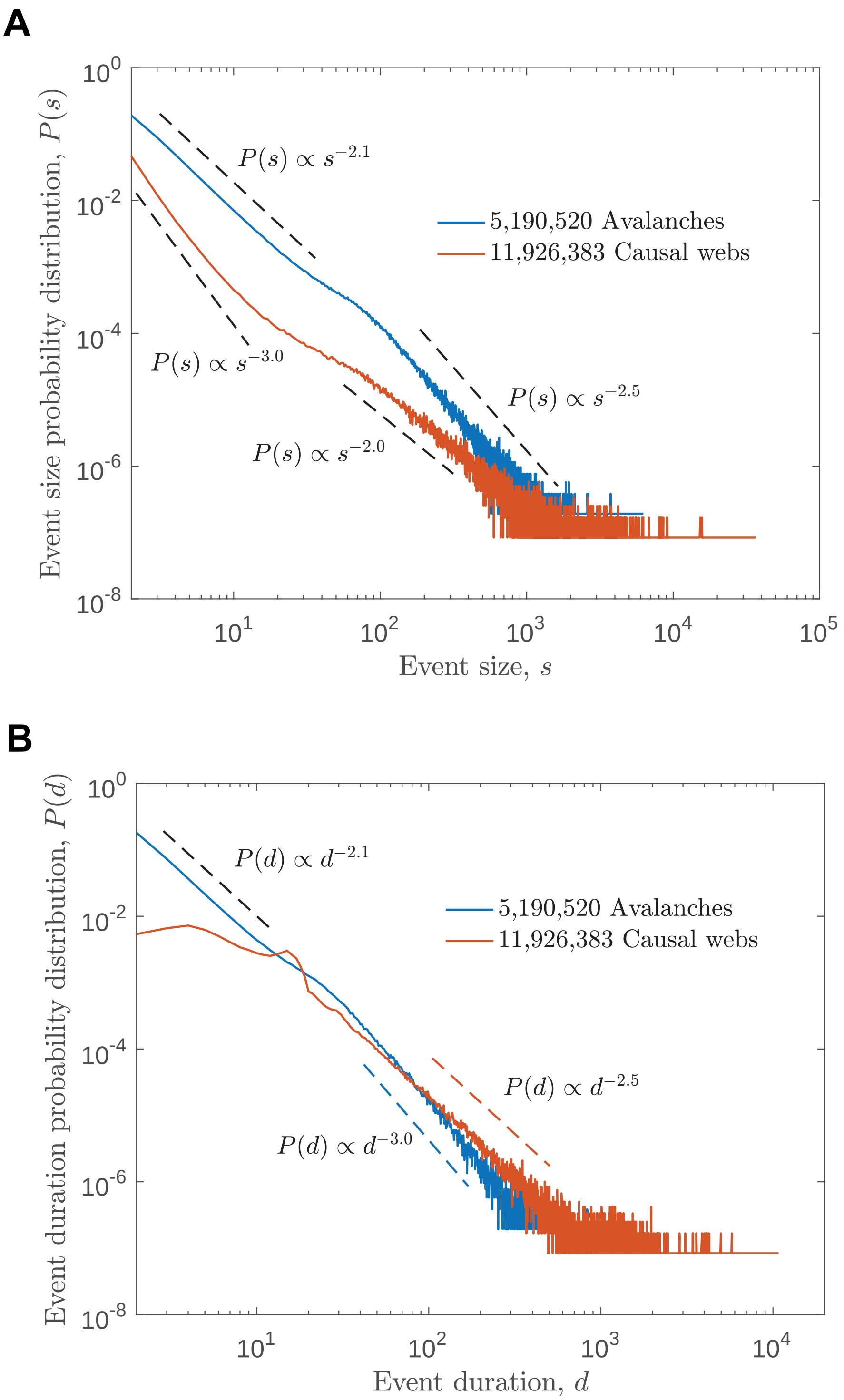

Figure 5.5: Avalanche and c-web size (A) and duration distributions (B) from aggregated mouse somatosensory cortex data.

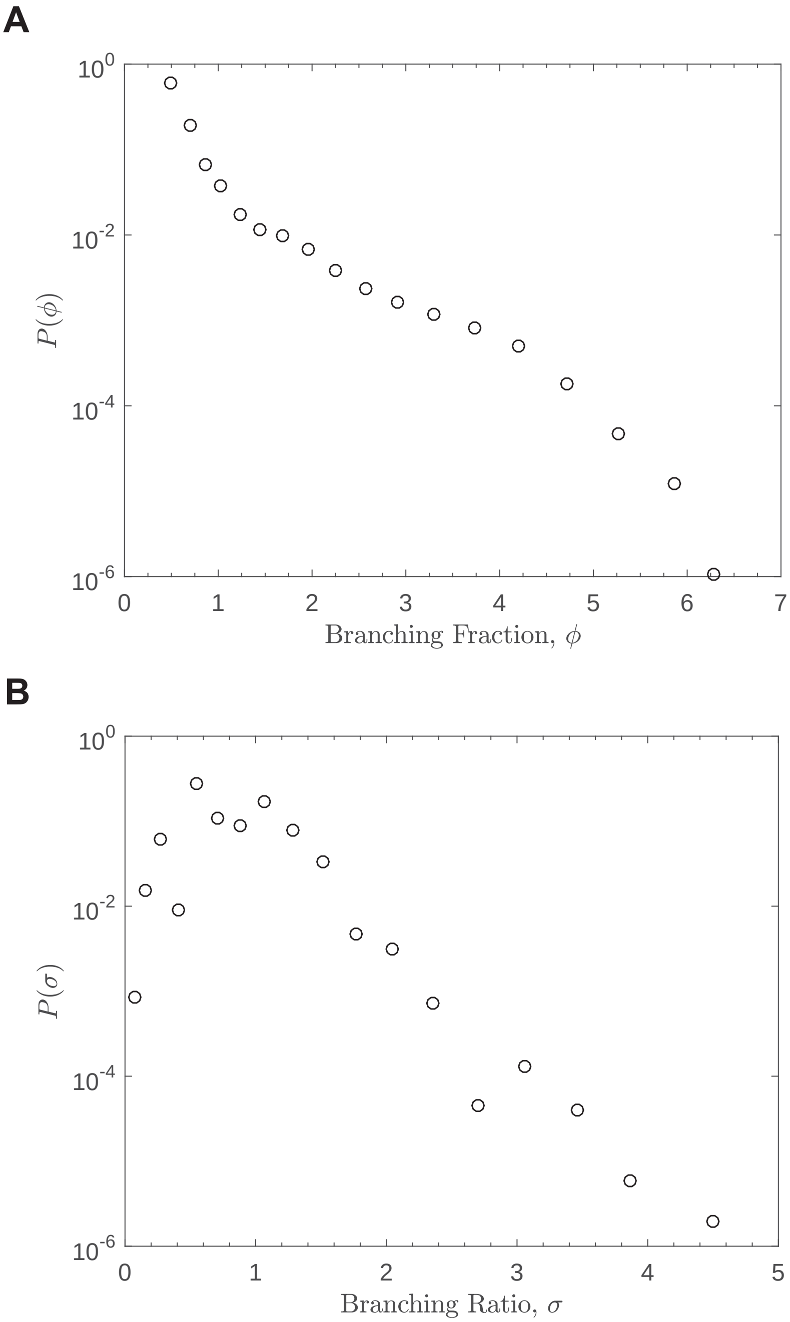

Figure 5.6: Probability distributions of c-web branching fractions (A) and avalanche branching ratios (B) from aggregated somatosensory cortex data show very different behavior.

5.5 Graphical Representations of Causal Webs

Because c-webs can be represented as directed graphs with vertices and edges given by $A(X)$ and X, respectively, it may be desirable to visualize these graphs. Causal webs will generally be **directed acyclic graphs** (DAGs), meaning that a number of **topological ordering** algorithms may be employed to produce a visual representation in linear time [89, 90]. DAGs are best suited to layered graph drawing styles, a.k.a. Sugiyama-style drawings, which place nodes in horizontal layers with vertices directed downward. Some algorithms for producing Sugiyama-style drawings include Kahn's algorithm, depth-first search algorithms, and Coffman-Graham algorithms, which minimize edge crossings. Generally, such algorithms constitute injective (i.e., one-to-one), measure-preserving maps of neuron positions and their activation times, the most trivial and easily understood of which is essentially a time raster with directed edges indicating causal relations, as in Figure 5.7. More complex algorithms[3] might be surjective (i.e., onto), non-measure-preserving maps, which are not as easily understood, but which may produce a more aesthetically pleasing visual representation (see Figure 5.8). In either case, nodes represent individual neuronal activations and directed edges represent causal relations between activations.

---

[3] Such as MATLAB's `digraph` function, which I have used here.

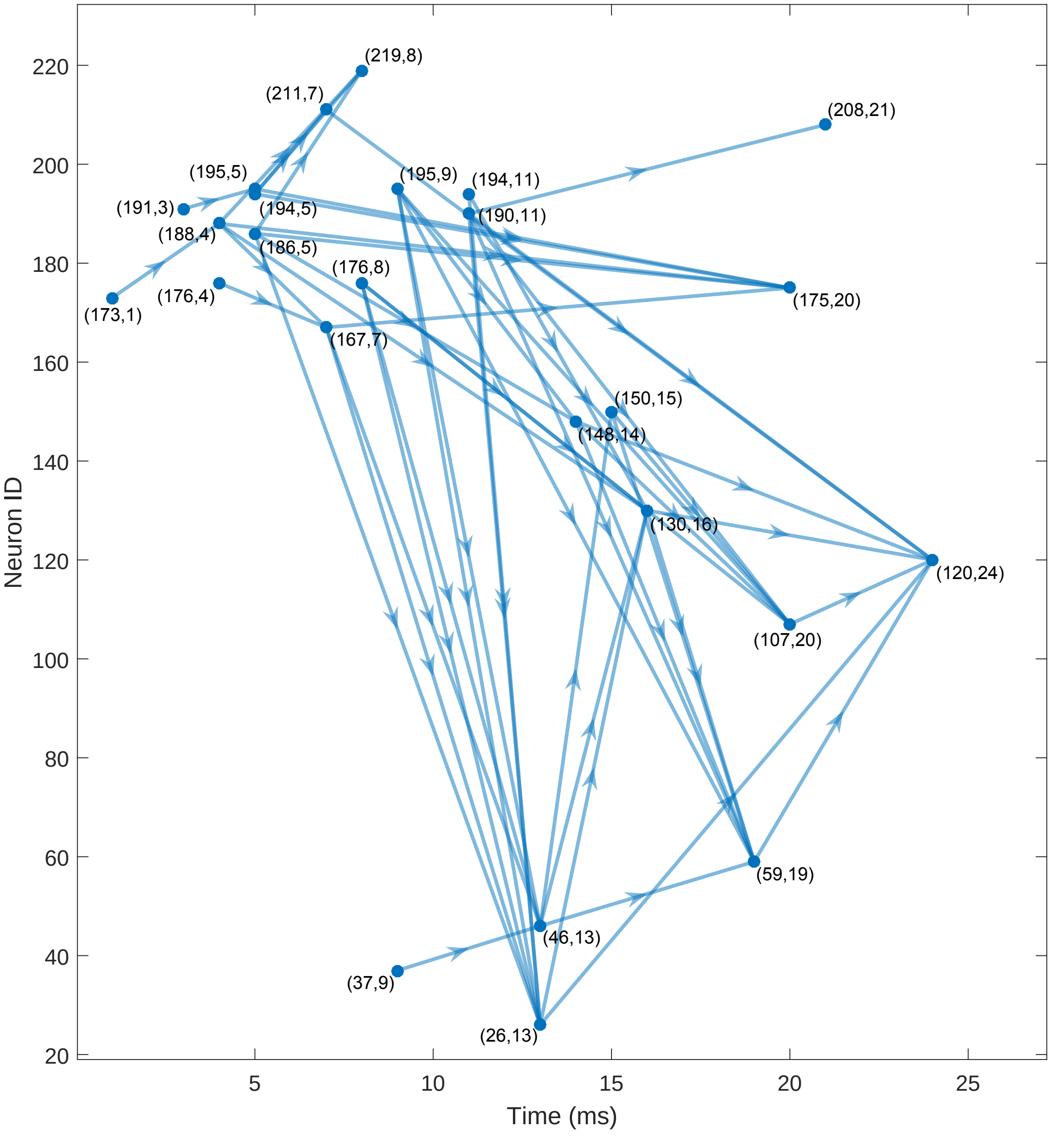

Figure 5.7: A causal web in raster form shows inferred causal relations between individual neuronal activations. Labels indicate neuron ID and relative activation time in milliseconds.

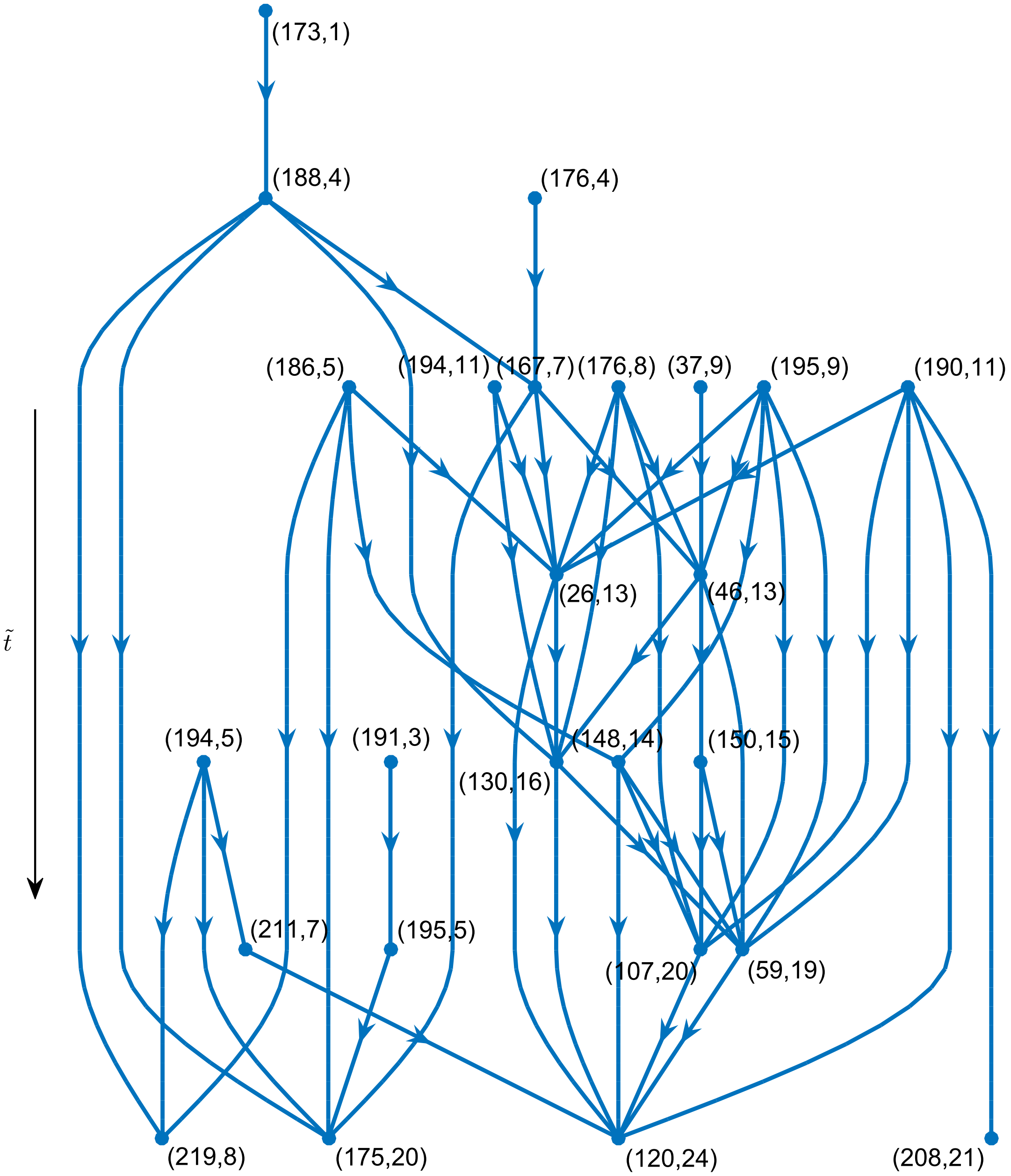
(173,1)
(188,4)
(176,4)
(186,5)
(194,11)
(167,7)
(176,8)
(37,9)
(195,9)
(190,11)
$\tilde{t}$
(26,13)
(46,13)
(194,5)
(191,3)
(148,14)
(150,15)
(130,16)
(211,7)
(195,5)
(107,20)
(59,19)
(219,8)
(175,20)
(120,24)
(208,21)

Figure 5.8: A causal web in an abstract activation space. Labels indicate neuron ID and relative activation time in milliseconds. The arrow of time points downward, but this axis is the result of a surjective, non-measure-preserving mapping of the time axis.

CHAPTER 6

Conclusions and Outlook

In this thesis, I explored complex dynamics of open neural networks and their associated nonequilibrium phase transitions. I have reviewed the theory of equilibrium and nonequilibrium phase transitions and self-organized criticality, then presented my work on quasicriticality and causal webs. In closing, I summarize my findings, place them within a larger context, describe their implications, and present potential future research directions. My central contributions are:

- Introduction of the nonequilibrium Widom line framework [19].
- Development of the quasicriticality hypothesis [19].
- Introduction of causal webs [58].

6.1 The Quasicriticality Hypothesis

The introduction of the **quasicriticality hypothesis** and the **nonequilibrium Widom line framework** has some serious implications for ongoing investigations of critical phenomena in biological systems, and contributes to a longstanding debate on self-organized criticality (SOC). My work suggests that such systems cannot be critical due to their *essential* coupling to an environment. Despite this, biological systems may still operate along a nonequilibrium Widom line of relative optimality, where their closeness to the critical point is determined by the strength of the influence of the environment.

A key concept in the quasicriticality hypothesis is the nonequilibrium Widom line, a line of maximal dynamical susceptibility, which naturally leads to a set of specific questions which can be addressed in living neural networks. For example: How does the nonequilibrium Widom line depend on the spontaneous activation probability p_s, the branching parameter κ, and the refractory period τ_r? By what factor is the maximum susceptibility modified by changes in p_s? Most importantly, what mechanisms drive living neural networks towards the nonequilibrium Widom line? All of these questions are experimentally accessible because manipulations of these parameters are readily made possible with the perfusion of pharmacological agents, adjustments of ionic concentrations [37, 91], or background stimulation [92, 93, 94] applied to *in vitro* preparations of neural networks. Note that in adjusting these parameters, we are manipulating intrinsic timescales of the system. There are a number of ways living neural networks could adjust these timescales, e.g., as a result of widespread neuronal activation or synchronization or by changing the balance of excitation and inhibition.

In developing these concepts, I have made extensive use of the cortical branching model (CBM), for which I developed a mean-field approximation and calculated its nonequilibrium phase diagram, finding three nonequilibrium phases: an absorbing disordered phase, an active ordered phase, and an oscillatory quasiperiodic phase. The CBM features four timescales, three of which I manipulated here: (1) the driving timescale associated with the spontaneous activation probability p_s, (2) the relaxation timescale associated with the branching parameter κ, (3) the refractory timescale associated with the refractory period τ_r, and (4) the activity transmission timescale, i.e. the time a signal is in transit from its originating node to its destination node (described in Appendix E). The situation where the driving and relaxation timescales are fully separated, i.e., when $p_s = 0$, and where the activity transmission delays are a single timestep, corresponds to SOC.

This novel framework may serve to explain existing experimental results. For instance, although there have been numerous reports of power laws resulting from spiking activity *in vitro* [71, 95, 96], they are rarely found *in vivo* [97, 98]. In the context of what is presented here, *in vitro* preparations could have a much smaller external influence p_s than *in vivo* preparations, which would suggest that they operate closer to criticality. And although the influence of different spontaneous activation probability distributions (e.g. Poisson, geometric, naturalistic) on the phase diagram or on details of the Widom line is not explored here, it could be probed experimentally to answer questions relating to the effect of external stimuli on the brain. Isolated neural networks used for *in vitro* preparations typically show intervals of many seconds between network bursts that initiate neuronal avalanches, while the avalanches themselves last tens to hundreds of milliseconds [99]. This separation of timescales, which is often given as a requirement for SOC [51], is not clearly seen with *in vivo* preparations, where each neural network receives many synaptic inputs from other intact brain regions.

6.1.1 The Quasiperiodic Phase

In addition to the critical phase transition found to occur when $p_s = 0$, a Neimark-Sacker bifurcation was found to give rise to an oscillatory **quasiperiodic phase** when τ_r was increased (see Appendix B). This transition could be the result of a competition of timescales. The significance of the quasiperiodic phase in terms of the behavior of living neural networks has not been fully explored, but it may represent epileptiform activity. Previous studies have found neuronal refractory periods to increase as a result of the axonal demyelination associated with multiple sclerosis [100, 101, 102]—a disease which is correlated with an unexplained increased incidence of epileptic seizures [103]. Perfusion of glutamate receptor agonists (such as kainic acid, KA) has been found to decrease neuronal refractory periods, while glutamate receptor antagonists (such as 6-cyano-7-nitroquinoxaline-2,3-dione, CNQX) were found to increase them [104]. Paradoxically, both KA and CNQX have been used to induce *in vitro* seizure-like activity [105, 106]. So while the oscillations observed in simulations are possibly related to the pathological synchronization typically associated with epilepsy, we note that synchronization in epilepsy is complex and not yet fully understood [107].

Technically, one of the key features of this quasiperiodic phase is that, unlike typical limit cycles in discrete systems, the system never revisits points in a quasiperiodic oscillation and hence the periodicity of the oscillations is not well-defined. In fact, I have found that the first Lyapunov exponent was positive and yet the limit cycle was stable; the system exhibits a sort of "contained chaos", in which the trajectory visits all points within a restricted region, without repetition, and while maintaining an oscillatory envelope. I make several attempts at understanding this behavior in Appendix B.

6.2 Generalized CBMs

As presented here, the CBM lacks some key features of living neural networks which may have a significant influence on the model behavior. Two glaring omissions are (1) the lack of a dynamic network structure, realized in a living neural network with regulatory mechanisms and synaptic plasticity, and (2) different neuron types, primarily inhibitory neurons. In living neural networks, the network structure derives from a combination of neuronal dynamics and external influences, such as sensory stimuli, which may drive a network towards optimality. I now describe the possible consequences for these omissions and future developments.

6.2.1 Network Structure

The influence and importance of the network topology has not been fully explored here. I have only used irreducible, random directed graphs with fixed in-degrees, partly to facilitate the development of the mean-field approximation. It would be interesting to explore other network topologies, including reducible and non-planar directed graphs, and additionally study numerically and, if possible, develop additional mean-field approximations. In the spirit of using realistic network topologies, I have developed an as yet untested method to construct such biologically-inspired networks, presented in Appendix G. This phenomenological network model is based on transfer entropy analysis of neural networks, and so it produces mean-field, time-averaged approximations of living neural network topologies at best—these networks are thus not expected to produce the self-organizing system we are looking for.

To address self-organization, it will be necessary to have a model which can self-tune via biological regulatory mechanisms, e.g., synaptic plasticity and neuronal homeostasis. The goal would be for such a model to respond in real time to its own dynamics and the influence of an environment by undergoing flows in parameter space (see Figure 6.1). This situation corresponds to dynamical disorder in the network structure, as opposed to quenched disorder, and presents a model which gives opportunities to understand how living neural networks deviate from optimal behavior due to some pathology. For example, an epileptic neural network may be suddenly drawn away from quasicriticality along the nonequilibrium Widom line and towards an attractor within the oscillatory quasiperiodic phase, thus initiating a seizure. Self-organizing network models which implement Hebbian learning rules, have been found to self-organize to a critical state [108] and recently, much more realistic "bottom-up" models have become available, e.g., self-organized recurrent networks (SORNs) [109] and self-organized cortical models (SOCMs) [110]. These realistic models, however, often suffer from being too detailed to provide analytically-tractable results and thus attempts at characterization of their exhibited phases and transitions are hindered. Simpler "top-down" models which yield analytical results will be key in making substantial progress.

6.2.2 Neuronal Heterogeneity

Due in part to the aforementioned regulatory mechanisms, living neural networks feature a high-degree of heterogeneity, which is also not explored here. Some spatial heterogeneity has been implemented into the CBM in the form of disordered connection strengths, but the model has no explicit temporal heterogeneity aside from perhaps the spontaneous events in the $p_s \neq 0$ case; the branching parameters and refractory periods are homogeneous throughout the network. Regulatory mechanisms cause these features to change in response to the recent history of the system, e.g., following a burst of activity, neurons may be less likely to fire and spread activity, a result of metabolic restrictions within each cell; this situation could be modeled with a disordered, time-dependent branching parameter for each node, which will depend on that node's recent history. Moreover, different neuron types have not been fully explored and this sort of heterogeneity may lead to new physics. A generalized CBM with inhibitory nodes is briefly considered in Appendix E.

The improved understanding of the heterogeneity of noise in neural networks, made possible by the introduction of causal webs, may allow for theoretical advancements to be made. For example, as in the case of an Ising spin system with a dichotomous external magnetic field, additional phases or different critical behavior, such as tricritical points may appear [16]. Heterogeneity may even have the potential to save the criticality hypothesis if it can be shown that living neural networks feature extended critical regions, such as Griffiths phases, which can arise due to spatial and/or temporal heterogeneity [111, 112].

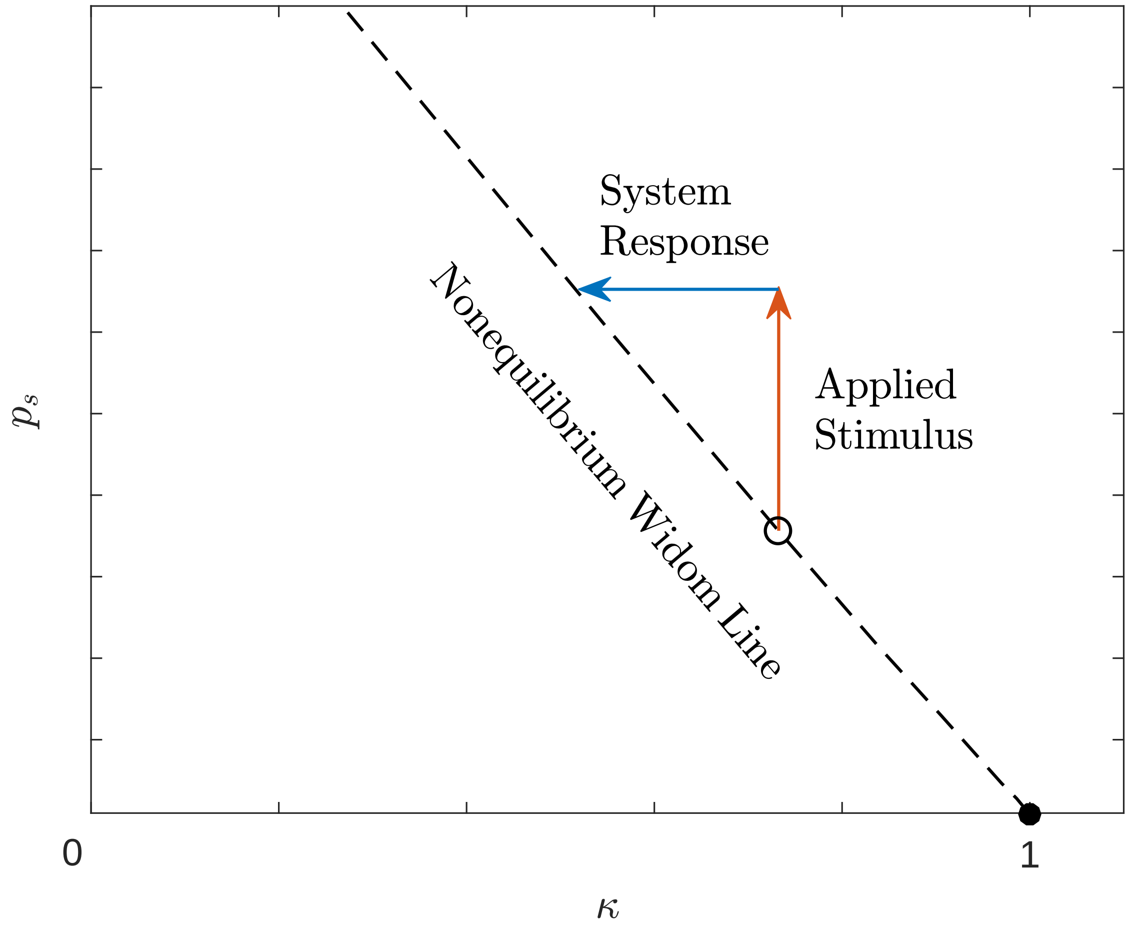

System
Response
Applied
Stimulus
Nonequilibrium Widom Line
p_s
0
1
κ

Figure 6.1: Self-organization to the nonequilibrium Widom line. A system, initially in a quasicritical state (black ring), is exposed to a chronic stimulus after which it adapts, transiting back to the nonequilibrium Widom line after sufficient time.

These Griffiths phases make it possible to optimize biological computation in a broad range of parameter values, thus obviating the need for fine-tuning, while potentially allowing for critical phenomena to coexist with environmental influences.

The influence of inhibitory neurons has also not been explored in the CBM, although a generalization of the CBM which includes the effect of inhibition is briefly developed in Appendix E. This improvement could help understand how this form of regulation dynamically alters disorder in a complex system, and what consequences this has for their behavior and computational optimality. One possibility is that inhibition acts as a sort of fluctuating bottleneck to the inputs of an environment, not only restraining the response of the network, but also perhaps adjusting the amount of inherent disorder and optimality [113]. Although it is hypothesized that living neural networks employ regulatory mechanisms (e.g., inhibition, spike-timing-dependent plasticity, refractory periods, and homeostatic adaptation) to achieve optimization—be it at a critical point or along a Widom line—the disorder itself may facilitate optimization in other ways such as in the case of Griffiths phases.

6.3 Beyond the Mean Field

Because the dynamical mean-field approximation excludes finite-sized fluctuations, i.e., avalanches, we must go beyond the mean field if we hope to analytically examine avalanche physics and obtain exact avalanche exponents. In statistical physics, the canonical next step involves applying the Bethe-Peierls approximation–in an artificial intelligence context, this method has been rediscovered as belief propagation (BP). The mean-field approximation explored in Section 3.3 considers a single node for which we determine the probability to find it in any of the allowed states $z \in \mathcal{S} = \{0, 1, 2, ..., \tau_r\}$; in the Bethe-Peierls approximation, we consider a single node and its nearest neighbors, computing the probabilities (i.e., "marginals" in BP) for each to be in any of the allowed states. This can be accomplished by summing over all the possible $|\mathcal{S}|^{1+k_{in}+k_{out}}$ configurations, but this quickly becomes computationally intensive; an alternative algorithm may be desired and this is provided by BP, a message-passing algorithm. For tree-like graphs, BP can compute marginals in $\mathcal{O}(1 + k_{in} + k_{out})$ time; a generalization of BP to graphs with loops is known as the cavity method [16, 114]. It is key to note, however, that approaches such as BP must be further developed to work on directed networks with non-Markov dynamics, such as in the case of a neural network with activity transmission delays and refractory periods.

6.4 Impact and Potential Applications of Causal Webs

The **causal webs** algorithm introduced in Chapter 5 uses knowledge of the network structure and activity transmission delays to separate causally-related neuronal activations, called causal webs (c-webs), from those which are not, i.e., spontaneous activations [58]. The structure of c-webs is primarily governed by the network topology and dynamics, whereas spontaneous events are potentially caused by an external stimulus or the intrinsic properties of the neurons themselves. This methodology represents a novel approach for analyzing complex networks in a range of fields and with significant consequences in neuroscience.

Whereas neuronal avalanches had been defined as bursts of activity in adjacent timesteps, framed by timesteps lacking activity, c-webs depend explicitly on the causal structure of the activity. The definition of neuronal avalanches overlooks two key features of living neural networks. First, neural networks are extended open systems with spontaneously active elements meaning that, as defined, neuronal avalanches may conflate unrelated activity from various sources and across a neural network. Secondly, because neural networks involve disordered synaptic delays, neuronal activity in two adjacent time steps may not be causally-related; a choice of one bin width may be appropriate for some pairs of neurons, but not for others. By unveiling the causal structure of neural network activity, c-webs obviate the need to choose the “correct” temporal binning—which can drastically affect neuronal avalanche statistics [14, 96, 115]—providing a more detailed picture of the underlying dynamics, and hence calling for a renewed analysis of existing data and application of the c-webs method to new experimental data.

The ability to disentangle c-webs from spontaneous events (i.e., noise) allows us to better test the quasicriticality hypothesis, as well as admitting new ways to examine the role of noise and heterogeneity in neural network dynamics. We are now able to examine the nature of spontaneous events in living neural networks, for example, tonically-active cells might be identified from their high spontaneous activation probability. This sort of information could be used to improve simulations by incorporating the spontaneous events directly from data. Another application is the identification of different classes of neurons. For instance, because inhibitory neurons exhibit different firing patterns from excitatory neurons, namely fast-spiking and tonic activation [116, 117], and because we have found tonic activations to be mostly spontaneous (cf. Figure 5.4A), distributions of spontaneous neuronal events may help identify inhibitory neurons, complementing previously-established methods [118]. Additionally, an improved characterization of noise in the nervous system may contribute to our understanding of neurological disorders, for example, it has been suggested that a reduced signal-to-noise ratio produces inefficient hyperactivation in the prefrontal cortices of schizophrenics during successful cognitive tasks [119]. This hypothesis has been supported by computational models showing that neural network attractors become unstable with increased noise [120]. Thus c-webs could be used to examine the neural basis of hyperfrontality for the first time. Causal webs may also provide further insight into the nature of rapid eye movement sleep, recently been shown to be induced by the activation of inhibitory neurons [121]. The latter may lead to a decreased signal-to-noise ratio, as in the portions of Figure 5.4A dominated by spontaneous events. Our method may also inform understanding of the neural network structure beyond the capabilities of currently available methods. In the case of network undersampling, hidden network cycles might be discovered by employing our approach in conjunction with population coupling methods [122]. Moreover, c-webs enable us to better distinguish recurrent from feed-forward neural network dynamics, which may be important in developing improved mean-field approximations.

Causal webs not only represent a novel method in neuroscience, but a fundamentally new way of understanding the behavior of complex networks in general, with applicability to a variety of topics in physics, chemistry, biology, ecology, geology, economics, and sociology, which merit further investigation. For example, financial networks could be decomposed into agents that directly interact through exchanges as well as exogenous factors like weather or inflation and the c-webs method could be used to understand the causal links between these influences and quantities of interest. In models of disease spreading, such as the SIRS model, c-webs could potentially differentiate between different sources of infection [123]. Such an approach is likely to be useful whenever considering interacting units, whether they are people in social networks, species in ecological webs, or protein molecules in a stochastic environment. A specific application in social media could involve the detection of Twitterbots and astroturfing [124].

APPENDIX A

Simulation and C-Web Algorithm Codes

Using spike-sorted MEA data in conjunction with delayed transfer entropy analysis and the deterministic causal webs algorithm, we are able to improve model simulations. This is accomplished by feeding synaptic weights, delays, and spontaneous events from c-webs analysis into a simulation, as depicted in Figure A.1.

A.1 MATLAB Cortical Branching Model Code

```
% cxmodel5.m
% gCBM with disordered parameters and activity transmission delays.
% INPUTS
% weightmat: NxN weighted adjacency matrix--elements are probabilities
% NT: maximum number of timesteps, typically 3.6E6, integer
% Taurs: Nx1 vector of refractory periods, integers
% spontEvents: Nx1 cell of vectors containing spontaneous activation times
% sig_del: NxN synaptic delays matrix, integers
% delSDs: NxN matrix of delay ranges, i.e., standard deviations, integers
%        (zeros mean synaptic delay is known with absolute certainty).
% OUTPUTS
% asdf: simulation asdf file
%
```

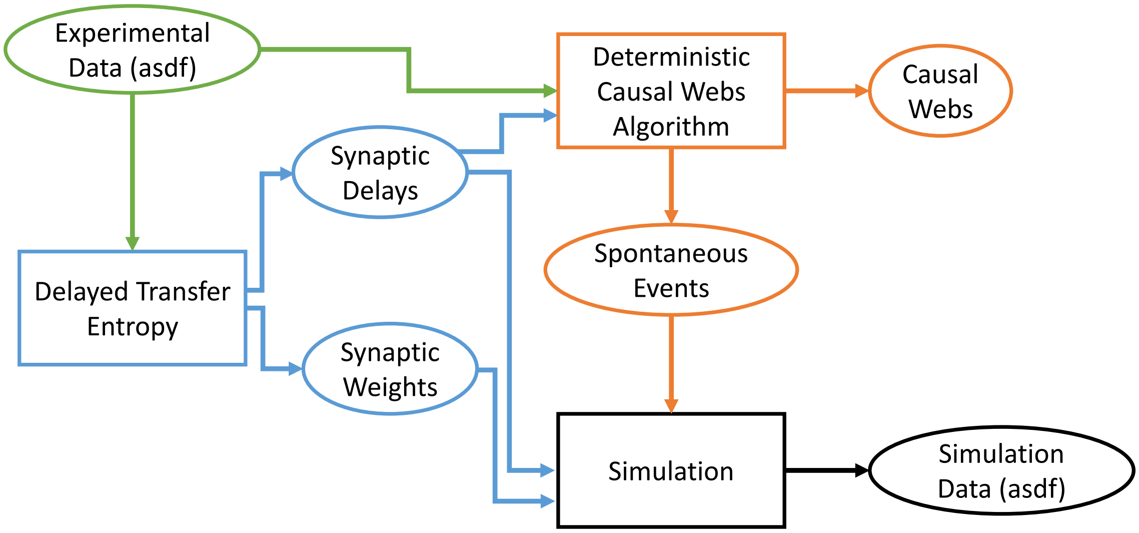
Experimental Data (asdf)
Deterministic Causal Webs Algorithm
Causal Webs
Synaptic Delays
Spontaneous Events
Delayed Transfer Entropy
Synaptic Weights
Simulation
Simulation Data (asdf)

Figure A.1: Flow diagram illustrating the production of data-enhanced simulations using the c-webs method.

```
% No longer optimizes data precision to enhance compatibility with foreign
% code...
% Rashid V. Williams-Garcia 12/2/15
function asdf = cxmodel5(weightmat,NT,Taurs,spontEvents,sig_del,delSDs)
    rng('shuffle','twister');
    N = length(weightmat);
    connmat = cell(N,1);
    for i=1:N
        connmat{i} = find(weightmat(i,:));
    end
    connects = cellfun(@numel,connmat);
    asdf = cell(N+2,1);
    asdf{end-1} = 1;
    asdf{end} = [N NT];
    prevZ = zeros(N,1);
    t = 1;
    dt = 0;
    DrivenSites = [];   %[driven site,activation time]
    %% Begin Simulation
    while t<NT
        %Locate avalanche seed nodes and times. First, check for ...
            spontaneous events:
        actives = cellfun(@(x) min(x(x>=t)),spontEvents,'UniformOutput',0);
        if sum(cellfun(@any,actives))==0
            break
        else
            actives(cellfun(@isempty,actives)) = {0};
            actives = cell2mat(actives);
            S = find(actives==t)';
            tS = min(actives(actives~=0));
            %The following ensures that earliest activity considered first,
            %whether spontaneous or driven. (marked for update)
            if isempty(DrivenSites)
                dt = tS-t;
                t = tS;
                S = find(actives==t)';
                actives = S; %actives should be a row vector
            else
                tD = min(DrivenSites(:,2));
                if tS>tD
                    dt = tD-t;
                    t = tD;
                    actives = DrivenSites(DrivenSites(:,2)==t)';
                elseif tS<tD
                    dt = tS-t;
                    t = tS;
                    S = find(actives==t)';
                    actives = S;
                elseif tS==tD
                    dt = tS-t;
                    t = tS;
                    S = find(actives==t)';
                    D = DrivenSites(DrivenSites(:,2)==t)';
                    actives = union(S,D);
                end
            end
        end
        %Increment node states appropriately
        prevZ(prevZ>1) = prevZ(prevZ>1)+dt;
        prevZ(prevZ>Taurs) = 0;
        actives = setdiff(actives,find(prevZ>1));
        if isempty(actives)
            t = t+1;
        else
            prevZ(actives) = 1;
            for i=1:numel(actives)
                asdf{actives(i)}=horzcat(asdf{actives(i)},t);
            end
            aSponts = intersect(actives,S);
            while ~isempty(actives) && t<NT
                %remove past drives
                if ~isempty(DrivenSites)
                    DrivenSites = DrivenSites(DrivenSites(:,2)>t,:);
                end
                for j=1:numel(actives)
                    TargetSites = connmat{actives(j)};
                    %roll the die for each outgoing connection:
                    temp = rand(1,connects(actives(j)));
                    %collect the respective weights:
```

```
                    x = weightmat(actives(j),TargetSites);
                    temp = (x>temp).*x;
                    temp = TargetSites(temp~=0); %these are the descendants
                    delaySD = delSDs(actives(j),temp);
                    at = t+sig_del(actives(j),temp);  %activation time
                    for k=1:numel(temp)
                        at(k) = at(k)+randi(2*delaySD(k)+1)-(delaySD(k)+1);
                    end
                    at(at<=t) = t+1;
                    DrivenSites = vertcat(DrivenSites,[temp',at']);
                end
                %move the clock:
                t = t+1;
                %update refractory periods
                prevZ(prevZ>1) = prevZ(prevZ>1)+1;
                prevZ(prevZ>Taurs) = 0;
                prevZ(actives) = 2;
                %Find spontaneously active sites at time t:
                S = cellfun(@(x) find(x==t),spontEvents,'UniformOutput',0);
                S(cellfun(@isempty,S)) = {0};
                S = find(cell2mat(S));
                %and driven ones:
                if isempty(DrivenSites)
                    D = [];
                else
                    D = DrivenSites(DrivenSites(:,2)==t,1);
                end
                actives = union(S,D);
                actives = setdiff(actives,find(prevZ>1));
                prevZ(actives) = 1;
                aSponts = intersect(actives,S);
```

```matlab
                if isempty(actives)
                    if ~isempty(DrivenSites)
                        DrivenSites = DrivenSites(DrivenSites(:,2)>t,:);
                    end
                    t = t+1;
                    break
                else
                    for i=1:numel(actives)
                        asdf{actives(i)}=horzcat(asdf{actives(i)},t);
                    end
                    if t>=NT
                        break
                    end
                end
            end
        end
    end
end
```

A.2 MATLAB Causal Webs Algorithm Code

```matlab
% asdf2avlets.m
% Utilizes a depth-first search to determine causal webs, their shapes, ...
    sizes, branching fractions, and spontaneous events.
% INPUTS
% asdf: N+2x1 cell containing spike information
% sig_del: NxN synaptic delays matrix
% REQUIRED FUNCTIONS: ASDFToSparse.m
% 4/19/16 UPDATES:
```

```
% Incorporates cWebs structure from Williams-Garcia et al. 2016.
% Calculates branching fractions.
% Rashid Williams-Garcia 12/10/15

function [cShapes,cWebs,cSizes,bFractions,spontEvents] = ...
    asdf2avlets2(asdf,sig_del)
    %asdf = asdfCast(asdf); %optional data optimization
    [raster,~] = ASDFToSparse(asdf);
    %% Main code
    N = length(asdf)-2;
    NT = asdf{end}(2);
    clear asdf
    %% Data precision optimization
    if NT<2^8
        p = 'uint8';
    elseif NT<2^16
        p = 'uint16';
    elseif NT<2^32
        p = 'uint32';
    else
        p = 'double';
    end
    if N*NT<2^8
        p2 = 'uint8';
    elseif NT<2^16
        p2 = 'uint16';
    elseif NT<2^32
        p2 = 'uint32';
    else
        p2 = 'double';
    end
```

```
%determine descendants
connmat = cell(N,1);
for i=1:N
    connmat{i} = find(sig_del(i,:));
end
dSD = zeros(size(sig_del));
dSD(sig_del~=0)=2; %std. dev. of delay values (should be an input)
maxDel = max(max(sig_del));
av = 0; %c-web counter
ac = 0; %activation counter
cShapes = cell(1,1);
cSizes = zeros(1);
cWebs = cell(1,1);
bFractions = zeros(1);
spontEvents = cell(N,1);
%find times with activity (active times)
aTimes = find(any(raster,1)~=0)';
while numel(aTimes)~=0
    %tic    %for debugging...
    dA = diff(aTimes);
    %identify macro-avalanche start and end times:
    t0 = min(aTimes);
    tf = aTimes(find(dA>maxDel,1));
   %tf-t0 %for debugging purposes
    if isempty(tf)  %this happens if the recording ends mid-activity
        tf = max(aTimes);
    end
    [sites,times] = find(raster(:,t0:tf));
    times = times+t0-1;
    activations = horzcat(sites,times);
    nA = size(activations,1);
```

```
        associations = zeros(nA,1);    %activation component associations
        cPairs = zeros(1,2,p2);   %causal pairs
        x = 0;  %causal pair counter
        for a=1:nA
            if associations(a)==0
                associations(a) = a;
            end
            n = activations(a,1);
            t0 = activations(a,2);
            %possible descendants of n and their delays
            PDs = connmat{n};
            if isempty(PDs) %n doesn't have any outgoing connections!
                continue
            else
                dat = t0+sig_del(n,PDs);%possible descendant activation times
                lb = dat-dSD(n,PDs);
                lb(lb<=t0) = t0+1;
                ub = dat+dSD(n,PDs);
                for j=1:numel(PDs)
                    if ub(j)>NT
                        dt = lb(j):NT;
                    else
                        dt = lb(j):ub(j);
                    end
                    temp = find(raster(PDs(j),dt),1);
                    if isempty(temp)    %n doesn't branch its activity!
                        continue
                    else
                        %about an order of magnitude faster than ismember...
                        b = find(activations(:,1)==PDs(j) & ...
                            activations(:,2)==dt(temp));
                        x = x+1;
                        cPairs(x,:) = [a+ac,b+ac];
                        if associations(b)==0
                            associations(b) = associations(a);
                        elseif associations(b)~=b
                            c = min(associations(a),associations(b));
                            associations(associations==associations(a)) = c;
                            associations(associations==associations(b)) = c;
                        elseif associations(b)==b
                            error('How could you let this happen?!')    %XD
                        end
                    end
                end
            end
        end
        avIDs = unique(associations);
        Nav = numel(avIDs);
        for y=1:Nav
            av = av+1;
            %find activations which are members of the avalanche:
            temp = find(associations==avIDs(y));    %activation indices
            avSize = numel(temp);
            n = activations(temp,1);    %neuron IDs
            t0 = activations(temp,2);   %timesteps
            BR = 0;
            c = [];
            for i=1:avSize
                [row,col] = find(cPairs==temp(i)+ac);
                %col is awesome! Numbers of 1's indicate numbers of
                %descendants of the activation temp(i); numbers of 2's
                %indicate numbers of ancestors!
                c = vertcat(c,row);    %row indices of associated c-pairs
                %Pick out spontaneous events:
                if sum(unique(col))==1 || isempty(col)
                    spontEvents{n(i)} = [spontEvents{n(i)} cast(t0(i),p)];
                end
                %Calculate branching fraction:
                BR = BR+numel(find(col==1));
            end
            c = unique(c);
            cShapes{av,1} = vertcat(cast([n t0],p));
            cSizes(av,1) = avSize;
            if avSize==1
                cWebs{av,1} = [];
                bFractions(av,1) = BR;  %should be 0
            else
                cWebs{av,1} = cPairs(c,:);
                bFractions(av,1) = BR/avSize;
            end
        end
        aTimes = aTimes(aTimes>tf);
        ac = ac+nA;
        %numel(aTimes)  %for debugging
        %toc
    end
end
```

APPENDIX B

On the Quasiperiodic Phase of the CBM

At high values of the refractory period, the mean-field approximation of the CBM (cf. Section 3.3) features a peculiar, oscillatory nonequilibrium phase, which may underlie the occurrence of certain types of seizures and/or other pathological behavior. We will want to understand the class of phase transition which leads to this quasiperiodic phase and the conditions under which it occurs, i.e., characterize the quasiperiodic phase and establish the analytical form of the phase boundary. To further understand this behavior, I initially applied Rouché's theorem, yielding inconclusive results. I then calculated the center manifold of the CBM mean-field map in an effort to reduce the dimensionality and examine the simplified dynamics on this invariant manifold. An additional tool which could help characterize the behavior of the map in the quasiperiodic phase, known as expansion entropy, had been developed recently, but not yet completely applied to the CBM [125]. These remain open problems for future study and my hope is that what is presented here will serve as a seed for future work. For simplicity, only the case $p_s = 0$ was considered.

B.1 Rouché's Theorem

Because the quasiperiodic phase appears when the stable fixed point in the ordered phase x^*_{1-} loses stability, the order parameter for the quasiperiodic transition might reflect the nature of the eigenvalues of the Jacobian. This loss of stability happens when the eigenvalues of the Jacobian transit across the unit circle, from the inside out; indeed, in our case, it is a complex-conjugate pair of eigenvalues which cross the unit circle at the quasiperiodic transition, as in a **Neimark-Sacker bifurcation**. We can attempt to determine when the number of eigenvalues inside the unit circle drops below τ_r by applying Rouché's theorem, which can be stated as

Rouché's theorem

Let K be a bounded region within a domain G, i.e., $K \subset G$, with a continuous boundary ∂K. If there are two holomorphic functions $f, g \in \mathcal{H}(G)$, where $\mathcal{H}(G)$ is the set of holomorphic functions in G, such that

$$|f(z)| < |g(z)|,$$

for $z \in \partial K$, then $f(z) + g(z)$ and $g(z)$ have the same number of roots in K.

Given the structure of the mean-field Jacobian matrix presented in Equation 3.17, we expand its determinant by minors and arrive at an equation for the eigenvalues $\lambda \in \mathbb{C}$ for any $\tau_r \geq 2$:

$$p(\lambda; \tau_r) = \lambda^{\tau_r - 1}(A - \lambda) + B \sum_{n=0}^{\tau_r - 2} \lambda^n = 0, \tag{B.1}$$

where $A = -(1 - \tau_r x_1^*)(2\kappa^2 p_1 p_2 x_1^* - \kappa(p_1 + p_2)) + B$ and $B = \kappa^2 p_1 p_2 x_1^{*2} - \kappa(p_1 + p_2) x_1^*$. For simplicity, we consider the case $\kappa > 1$ and hence $x_1^* = x_{1-}^*$, as given by Equation 3.22. The complex unit circle $|\lambda| = 1$ corresponds to the boundary ∂K containing the region $|\lambda| < 1$. As an example of the application of Rouché's theorem, consider the case $\tau_r = 2$, where we know that all the eigenvalues lie within the bounded region. In this case, the above polynomial becomes

$$p(\lambda; 2) = \lambda^2 - A\lambda - B. \tag{B.2}$$

Choosing $f(\lambda) = -A\lambda - B$ and $g(\lambda) = \lambda^2$, Rouché's theorem says that $p(\lambda; 2)$ should have the same number (2) of zeros as λ^2 within the bounded region $|\lambda| < 1$ if

$$|A\lambda + B| < |\lambda^2|, \tag{B.3}$$

which can be verified numerically along the boundary $|\lambda| = 1$ for $1 \leq \kappa \leq \kappa_{max} \approx 1.61$ and up to $\kappa \approx 3.57$. We know the quasiperiodic transition to occur when there are only $\tau_r - 2$ zeros inside of the bounded region—the other 2 having crossed over—and so we rewrite Equation B.1 as

$$p(\lambda; \tau_r) = \lambda^{\tau_r - 1}(A - \lambda) + B\lambda^{\tau_r - 2} + B \sum_{n=0}^{\tau_r - 3} \lambda^n. \tag{B.4}$$

Choosing $f(\lambda) = B\lambda^{\tau_r - 2}$ and $g(\lambda) = \lambda^{\tau_r - 1}(A - \lambda) + B \sum_{n=0}^{\tau_r - 3} \lambda^n$, we must find the maximum value of κ for which the following relation is satisfied:

$$\left| \lambda^{\tau_r - 1}(A - \lambda) + B \sum_{n=0}^{\tau_r - 3} \lambda^n \right| < \left| B\lambda^{\tau_r - 2} \right|. \tag{B.5}$$

It was found that this was never satisfied for the conditions stated here. We must note, however, that Rouché's theorem provides a *necessary, though not sufficient* condition for the functions $f(z) + g(z)$ and $g(z)$ to have the same number of zeros, and so our application of Rouché's theorem appears to be inconclusive.

B.2 Center Manifold Theorem

Another approach to understand the nature of the quasiperiodic phase of the mean-field system $\mathbf{x}(k+1) = F[\mathbf{x}(k)]$ is by calculating the **center manifold** of the linearized mean-field map:

$$\mathbf{x}(k + 1) = J\mathbf{x}(k), \tag{B.6}$$

where $\mathbf{x} = (x_1, x_2, ..., x_{\tau_r})$ and the form of the Jacobian J is given in Equation 3.17. If the right-hand side of this equation is C^r, i.e., r times continuously differentiable, then the **center manifold theorem** guarantees the existence of a finite neighborhood $\mathcal{U}$ around each fixed point $\mathbf{x}^* = (x^*_{1-}, x^*_{1-}, ..., x^*_{1-})$ in which there is at least one of the following:

- a unique C^r stable manifold, $M^s \in \mathcal{U}$,
- a unique C^r unstable manifold, $M^u \in \mathcal{U}$,
- or a (not necessarily unique) C^{r-1} center manifold, $M^c \in \mathcal{U}$.

Eigenvectors corresponding to eigenvalues λ of J with $|\lambda| < 1$ span the stable eigenspace E^s, whereas eigenvectors corresponding to eigenvalues with $|\lambda| > 1$ span the unstable eigenspace E^u; these eigenspaces define the manifolds M^s and M^u, respectively. The center manifold is defined by eigenvectors corresponding to eigenvalues $|\lambda| = 1$. A nonlinear coordinate transformation to a **normal form** separates these manifolds.

Most importantly, the center manifold is real, two-dimensional, and F-invariant; it passes through $\mathbf{x}^*$, tangent to its corresponding eigenspace E^c, on which J acts as a rotation. This leaves a $(\tau_r - 2)$-dimensional, F-invariant, real submanifold passing through $\mathbf{x}^*$ tangent to the corresponding stable eigenspace E^s, on which J acts as a contraction. Locally near $\mathbf{x}^*$, M^c is the graph of a function $f : E^c \rightarrow E^s$. Finally, if $x_0 \in \mathcal{U}$, then the orbit of x_0 under F converges to M^c under iteration of the map.

Next, we perform our coordinate transformation, redefining the fixed point $\mathbf{x}^*$ as the origin: $\mathbf{x}' = \mathbf{x} - \mathbf{x}^*$. The iterated map becomes $\mathbf{x}'(k+1) = F'[\mathbf{x}'(k)]$ with the corresponding Jacobian J':

$$J' = \begin{pmatrix} \frac{\partial F_1'}{\partial x_1'} & \frac{\partial F_1'}{\partial x_2'} & \cdots & \frac{\partial F_1'}{\partial x_{\tau_r}'} \\ 1 & 0 & \cdots & 0 \\ 0 & 1 & \cdots & 0 \\ \vdots & \vdots & \ddots & \vdots \\ 0 & 0 & \cdots & 0 \end{pmatrix}, \tag{B.7}$$

where $x_1'(k+1) = F_1'[x_1'(k)]$ This new Jacobian J' is transformed to real **Jordan normal form** by finding the matrix V such that $J^R = V^{-1} J' V$ where J^R is the Jordan normal form of our transformed Jacobian J'. Supposing the matrix J' has $\tau_r/2$ complex conjugate pairs of eigenvectors of the form $u_z \pm iv_z$, the matrix V is constructed in the following way:

$$V = [v_1|u_1|v_2|u_2|\ldots], \tag{B.8}$$

for $z \in \{1, 2, ..., \tau_r/2\}$. We then transform our state vectors $\mathbf{x}'$ by the appropriate matrix operation, i.e., $\mathbf{x}' = V\mathbf{y}$, to arrive at a new, linearized map $\mathbf{y} \mapsto J^R\mathbf{y}$. At this point, we include the nonlinear portion,

$$G(\mathbf{x}') = \begin{pmatrix} -a(1-\tau_r x_{1-}^*)x_1'^2 + x_0'x_1'(-2ax_{1-}^* + b) - ax_0'x_1'^2 \\ 0 \\ \vdots \\ 0 \end{pmatrix}, \tag{B.9}$$

in the original map

$$\mathbf{x}' \mapsto J'\mathbf{x}' + G(\mathbf{x}'), \tag{B.10}$$

where $a = \kappa^2 p_1 p_2$ and $b = \kappa(p_1 + p_2)$. After this transformation, we have

$$\mathbf{y} \mapsto J^R\mathbf{y} + G(\mathbf{y}), \tag{B.11}$$

where $G(\mathbf{y}) = V^{-1}G(\mathbf{x}')$. We can finally approximate the dynamics on the center manifold by iterating an initial state vector $\mathbf{y}(k = 1)$ and plotting the first two components (y_1, y_2) of the resulting $\mathbf{y}$ (see Figure B.1). One of the hopes here was that **elliptic islands** would appear, as in other cases of quasiperiodicity, however, this was not found.

After having made the coordinate transformation $\mathbf{x}' = \mathbf{x} - \mathbf{x}^*$, it may be possible to determine quasiperiodic phase boundary using the characteristic polynomial corresponding to the transformed Jacobian J':

$$\lambda^{\tau_r} - \lambda^{\tau_r - 1}\frac{\partial F_1'}{\partial x_1'} - \lambda^{\tau_r - 2}\frac{\partial F_1'}{\partial x_z'} - \ldots - \lambda\frac{\partial F_1'}{\partial x_z'} - \frac{\partial F_1'}{\partial x_z'} = 0, \tag{B.12}$$

for any $z > 1$. We focus on the phase boundary where $|\lambda| = 1$ and solutions which yield eigenvalues of the form $\lambda = e^{i\phi}$ on the center manifold, and which satisfy the characteristic

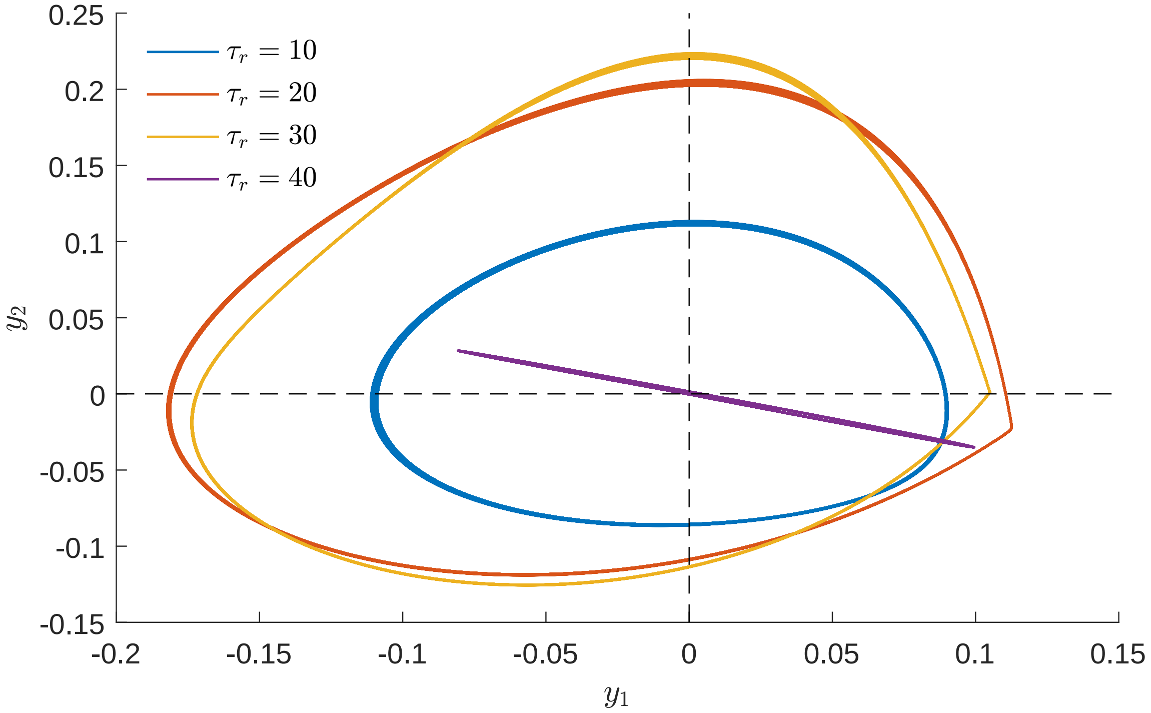

Figure B.1: Quasiperiodic orbits on the center manifold for various values of the refractory period τ_r along $\kappa = \kappa_{max}$ for a $B = 0.5$, $p_s = 0$ mean-field approximation of the CBM. These trajectories are the final 10^4 iterations of the map after a total of 10^5 iterations have been performed.

polynomial equation. This yields two equations for large τ_r, one for the real component,

$$\cos(\tau_{\mathsf{r}}\phi) = \frac{\partial F_1'}{\partial x_1'}\cos(\tau_{\mathsf{r}}-1)\phi + \frac{1}{2}\frac{\partial F_1'}{\partial x_z'}\left(\csc\frac{\phi}{2}\sin\frac{2\tau_{\mathsf{r}}-3}{2}\phi + 1\right), \tag{B.13}$$

and the other from the imaginary component

$$\sin(\tau_{\mathsf{r}}\phi) = \frac{\partial F_1'}{\partial x_1'}\sin(\tau_{\mathsf{r}}-1)\phi + \frac{1}{2}\frac{\partial F_1'}{\partial x_z'}\left(\cot\frac{\phi}{2} - \csc\frac{\phi}{2}\cos\frac{2\tau_{\mathsf{r}}-3}{2}\phi\right). \tag{B.14}$$

In principle, one would have to solve these equations at a specified τ_r for κ, which would correspond to the quasiperiodic phase boundary.

B.3 Expansion Entropy

It was conjectured that the **expansion entropy** H_0, as defined in [125], may serve as an order parameter for the quasiperiodic transition. This application was not pursued to completion and so may provide a future research project. The quantity H_0 is essentially the average of the sum of positive Lyapunov exponents; when $H_0 > 0$, the trajectories are chaotic. The expansion entropy is defined as

$$H_0(f,S) = \lim_{k'\to\infty}\frac{\ln E_{k',k}(f,S)}{k'-k}, \tag{B.15}$$

where $f_{k',k} : M \to M$ is a discrete map which takes a point in the manifold M at an iteration k and returns it to M at another iteration k', i.e., it is analogous to the quantum mechanical time-evolution operator. A **restraining region** S within M, i.e., $S \subset M$, contains trajectories of the map after many iterations, $k' \to \infty$. In our case, we are interested in the $k_{in} = 2$ CBM mean-field map in τ_r dimensions,

$$f_{k+1,k} = \begin{cases} x_0(k)\kappa x_1(k)(1-\kappa p_1 p_2 x_1(k)) \\ x_1(k) \\ \vdots \\ x_{\tau_r - 1}(k) \end{cases} \tag{B.16}$$

and the manifold M, which is an n-simplex Δ^n of dimension $n = \tau_r$:

$$\Delta^n = \{(x_1, x_2, ..., x_n) \in \mathbb{R}^n \mid 0 \leq x_i \leq 1 \;\wedge\; \sum_{i=1}^{n} x_i = 1 \;\forall\; i\}. \tag{B.17}$$

The quantity $E_{k',k}(f, S)$ is given by

$$E_{k',k}(f, S) = \frac{1}{\mu(S)} \int_{S_{k',t}} G(Df_{k',t}(x)) d\mu(x), \tag{B.18}$$

where $\mu(S)$ is the volume of the restraining region S and $G(Df_{k',k}(x))$ is the product of the **singular values** of the Jacobian $A = Df_{k',k}(x)$ which are greater than 1, i.e.,

$$G(A) = \prod_{\sqrt{\lambda} > 1} \sqrt{\lambda}, \tag{B.19}$$

where λ are eigenvalues of $A^\top A$. If all singular values of A are less than 1, then $G(A) = 1$.

APPENDIX C

The Strongly-Driven BTW Model

Here I describe a strongly-driven BTW model which lacks a separation of timescales[1]. A thorough examination of this model has not yet been completed, but has been initiated. In this model, “events” (or “activations”) correspond to topplings, not grain drops. This strongly-driven two-dimensional BTW model is summarized by the following algorithm:

1. *Initialization.* Start board in random configuration $z_i \leq z^{th}$. Set the clock to $t = 1$ and prepare spontaneous grain drops by drawing inter-drop intervals Δt_s from a specified distribution.

2. *Drive.* Advance to the time t corresponding to the next spontaneous drop and drop a grain on a random site i: $z_i \rightarrow z_i + 1$

3. *Relaxation.* For all sites i with $z_i \geq z^{th}$, topple one grain to each of its neighboring sites: $z_i \rightarrow z_i - 4$ and $z_{\mathcal{N}(i)} \rightarrow z_{\mathcal{N}(i)} + 1$. Grains are conserved within the bulk, where each site has four neighbors, but not at the edges, where sites can have as few as two neighbors. Continue until $z_i \leq z^{th}$ for all sites i.

4. *Iteration.* Return to **2.**

---

[1] For an analysis of the BTW model with a full separation of timescales, refer to Section 3.1.

APPENDIX D

Sudden Quench Dynamics

Using a dynamical response approach, it may be possible to extract information regarding the nature of the state of a living neural network. This approach makes use of **critical slowing down**, a phenomena in which the relaxation time of the dynamics τ_0 in response to a stimulus diverges for a system at criticality: $\tau_0 \propto \xi_\perp^z$, where $\xi_\perp$ is the correlation length and z the dynamical critical exponent. Presented here are a set of notes on the application of this approach to the mean-field approximation of the cortical branching model (CBM) (cf. Section 4.1.1). It is expected that such an approach would be of use to experiments wherein a living system is exposed to a precisely-controlled stimulus. We simulate this experimental arrangement by applying a time-dependent spontaneous activation probability, a **sudden quench** (see Figure D.1), to the mean field, then observe the resulting **transient dynamics** and estimate the duration of the transient τ_0. Recent experiments demonstrate the presence of a transient, immediately following sudden stimulus onset, during which "supercritical" dynamics are observed [78].

For different parameter values, we observe the duration of the transient to vary sufficiently to identify the nonequilibrium Widom line and distinct phases of the mean-field CBM; the transient duration is noticeably longer near and along the nonequilibrium Widom line. This represents a novel dynamical probe which can be utilized by experimentalists to reveal proximity to critical or quasicritical states. We estimate the duration of this tran-

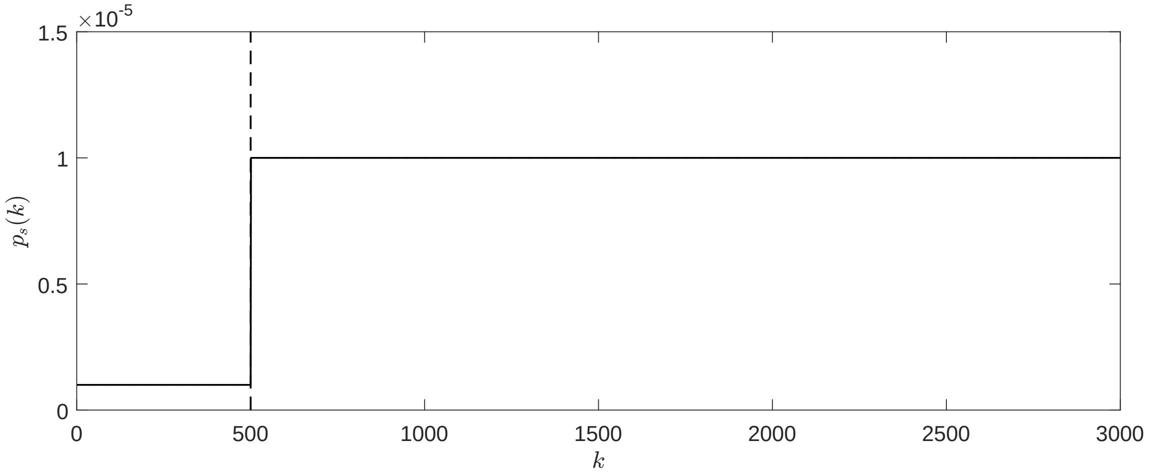

Figure D.1: The spontaneous activation probability is a function of time which starts at $p_s = 10^{-6}$ and, after 500 iterations, suddenly increases to $p_s = p_s'$, the stimulus intensity. Here, $p_s' = 10^{-5}$.

sient for different parameter values to predict the nature of the response of a living neural network to stimulus of different stimulus intensities and under different pharmacological conditions. Additionally, this provides further hope for employing the nonequilibrium Widom line framework and testing the quasicriticality hypothesis in a living system. Avalanche scaling behavior and adherence to scaling relations will require simulations of the CBM or estimations beyond the mean field.

Using the *ex vivo* preparation in [78] as a contextual example, we interpret the spontaneous activation probability p_s as the intensity (and/or contrast) of the stimulus video and apply to the mean-field system a sudden quench in p_s, from a "resting" value of 10^{-6}, as illustrated in Figure D.1. The branching parameter and refractory period can be manipulated experimentally by adjusting levels of excitation and inhibition using pharmacological agents, although some adjustments may be made dynamically by the homeostatic mechanisms of a living neural network in response to levels of activity. Prior to activation of the stimulus, the mean-field map is allowed to reach the appropriate stable fixed point for the specific parameter values. Following activation of the stimulus, the mean-field map undergoes transient dynamics, during which the density of active nodes x_1 fluctuates before reaching a new stable fixed point x_1^*. We identify the duration of the transient period as the number of time steps required to reach this new fixed point. The duration of the transient period is estimated by determining the first time step k' (following the stimulus) for which the condition $|x_1(k) - x_1^*| < 10^{-10}$ is satisfied and maintained for all $k > k'$. If the condition is not met after a large number K of iterations of the map—as is the case for the quasiperiodic phase—the duration of the transient period k' is set to K.

The character of the transient period depends on the parameters of the model (e.g., κ, τ_r, p_s, etc.). For instance, see Figure D.2, where we plot the $\kappa = 1.0$ fraction of active nodes as a function of time for $\tau_r = 1$ and $\tau_r = 5$, while varying the stimulus intensity p_s' between values 10^{-3} and 10^{-1}. Increasing the refractory period τ_r to 5 time steps results in a marked difference in the qualitative behavior of the system during the transient period, involving more fluctuations of the order parameter. To better understand how the duration of the transient phase τ_0 depends on the variables of the model, we plot τ_r versus κ with τ_0 on a color axis for stimulus values $p_s' = \{10^{-5}, 10^{-4}, 10^{-3}\}$ (see Figure D.3).

The location of the nonequilibrium Widom line is indicated by an increase τ_0 around $\kappa = 1.0$ which fades as we increase p_s—the critical phase transition located at $\kappa = 1.0$ when $p_s = 0$ is not plotted. In contrast to the nonequilibrium phase diagrams presented in Section 4.1, these plots indicate locations of phase transitions in terms of the relaxation timescales of the mean-field CBM—diverging relaxation times indicate oscillatory or critical dynamics. While these results may not give precise quantitative predictions, qualitative predictions of how the transient duration τ_0 scales with the stimulus intensity p_s' may be accurate and useful in determining the nature of the dynamics of a living system, e.g., closeness to criticality. In Figure D.4, we vary κ, while maintaining $\tau_r = 1$, to illustrate how τ_0 scales

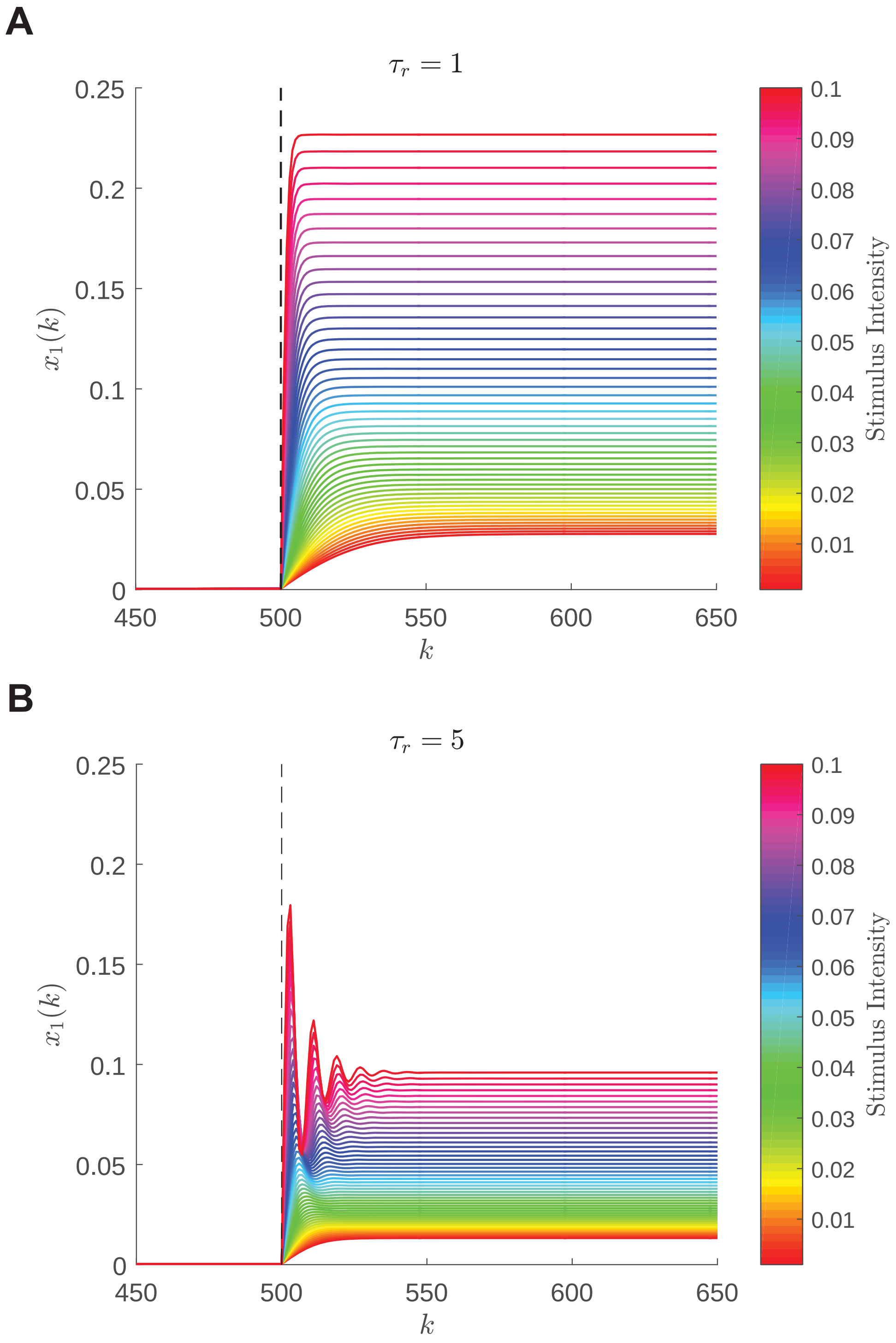

Figure D.2: When the refractory period is low (A), the model responds "adiabatically" to the sudden quench. With higher refractory periods (B), the model responds to the sudden quench by over-shooting the stable fixed point.

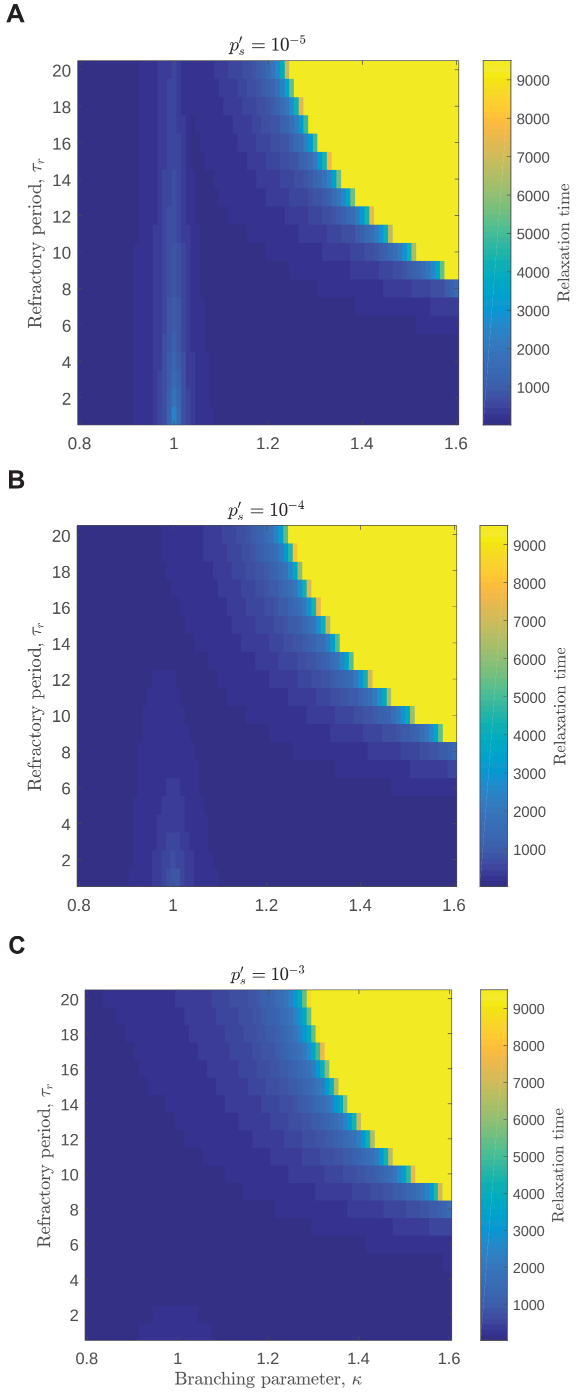
$p'_s = 10^{-5}$

$p'_s = 10^{-4}$

$p'_s = 10^{-3}$

Figure D.3: The relaxation time, i.e., the duration of the transient phase, peaks at the critical point and along the nonequilibrium Widom line. Compare to Figure 4.1.

with the stimulus intensity p'_s in this case.

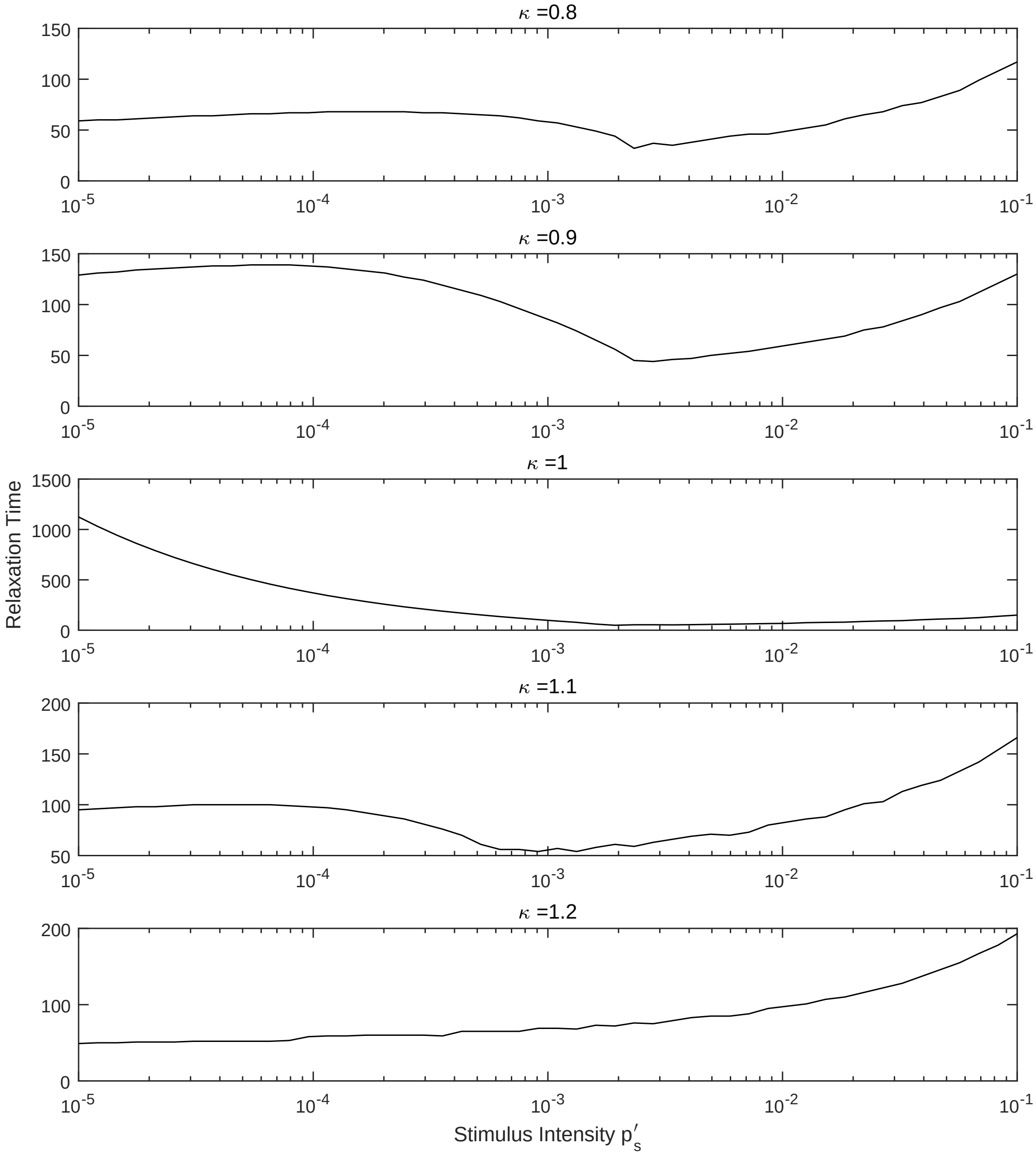

Figure D.4: The "adiabatic" stimuli intensities result in a different scaling of the relaxation time versus the stimulus intensity, which depends on proximity to the nonequilibrium Widom line. The relaxation time near $\kappa = 1$ is largest at small values of the stimulus intensity, due to critical slowing and proximity to the critical point at $\kappa = 1$ when $p_s = 0$.

APPENDIX E

Generalized Cortical Branching Models

Here I introduce a family of generalizations of the CBM called generalized cortical branching models (gCBMs). These models incorporate some more realistic features of living neural networks, including activity transmission delays and inhibition. In developing these models, I held the following objectives in mind:

(1) to model the interaction between timescales present in living neural networks, e.g., synaptic delays, refractory periods, metabolic timescales, etc.,

(2) to formally establish the so-called "balance of excitation and inhibition" and its relation to criticality, and

(3) to characterize any additional phases and phase transitions of a more realistic CBM.

I wanted to understand how different timescales in systems far from equilibrium interact to produce the wealth of behaviors observed in living neural networks.Analytic approaches would be most valuable in such a endeavor and so this appendix focuses on results from mean-field approaches—the typical first step in understanding the complex dynamics of a new model.

The first model in this class, the delayed-transmission CBM (dCBM), incorporates activity transmission delays. The second model is the Excitatory/Inhibitory CBM (EICBM)[1], which incorporates inhibitory nodes able to act directly on excitatory nodes, i.e., via **site inhibition**, and those which act on synapses, i.e., via **bond inhibition**.

---

[1] I began developing the EICBM in Heidelberg, Germany at a coffee shop, *Coffee Nerd*, which had some of

E.1 The Delayed-Transmission CBM

I briefly considered a situation where, as in living neural networks, activity transmission delays play an important role in the dynamics. When we account for this timescale of interaction with $k_{in} = 1$, the mean-field equation (cf. Equation 3.18) becomes

$$\begin{aligned} x_1(k+1) &= \left(1 - \sum_{z=1}^{\tau_r} x_z(k)\right)\left(cx_1(k-d+1) + p_s\right) \\ x_z(k+1) &= x_{z-1}(k), \end{aligned} \tag{E.1}$$

where d is the activity transmission delay. Note that since we are only changing the timescale of the interactions, we do not change how nodes cycle through states during the refractory period or the rule requiring nodes be quiescent prior to driven activation. That is, the timescale of interaction is different, but the timescales of the internal dynamics remain the same. For values $d > 1$, the fixed points are unchanged, though the equation for $x_1(k+1)$ becomes

$$x_1(k+1) = \left(1 - \sum_{z=1}^{\tau_r} x_z(k)\right)\left(cx_d(k) + p_s\right), \tag{E.2}$$

where $x_d(k)$ replaces $x_1(k-d+1)$ due to the dynamics of the CBM and as long as $d \leq \tau_r$; for $d > \tau_r$, the mean-field map becomes non-Markovian. This does, however, have an effect on the Jacobian. With $p_s = 0$, the Jacobian matrix presented in Equation 3.17, for example, becomes

$$J = \begin{pmatrix} A & B' & B & \cdots & B & B \\ 1 & 0 & 0 & \cdots & 0 & 0 \\ 0 & 1 & 0 & \cdots & 0 & 0 \\ \vdots & \vdots & \vdots & \ddots & \vdots & \vdots \\ 0 & 0 & 0 & \cdots & 1 & 0 \end{pmatrix}, \tag{E.3}$$

---

the best cappuccinos I ever had; those nerds really know their espresso!

when $d = 2$ and where

$$B' = \frac{\partial x_1(k+1)}{\partial x_2(k)} = c\left(1 - \sum_{z=1}^{\tau_r} x_z(k)\right) - cx_2(k). \tag{E.4}$$

The condition for the fixed point $x_1^* = 0$ to lose stability changes subtly from $\kappa = 1$ to $\sqrt{\kappa} = 1$; generally, the condition becomes $\kappa^{1/d} = 1$, which has no noticeable effect on the location of the fixed point. A thorough examination should be performed in future studies to determine if any substantial changes occur for $k_{in} > 1$.

E.2 The Excitatory/Inhibitory CBM

A major shortcoming of the CBM presented in Chapters 3 and 4 is the absence of inhibitory neurons. Real neural networks typically include both excitatory and inhibitory influences, and a "balance" of these influences is often purported to occur at criticality [126, 36, 127]. Of course, neural network models with inhibition are not new, but stochastic branching models with inhibition, such as the one presented, are. Intuitively, the excitatory/inhibitory CBM (EICBM) features inhibitory nodes which can "veto" the influence of excitatory nodes: excessive excitation stochastically elicits inhibitory effects, effectively altering connection strengths and the influence of the external stimulus by counteracting excitation.

Previous attempts have been made to determine the nature of the various phases networks such as these can exhibit [128], but these studies were based on simulations of realistic models of neurons, such as leaky integrate-and-fire models, and focused on numerics as opposed to analytics. What resulted was a qualitative description of the phase diagram and the phases therein, based on simulations of models with many parameters. Although I was inspired by the work of Brunel et al., I sought to improve upon it by developing a more general, analytically-tractable model with fewer parameters, in order to rigorously characterize the various phases and transitions between them.

The full EICBM consists of a network of N_E excitatory nodes and N_I inhibitory nodes

($N_E + N_I = N$, the total number of nodes); excitatory (inhibitory) nodes only produce excitatory (inhibitory) connections, while all nodes, whether excitatory or inhibitory, can receive input from either type. As in the CBM, excitatory nodes influence the behavior of the nodes to which they connect in a stochastic way: at a time step t, given an active node i, a quiescent node j, and a connection from i to j, node j will become active in time step $t + 1$ with probability P_{ij} in the absence of external stimulation. The state of individual nodes is described by the dynamical variable $z \in \mathbb{Z}$: quiescent nodes are indicated by $z = 0$, active nodes by $z = 1$, and refractory nodes by any $z \in \{2, ..., \tau_r\}$. What sets the EICBM apart from the CBM, however, is the presence of inhibitory nodes which can counteract, or *veto*, the action of excitatory nodes. There are two mechanisms by which this can be accomplished, where inhibitory nodes can

1. act directly on other nodes to prevent their activation, and/or
2. selectively disable connections.

We refer to the first mechanism as **site inhibition** and the second as **bond inhibition**. These distinct mechanisms are considered separately in the following sections.

E.2.1 Site Inhibition

This form of inhibition counteracts excitatory influences regardless of the source and we call this variation on the EICBM the site-inhibition EICBM (or siCBM for short). Biologically, this may correspond to a hyperpolarizing influence which counteracts any depolarization in the membrane potential of the postsynaptic neuron. In the EICBM, this is modeled stochastically, where given excitatory and inhibitory influences to a target node, there is a **veto probability** v with which the target node is prevented from activating.

As a first example, consider three nodes in the absence of an external stimulus: two active nodes i and j, and a quiescent node k; node i is excitatory and node j is inhibitory.

Connections exist from nodes i and j to k with strengths P_{ik} and P_{jk}. If only the connection from i to k transmits activity, then k becomes active with probability P_{ik}. However, if both nodes i and j transmit to k, then node k becomes active with probability $(1-v)P_{ik}P_{jk}$, where v is the veto probability. In this example, both nodes transmit activity to k, but node j fails to veto the excitatory influence from i and hence k activates. If we allow for an external stimulus, then k becomes active with probability $(1-p_s)(1-v)P_{ik}P_{jk} + p_s(1-v)^2P_{ik}P_{jk}$. Notice that a veto term exists for each excitatory influence and that the external stimulus p_s is assumed to be excitatory.

To develop a mean-field approximation, translational invariance is introduced by ensuring that each node receives a fixed number of inhibitory (in-degree k_i) and excitatory (in-degree k_e) connections. Consider the simplest siCBM, i.e., the one with $k_e = k_i = 1$ and $\tau_r = 1$, so we have a two-element state space $S = \{0, 1\}$. The excitatory and inhibitory nodes have respective connection strengths P_e and P_i. States of excitatory and inhibitory nodes are referred to as z_e and z_i; the state of the representative node is z_o; the state of the system is represented as the 3-tuple $\mathbf{z} = (z_o, z_e, z_i)$.

As with the mean-field CBM, first consider the probabilities for $z_o = 0$ to calculate the probabilities for $z_o = 1$ under the various configurations $\mathbf{z}$; that is, $W(\mathbf{z} \to 1) = 1 - W(\mathbf{z} \to 0)$, where $W(\mathbf{z} \to z)$ is short-hand indicating the representative node's transition probability into state z given the prior system configuration $\mathbf{z}$. The fraction of excitatory and inhibitory nodes in any state $z \in S$ are respectively referred to as x_z and y_z: in this case, $x_0 + x_1 = y_0 + y_1 = 1$. We seek to evaluate the mean-field map

$$\begin{aligned} x_1(k+1) &= x_0(k)F(\mathbf{z}(t)) \\ y_1(k+1) &= y_0(k)F(\mathbf{z}(t)), \end{aligned} \tag{E.5}$$

where k indicates the iteration of the map. Notice that the term $F(\mathbf{z}(k)) = \sum_{\mathbf{z}} W(\mathbf{z} \to 1)x_{z_e}(k)y_{z_i}(k)$ is identical for both the excitatory and inhibitory maps since both kinds of nodes receive the same input to ensure translational invariance. I will now go through the various realizations of $\mathbf{z}$ in detail.

No Prior Activity This is the most trivial case, in which the initial state is $\mathbf{z} = (0, 0, 0)$. Because there is no prior activity to consider, the representative node is subject only to the influence of the external field, and so $W(\mathbf{z} \to 1) = p_s$. The contribution to the activation probability is then $p_s x_0 y_0$.

Active Excitatory Node This is the next simplest case, with initial state $\mathbf{z} = (0, 1, 0)$. Consider $\mathbf{z} \to 0$: that is, despite there being an active excitatory node, it does not transmit activity, nor does the external field drive the representative node to activation. Thus we have $W(\mathbf{z} \to 0) = (1 - p_s)(1 - P_e)$ or $W(\mathbf{z} \to 1) = p_s + P_e(1 - p_s)$. The contribution to the activation probability is $(p_s + P_e(1 - p_s))x_1 y_0$.

Active Inhibitory Node Now we start with initial state $\mathbf{z} = (0, 0, 1)$ and consider $\mathbf{z} \to 0$. There are three ways for this to occur: **(1)** the target node does not spontaneously activate and the inhibitory node does not transmit, **(2)** the target node does not spontaneously activate and the inhibitory node does transmit and does nothing, and **(3)** the spontaneous activation is defeated by the inhibitory input. These situations occur with probabilities $(1 - p_s)(1 - P_i)$, $(1 - p_s)P_i$, and $g p_s P_i$, respectively, where g is a constant describing the coupling between the inhibitory nodes and the external field relative to the influence the inhibitory nodes have on influences from excitatory nodes; take this to be $g = 1$ for simplicity. Thus $W(\mathbf{z} \to 1) = p_s(1 - P_i)$ with contribution $p_s(1 - P_i)x_0 y_1$. Note that here, it may be useful to consider the effect an inhibitory node may have on a quiescent node: an inhibitory node acting on a quiescent node may cause the node become hyperpolarized which may be represented by states $z > 1$, already used to represent refractory states.

Both Input Nodes Active This is the most complicated case, $\mathbf{z} = (0, 1, 1)$, in which there are five ways for $\mathbf{z} \to 0$ to occur: **(1)** the target node does not spontaneously activate and the inhibitory and excitatory nodes do not transmit, **(2)** the target node does not spontaneously activate, the excitatory node fails to transmit, but the inhibitory node does transmit (doing nothing), **(3)** the target node does not spontaneously activate, but both the inhibitory and excitatory nodes transmit, and the inhibition vetoes the excitation, **(4)** the excitatory node fails to transmit and the spontaneous activation is vetoed by the inhibition, and finally **(5)** both the spontaneous activation and excitation are vetoed by the inhibition. These situations occur with probabilities $(1-p_s)(1-P_e)(1-P_i)$, $(1-p_s)(1-P_e)P_i$, $g(1-p_s)P_eP_i$, $gp_s(1-P_e)P_i$, and $g^2p_sP_eP_i$, respectively. Note that we could potentially have different couplings g with respect to spontaneous activation and excitation, e.g., g_s and g_e, but I considered only the case $g_s = g_e = g$, for simplicity. And thus the contribution to the activation probability is $[P_e(1-gP_i)(1-p_s) + p_s(1-gP_i) + g(1-g)P_eP_ip_s]x_1y_1$ or, with $g = 1$, $[P_e(1-P_i)(1-p_s) + p_s(1-P_i)]x_1y_1$.

All together, we have $F(\mathbf{z}(k)) = p_s + (1-p_s)P_ex_1(k) - P_i(p_s + (1-p_s)P_ex_1(k))y_1(k)$, and the resulting mean-field approximation for the siCBM, in the case $k_e = k_i = 1$, is a two-dimensional discrete iterated map,

$$\begin{aligned} x_1(k+1) &= (1-x_1(k))(p_s + (1-p_s)P_ex_1(k) - P_i(p_s + (1-p_s)P_ex_1(k))y_1(k)) \\ y_1(k+1) &= (1-y_1(k))(p_s + (1-p_s)P_ex_1(k) - P_i(p_s + (1-p_s)P_ex_1(k))y_1(k)). \end{aligned} \tag{E.6}$$

In the absence of spontaneous activation, i.e., $p_s = 0$, we have $F(\mathbf{z}(k)) = P_e(1-P_iy_1(k))x_1(k)$, and we see there are three fixed-points $\mathbf{x}^* = (x_1^*, y_1^*)$: $\mathbf{x}_0^* = (0,0)$ and

$$\mathbf{x}_\pm^* = \left(\frac{(1+P_i)\sqrt{P_e} \pm G}{2P_i\sqrt{P_e}}, \frac{(1+P_i)P_e \pm G\sqrt{P_e}}{2P_iP_e}\right) \tag{E.7}$$

where $G = \sqrt{P_e + 2P_i(2-P_e) + P_eP_i^2}$. When we perform stability analysis on this map, we find that the fixed point $\mathbf{x}_0^*$ is stable so long as $P_e < 1$, which is nearly always true. We next consider arbitrary k_e and k_i.

Arbitrary Inputs

In our mean-field treatment of the CBM, we found a phase transition only for $k_{in} > 1$, as so we will be interested in examining cases with arbitrary k_e and k_i. First, when there are two excitatory inputs and a single inhibitory input, i.e., $k_e = 2$ and $k_i = 1$:

$$\begin{aligned} F(x_1, y_1; k) &= gp_3 v(1-v)\kappa^2 p_1 p_2 x_1^2(k) y_1(k) \\ &\quad + (1 - gp_3 v y_1(k))(\kappa(p_1 + p_2)x_1(k) - \kappa^2 p_1 p_2 x_1^2(k)), \end{aligned} \tag{E.8}$$

where κp_1 and κp_2 are activity transmission probabilities for the excitatory inputs. For arbitrary numbers of inputs of either type, we perform a multi-binomial expansion to arrive at

$$\begin{aligned} W(\mathbf{z} \to 0) = &\sum_{q=0}^{1} \sum_{k_1=0}^{\delta_{z_1,1}} \ldots \sum_{k_d=0}^{\delta_{z_d,1}} (-p_s)^{1-q} (-p_1)^{(1-k_1)\delta_{z_1,1}} \ldots (-p_d)^{(1-k_d)\delta_{z_{d-1},1}} \times \ldots \\ &\ldots \times \prod_{j=1}^{k_{in}^i} \sum_{n_1=0}^{\delta_{\tilde{z}_j,1}} \ldots \sum_{n_m=0}^{\delta_{\tilde{z}_j,1}} \left[(-v)^{n_1+\ldots+n_m} \tilde{p}_j^{1-\delta_{n_1,0}\ldots\delta_{n_m,0}} \right], \end{aligned} \tag{E.9}$$

where $d \equiv k_e$ and $m \equiv (1-q) + (1-k_1)\delta_{z_1,1} + \ldots + (1-k_d)\delta_{z_d,1}$. This is particularly useful for computational implementations of the siCBM.

Jacobian Matrices

To understand the nature of the phases exhibited by the model, we turn to a generic analysis of the siCBM Jacobian matrices. The mean-field maps corresponding to an siCBM with an arbitrary number of excitatory and inhibitory inputs, as well as arbitrary excitatory and inhibitory node refractory periods, τ_r and $\tilde{\tau}_r$, respectively, will be of the form

$$\begin{aligned} x_1(k+1) &= x_0(k)F(\mathbf{x}(k),\mathbf{y}(k)) & y_1(k+1) &= y_0(k)F(\mathbf{x}(k),\mathbf{y}(k)) \\ x_2(k+1) &= x_1(k) & y_2(k+1) &= y_1(k) \\ &\vdots & &\vdots \\ x_{\tau_r}(k+1) &= x_{\tau_r-1}(k) & y_{\tilde{\tau}_r}(k+1) &= y_{\tilde{\tau}_r-1}(k). \end{aligned} \tag{E.10}$$

The corresponding Jacobian matrix will be of the form

$$J = \begin{pmatrix} A & B & \cdots & B & C & 0 & \cdots & 0 \\ 1 & 0 & \cdots & 0 & 0 & 0 & \cdots & 0 \\ 0 & 1 & \cdots & 0 & 0 & 0 & \cdots & 0 \\ \vdots & \vdots & \ddots & \vdots & \vdots & \vdots & \ddots & \vdots \\ D & 0 & \cdots & 0 & E & F & \cdots & F \\ 0 & 0 & \cdots & 0 & 1 & 0 & \cdots & 0 \\ 0 & 0 & \cdots & 0 & 0 & 1 & \cdots & 0 \\ \vdots & \vdots & \ddots & \vdots & \vdots & \vdots & \ddots & \vdots \end{pmatrix}, \tag{E.11}$$

where $A = \partial x_1(k+1)/\partial x_1(k)$, $B = \partial x_1(k+1)/\partial x_z(k)$, $C = \partial x_1(k+1)/\partial y_1(k)$, $D = \partial y_1(k+1)/\partial x_1(k)$, $E = \partial y_1(k+1)/\partial y_1(k)$, and $F = \partial y_1(k+1)/\partial y_{\tilde{z}}(k)$, for $z \in \{2, \tau_r\}$ and $\tilde{z} \in \{2, \tilde{\tau}_r\}$. The similarity between this matrix and the original CBM mean-field Jacobian in Equation 3.17 should be noted; new physics comes from additional, nonzero terms in the Jacobian, which may be introduced through the action of activity transmission delays or perhaps metabolic delays, as presented in the following section.

E.2.2 Bond Inhibition

We now turn our attention to the second mechanism mentioned above, wherein inhibition acts directly and selectively on bonds and not the sites themselves. One of the key findings from [129] involved the action of somatostatin-expressing (SST) inhibitory interneurons, i.e., suppression of excitatory axonal transmission by means of the GABAb presynaptic receptor. This **axo-axonic** mechanism can be modeled as a site-to-bond interaction: SST-expressing inhibitory interneurons act upon synapses inbound on excitatory pyramidal cells. Consider a pyramidal cell k with two inbound connections: one from an SST neuron j and the other from a fellow excitatory pyramidal cell i. A directed edge exists between the pair of pyramidal cells with activity transmission probability P_{ik}, and there is an axo-axonal connection from neuron j to the synapse between i and k.

In the absence of any activity, the pyramidal cell k becomes active with probability p_s given its quiescence, $z_k = 0$. If the pyramidal cell at i is active, then the cell at k becomes active with probability $p_s + P_{ik}(1-p_s)$. Thus far, there is no distinction to be made between this interaction in the EICBM and the $k_{in} = 1$ mean-field CBM. But now, let us consider an active inhibitory cell j featuring bond inhibition; if only this cell is active, then the cell at k becomes active with probability p_s, as before, since the depression of the bond $i \to k$ has no effect on spontaneous activation, which represents incoming excitation from some hidden or unidentified source. If, however, both cells at i and j are active, then cell j can veto the influence of cell i with probability v. Hence, the probability that k becomes active under these conditions is $p_s + P_{ik}(1-v)(1-p_s)$, or, in other terms, $p_s + P'_{ik}(1-p_s)$. That is, node j has the effect of changing the bond strength from P_{ik} to $P'_{ik} = (1-v)P_{ik}$. We summarize the model with the following transition rates:

$$
\begin{aligned}
&W(00 \to 1) = p_s \\
&W(01 \to 1) = p_s(1-v) \\
&W(10 \to 1) = p_s + P_{ik}(1-p_s) \\
&W(11 \to 1) = p_s(1-v) + P_{ik}(1-p_s)(1-v) + vP_{ik}p_s
\end{aligned}
\tag{E.12}
$$

The resulting mean-field approximation is

$$x_1(t+1) = x_0(t)(p_s + P_{ik}(1-p_s)(1-vy_1(t))x_1(t)) \tag{E.13}$$

where we have used t to index the iterations of the map. The form of $y_1(t)$ would be determined by the nature of SST neurons, i.e., their dynamics (e.g., tonic firing) and inputs. If $y_1(t+1) = y_0(t)(p_s + P_{ik}(1-p_s)(1-vy_1(t))y_1(t))$, as in the siCBM, then again we would find that the phase transition occurs at $P_{ik} = 1$. But as detailed in [129], SST neurons *tonically* suppress the firing of excitatory pyramidal neurons by utilizing a GABAb metabotropic transmembrane receptor and hence $y_1(t)$ might be approximated as a constant, i.e., an inhibitory analog to p_s. When $p_s = 0$, we have two fixed points, including $x_1^* = 0$, which is stable up until $P_{ik}(1 - vy_1) = 1$, where y_1 is now a constant: the location of the critical point has been shifted due to the action of the tonic inhibition.

Moreover, because the inhibitory action of SST involves an additional timescale, i.e., the timescale τ_G involved in the transit of a G-protein to a potassium channel, the states of excitatory nodes receiving SST inputs will depend on an inhibitory signal sent some time τ_G ago, unlike the action of GABAa, which acts immediately. This represents a **metabolic retardation effect**. In the mean-field approximation then, we should modify the discrete map to include these varied influences:

$$x_1(t+1) = f(x_1(t), y_1(t), y_1(t-\tau_G)), \tag{E.14}$$

which would include terms for direct excitation,$x_1(t)$, terms for GABAa inhibition, $y_1(t)$, and terms for GABAb inhibition $y_1(t-\tau_G)$. The term $y_1(t-\tau_G)$ would introduce new nonzero elements to the Jacobian and thus this model has potential for the discovery of new physics based on these metabolic delay effects.

APPENDIX F

Analysis of Somatosensory Cortex Data

Here I describe some basic features of the ten data sets from [85]. The data were collected *in vitro* from organotypic cultures of mouse somatosensory cortex using a 512-microelectrode array (MEA) with a 60 μm electrode spacing and a 20 kHz sampling rate over an hour-long recording [86, 87]. Using delayed transfer entropy (dTE), we obtain estimates for synaptic delays between identified neurons along with respective synaptic weights given as probabilities. From this information, we can infer a number of properties which may be of interest. All of the results presented in this Appendix are from aggregated data; they represent a sort of mean-field approximation of the neural network structure and so should be taken with a grain of salt. Additionally, inhibitory neurons can not be identified by TE methods, and so neuronal out-degrees do not include those of inhibitory neurons; synaptic strengths may be biased as well.

Synapses are established by two distinct mechanisms

The probability distribution of synaptic delays $P(d_{ij})$ aggregated across all 10 data sets, appeared to be convex in shape (see Figure F.1). To understand this shape, I have made the assumption that synaptic delays are reliably determined by the length of the synapse, with an identical and constant synaptic transmission velocity across all synapses. The shape of $P(d_{ij})$ then reflects the density of connections as a function of distance between

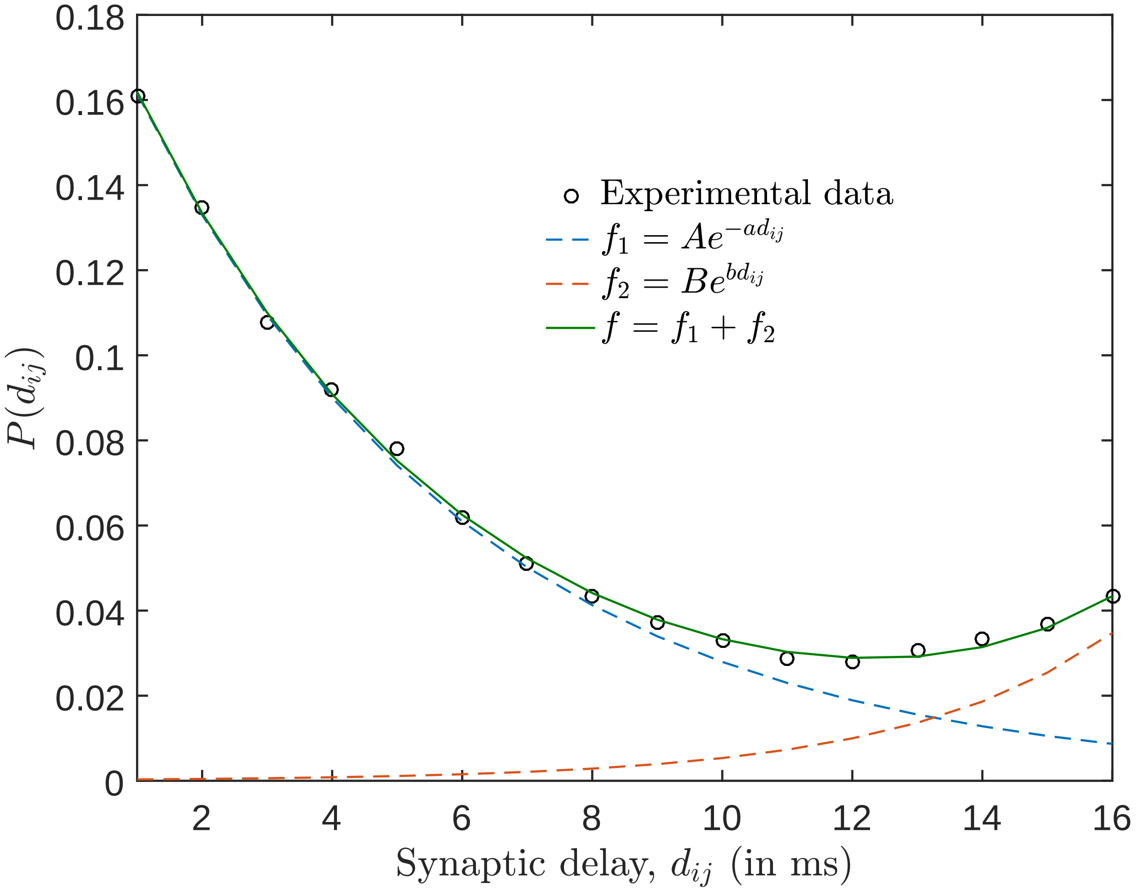

Figure F.1: The form of the synaptic delay probability distribution potentially suggests the presence of two, distinct mechanisms promoting the establishment of short- and long-ranged synaptic connections.

neurons. Indeed, $P(d_{ij})$ is well described (with $R^2 = 0.999$) by a sum of two exponential functions $f = f_1 + f_2$, where $f_1 = Ae^{-ad_{ij}}$ describes the short-ranged distribution and $f_2 = Be^{bd_{ij}}$ the long-ranged distribution, where $A = 0.196 \pm 0.005$, $a = 0.195 \pm 0.009$ ms^{-1}, $B = (2.36 \pm 2.67) \times 10^{-4}$, and $b = 0.312 \pm 0.072$ ms^{-1}, with 95% confidence intervals. Whereas short-range (short-delay) synaptic connections might correspond to dendritic connections made between nearby cells, long-range (long-delay) synaptic connections might correspond to axonal projections made to distant cells.

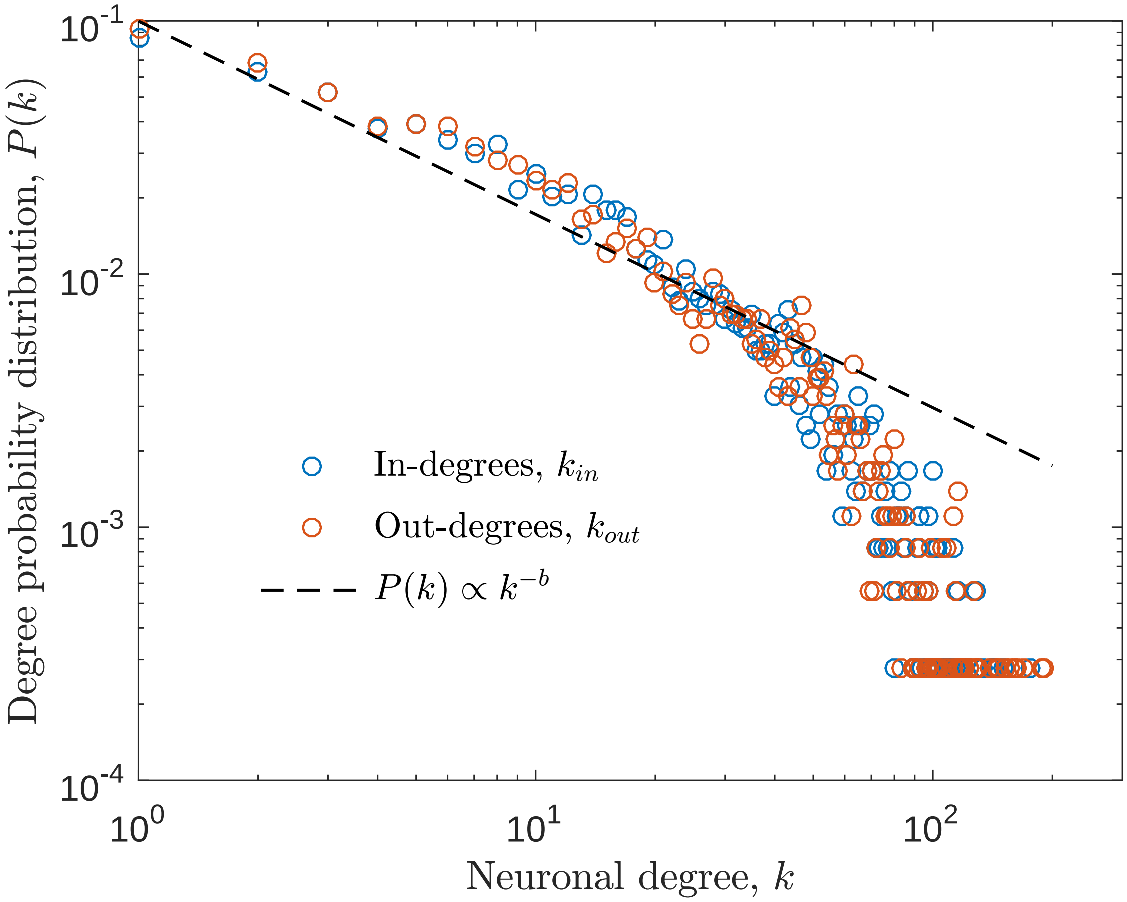

Figure F.2: Aggregated neuronal in- and out-degree distributions, excluding $k = 0$ neurons, roughly follow power-law distributions with exponent $b = -0.76 \pm 0.03$.

Neuronal in- and out-degrees are nearly identically distributed

The probability distribution of neuronal degrees k, both in-degrees and out-degrees, aggregated across all 10 data sets roughly followed a power law with exponent $b = -0.76 \pm 0.03$ (see Figure F.2). A scatter plot is used to highlight the variability of the in- and out-degrees for individual neurons (see Figure F.3).

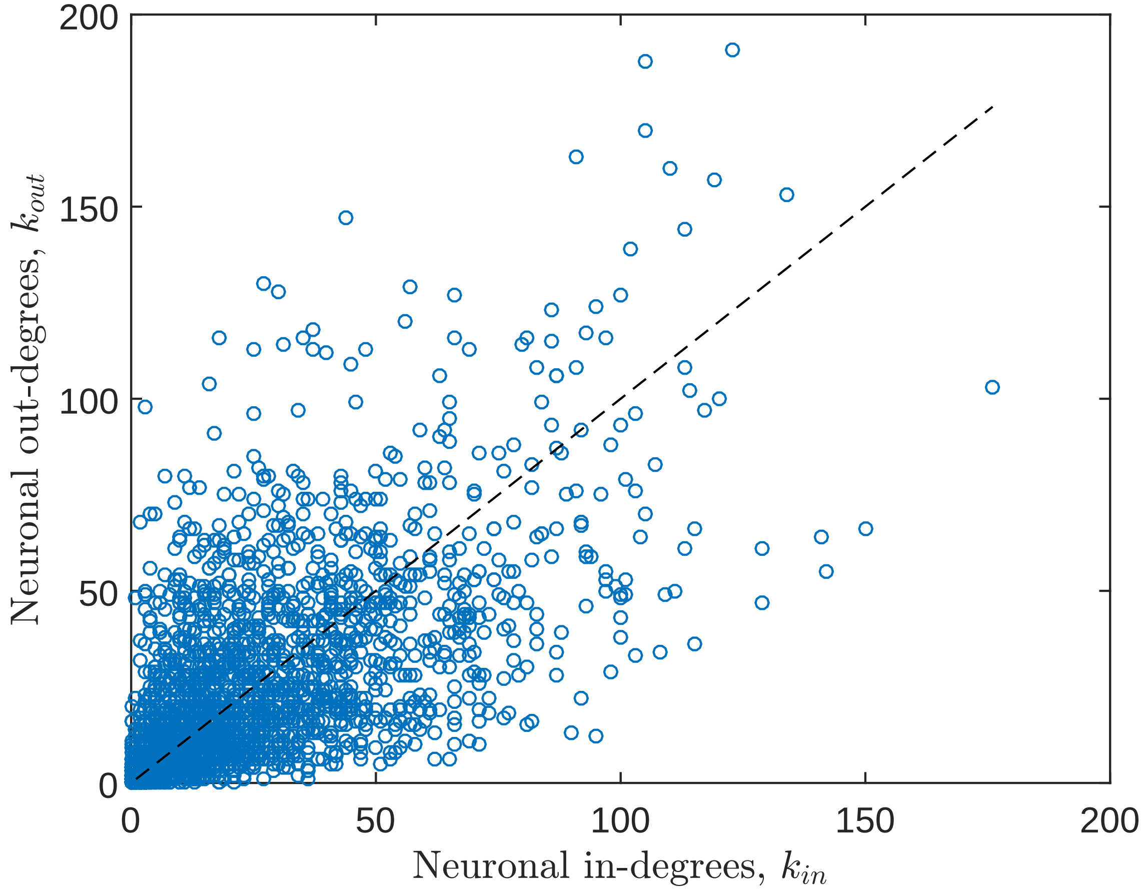

Figure F.3: Scatter plot of neuronal out-degrees versus in-degrees; each annulus represents a single neuron, with its position indicating its out- and in-degrees. The diagonal dashed line is of unity slope, serving as a guide to the eye. Annuli above the diagonal have more outgoing connections than incoming connections; the opposite is true for annuli below the diagonal.

APPENDIX G

Generation of Biologically-Inspired Networks

The following procedure has not yet been tested or used in generating networks for simulations of the CBM, however, it could be particularly useful in a generalized CBM incorporating activity transmission delays—I describe various generalized CBM's in Section E. Results from delayed transfer entropy analysis on the 512-electrode MEA data in [84] presented below have been used as a basis for this *recipe*.

The synaptic delay probability distribution is approximately a sum of exponentials: a decaying exponential at short delays and a growing exponential at long delays. The delays themselves can be interpreted as being proportional to the lengths of neuronal projections, assuming constant action potential propagation rates. Interpreting the data in this way might suggest that two different mechanisms are at play in the development of neuronal projections: one which acts at short range, promoting local connections, and another which acts at long ranges, promoting distal connections. The long-range behavior may be due to mechanisms which guide axonal projections to specific targets in the nervous system, in a process known as growth cone chemotaxis [130]. The procedure is prescribed as follows:

1. Preheat CPU to 55°C.

2. Choose a number of neurons N.

3. For each neuron, choose the in- and out-degrees k from the distribution

$$P(k) = A_k(k+1)^{-\alpha_k}, \tag{G.1}$$

   where $\alpha_k = 0.86$ from data. Pre- and post-synaptic neurons are randomly assigned, with the following normalization:

$$\sum_{k=1}^{k_{\mathsf{max}}}(k+1)^{-\alpha_k} = 1/A_k, \tag{G.2}$$

   where $A_k = 0.15$ from the data, suggesting a maximum node degree of $k_{\mathsf{max}} = 136$, which should be independent of the system size N.

4. For each connection, generate associated synaptic delays d_{ij}'s, according to the distribution

$$P(d_{ij}) = A_d(e^{-\alpha_s d_{ij}} + \rho_{\mathsf{s}} e^{\alpha_\ell d_{ij}}), \tag{G.3}$$

   where $\rho_{\mathsf{s}} = 10^{-3}$ is the relative strength of the long-ranged interactions, $\alpha_s = 0.2$ ms^{-1} is the **short-ranged connectivity exponent**, and $\alpha_\ell = 0.3$ ms^{-1} is the **long-ranged connectivity exponent**.

5. Assign connection strengths P_{ij}'s according to the activity transmission delays, i.e., according to

$$P_{ij}(d_{ij}) = A_p^{(i)} \frac{1}{d_{ij} + \tau_d}, \tag{G.4}$$

   where $\tau_d = 11$ ms and the normalization $A_p^{(i)}$ is chosen to satisfy the condition Equation 3.3 for each node i:

$$A_p^{(i)} = \kappa \left(\sum_{k=1}^{k_{\mathsf{out}}^{(i)}} \frac{1}{d_{in_i(k)} + \tau_d} \right)^{-1}. \tag{G.5}$$

Some final checks should be performed to validate results of the method, for example, scatter plots of out-degrees versus in-degrees should be checked against data and the networks can be checked for the presence of a rich club.

BIBLIOGRAPHY

[1] S. Herculano-Houzel, “The remarkable, yet not extraordinary, human brain as a scaled-up primate brain and its associated cost,” *Proceedings of the National Academy of Sciences*, vol. **109**, pp. 10661–10668, 2012.

[2] Facebook Inc., “Facebook reports first quarter 2016 results and announces proposal for new class of stock,” 2016. `http://investor.fb.com/releasedetail.cfm?ReleaseID=967167`.

[3] Pew Research Center, “6 new facts about Facebook,” 2014. `http://pewrsr.ch/1dm5NmJ`.

[4] A. L. Barabási and Z. N. Oltvai, “Network biology: understanding the cell’s functional organization,” *Nature Reviews Genetics*, vol. **5**, pp. 101–113, 2004.

[5] C. Zhou, L. Zemanová, G. Zamora, C. C. Hilgetag, and J. Kurths, “Hierarchical organization unveiled by functional connectivity in complex brain networks,” *Physical Review Letters*, vol. **97**, p. 238103, 2006.

[6] R. V. Solé and J. M. Montoya, “Complexity and fragility in ecological networks,” *Proceedings of the Royal Society of London B: Biological Sciences*, vol. **268**, pp. 2039–2045, 2001.

[7] J. F. Donges, Y. Zou, N. Marwan, and J. Kurths, "Complex networks in climate dynamics," *The European Physical Journal Special Topics*, vol. **174**, pp. 157–179, 2009.

[8] R. Albert and A. L. Barabási, "Statistical mechanics of complex networks," *Reviews of Modern Physics*, vol. **74**, pp. 47–97, 2002.

[9] P. Bak, K. Christensen, L. Danon, and T. Scanlon, "Unified scaling law for earthquakes," *Physical Review Letters*, vol. **88**, p. 178501, 2002.

[10] D. L. Turcotte and B. D. Malamud, "Landslides, forest fires, and earthquakes: examples of self-organized critical behavior," *Physica A*, vol. **340**, pp. 580–589, 2004.

[11] F. Y. Wang and Z. G. Dai, "Self-organized criticality in X-ray flares of gamma-ray-burst afterglows," *Nature Physics*, vol. **9**, pp. 465–467, 2013.

[12] S. Hergarten, "Landslides, sandpiles, and self-organized criticality," *Natural Hazards and Earth System Science*, vol. **3**, pp. 505–514, 2003.

[13] M. E. J. Newman, "Self-organized criticality, evolution, and the fossil extinction record," *Proceedings of the Royal Society of London B: Biological Sciences*, vol. **263**, pp. 1605–1610, 1996.

[14] J. M. Beggs and D. Plenz, "Neuronal avalanches in neocortical circuits," *The Journal of Neuroscience*, vol. **23**, pp. 11167–11177, 2003.

[15] H. E. Stanley, L. A. N. Amaral, P. Gopikrishnan, and V. Plerou, "Scale invariance and universality of economic fluctuations," *Physica A*, vol. **283**, pp. 31–41, 2000.

[16] H. Nishimori and G. Ortiz, *Elements of Phase Transitions and Critical Phenomena.* Oxford University Press, 2011.

[17] F. G. Zeng, Q. J. Fu, and R. Morse, "Human hearing enhanced by noise," *Brain Research*, vol. **869**, pp. 251–255, 2000.

[18] M. A. Buice and J. D. Cowan, "Field-theoretic approach to fluctuation effects in neural networks," *Physical Review E*, vol. **75**, p. 051919, 2007.

[19] R. V. Williams-García, M. Moore, J. M. Beggs, and G. Ortiz, "Quasicritical brain dynamics on a nonequilibrium Widom line," *Physical Review E*, vol. **90**, p. 062714, 2014.

[20] P. Bak, C. Tang, and K. Wiesenfeld, "Self-organized criticality: An explanation of the $1/f$ noise," *Physical Review Letters*, vol. **59**, p. 381, 1987.

[21] P. Bak, *How Nature Works: The Science of Self-Organized Criticality.* Springer, 1996.

[22] K. Christensen and N. R. Moloney, *Complexity and Criticality.* Imperial College Press, 2005.

[23] C. Haldeman and J. M. Beggs, "Critical branching captures activity in living neural networks and maximizes the number of metastable states," *Physical Review Letters*, vol. **94**, p. 058101, 2005.

[24] W. Chen, J. P. Hobbs, A. Tang, and J. M. Beggs, "A few strong connections: optimizing information retention in neuronal avalanches," *BMC Neuroscience*, vol. **11**, p. 3, 2010.

[25] N. Bertschinger and T. Natschläger, "Real-time computation at the edge of chaos in recurrent neural networks," *Neural Computation*, vol. **16**, pp. 1413–1436, 2004.

[26] L. L. Gollo, O. Kinouchi, and M. Copelli, "Single-neuron criticality optimizes analog dendritic computation," *Scientific Reports*, vol. **3**, 2013.

[27] O. Kinouchi and M. Copelli, "Optimal dynamical range of excitable networks at criticality," *Nature Physics*, vol. **2**, pp. 348–351, 2006.

[28] D. B. Larremore, W. L. Shew, and J. G. Restrepo, "Predicting criticality and dynamic range in complex networks: effects of topology," *Physical Review Letters*, vol. **106**, p. 058101, 2011.

[29] S. Pei, S. Tang, S. Yan, S. Jiang, X. Zhang, and Z. Zheng, "How to enhance the dynamic range of excitatory-inhibitory excitable networks," *Physical Review E*, vol. **86**, p. 021909, 2012.

[30] R. Publio, C. C. Ceballos, and A. C. Roque, "Dynamic range of vertebrate retina ganglion cells: Importance of active dendrites and coupling by electrical synapses," *PLoS ONE*, vol. **7**, p. e48517, 2012.

[31] K. Manchanda, A. C. Yadav, and R. Ramaswamy, "Scaling behavior in probabilistic neuronal cellular automata," *Physical Review E*, vol. **87**, p. 012704, 2013.

[32] T. S. Mosqueiro and L. P. Maia, "Optimal channel efficiency in a sensory network," *Physical Review E*, vol. **88**, p. 012712, 2013.

[33] L. Wang, P. M. Zhang, P. J. Liang, and Q. Y. H., "Enhancement of the neuronal dynamic range by proper intensities of channel noise," *Chinese Physics Letters*, vol. **30**, p. 070506, 2013.

[34] L. de Arcangelis and H. J. Herrmann, "Learning as a phenomenon occurring in a critical state," *Proceedings of the National Academy of Sciences*, vol. **107**, p. 3977, 2010.

[35] M. O. Magnasco, O. Piro, and G. A. Cecchi, "Self-tuned critical anti-Hebbian networks," *Physical Review Letters*, vol. **102**, p. 258102, 2009.

[36] W. L. Shew, H. Yang, T. Petermann, R. Roy, and D. Plenz, "Neuronal avalanches imply maximum dynamic range in cortical networks at criticality," *The Journal of Neuroscience*, vol. **29**, pp. 15595–15600, 2009.

[37] W. L. Shew, H. Yang, S. Yu, R. Roy, and D. Plenz, "Information capacity and transmission are maximized in balanced cortical networks with neuronal avalanches," *The Journal of Neuroscience*, vol. **31**, pp. 55–63, 2011.

[38] G. Solovey, K. J. Miller, J. G. Ojemann, M. O. Magnasco, and G. A. Cecchi, "Self-regulated dynamical criticality in human ECoG," *Frontiers in Integrative Neuroscience*, vol. **6**, p. 44, 2012.

[39] J. M. Beggs, "The criticality hypothesis: how local cortical networks might optimize information processing," *Philosophical Transactions of the Royal Society of London A: Mathematical, Physical and Engineering Sciences*, vol. **366**, pp. 329–343, 2008.

[40] D. Hsu and J. M. Beggs, "Neuronal avalanches and criticality: A dynamical model for homeostasis," *Neurocomputing*, vol. **69**, p. 1134, 2006.

[41] B. A. Pearlmutter and C. J. Houghton, "A new hypothesis for sleep: Tuning for criticality," *Neural Computation*, vol. **21**, p. 1622, 2009.

[42] V. Priesemann, M. Valderrama, M. Wibral, and M. L. V. Quyen, "Neuronal avalanches differ from wakefulness to deep sleep–evidence from intracranial depth recordings in humans," *PLoS Computational Biology*, vol. **9**, p. e1002985, 2013.

[43] L. de Arcangelis, F. Lombardi, and H. J. Herrmann, "Criticality in the brain," *Journal of Statistical Mechanics*, vol. **2014**, p. P03026, 2014.

[44] M. Rybarsh and S. Bornholdt, “Avalanches in self-organized critical neural networks: A minimal model for the neural SOC universality class,” *PLoS ONE*, vol. **9**, p. e93090, 2014.

[45] C. Bédard, H. Kroeger, and A. Destexhe, “Does the 1/f frequency scaling of brain signals reflect self-organized critical states?,” *Physical Review Letters*, vol. **97**, p. 118102, 2006.

[46] J. Touboul and A. Destexhe, “Can power-law scaling and neuronal avalanches arise from stochastic dynamics?,” *PLoS ONE*, vol. **5**, p. e8982, 2010.

[47] T. L. Ribeiro, S. Ribeiro, H. Belchior, F. Caixeta, and M. Copelli, “Undersampled critical branching processes on small-world and random networks fail to reproduce the statistics of spike avalanches,” *PloS ONE*, vol. **9**, p. e94992, 2014.

[48] V. Priesemann, M. Wibral, M. Valderrama, R. Pröpper, M. L. V. Quyen, T. Geisel, J. Triesch, D. Nikolic, and M. H. J. Munk, “Spike avalanches in vivo suggest a driven, slightly subcritical brain state,” *Frontiers in Systems Neuroscience*, vol. **8**, 2014.

[49] A. Clauset, C. R. Shalizi, and M. E. J. Newman, “Power-law distributions in empirical data,” *SIAM Review*, vol. **51**, pp. 661–703, 2009.

[50] M. P. H. Stumpf and M. A. Porter, “Critical truths about power laws,” *Science*, vol. **335**, pp. 665–666, 2012.

[51] H. J. Jensen, *Self-Organized Criticality: Emergent Complex Behavior in Physical and Biological Systems.* Cambridge University Press, 1998.

[52] K. Tillisch, J. Labus, L. Kilpatrick, Z. Jiang, J. Stains, B. Ebrat, D. Guyonnet, S. Legrain-Raspaud, B. Trotin, B. Naliboff, and E. A. Mayer, “Consumption of

fermented milk product with probiotic modulates brain activity," *Gastroenterology*, vol. **144**, pp. 1394–1401, 2013.

[53] L. Onsager, "Crystal statistics. I. A two-dimensional model with an order-disorder transition," *Physical Review*, vol. **65**, p. 117, 1944.

[54] M. Henkel, H. Hinrichsen, and S. Lübeck, *Non-Equilibrium Phase Transitions.* Springer, 2008.

[55] H. K. Janssen, "On the nonequilibrium phase transition in reaction-diffusion systems with an absorbing stationary state," *Zeitschrift für Physik B Condensed Matter*, vol. **42**, pp. 151–154, 1981.

[56] P. Grassberger, "On phase transitions in Schlögl's second model," *Zeitschrift für Physik B Condensed Matter*, vol. **47**, pp. 365–374, 1982.

[57] L. D. Landau, "On the theory of phase transitions. I.," *Zh. Eksp. Teor. Fiz.*, vol. **11**, pp. 19–32, 1937.

[58] R. V. Williams-García, J. M. Beggs, and G. Ortiz, "Unveiling causal activity of complex networks," *arXiv preprint:1603.05659*, 2016.

[59] D. Dhar and R. Ramaswamy, "Exactly solved model of self-organized critical phenomena," *Physical Review Letters*, vol. **63**, no. 16, p. 1659, 1989.

[60] S. Pajevic and D. Plenz, "Efficient network reconstruction from dynamical cascades identifies small-world topology of neuronal avalanches," *PLoS Computational Biology*, vol. **5**, p. e1000271, 2009.

[61] D. B. Larremore, M. Y. Carpenter, E. Ott, and J. G. Restrepo, "Statistical properties of avalanches in networks," *Physical Review E*, vol. **85**, p. 066131, 2012.

[62] A. Vespignani and S. Zapperi, “How self-organized criticality works: A unified mean-field picture,” *Physical Review E*, vol. **57**, p. 6345, 1998.

[63] J. P. Sethna, K. A. Dahmen, and C. R. Myers, “Crackling noise,” *Nature*, vol. **410**, pp. 242–250, 2001.

[64] A. Levina, J. M. Herrmann, and T. Geisel, “Dynamical synapses causing self-organized criticality in neural networks,” *Nature Physics*, vol. **3**, pp. 857–860, 2007.

[65] T. E. Harris, *The Theory of Branching Processes.* Dover Publications, 1989.

[66] K. Christensen and Z. Olami, “Sandpile models with and without an underlying spatial structure,” *Physical Review E*, vol. **48**, p. 3361, 1993.

[67] A. Deutsch and S. Dormann, *Cellular Automaton Modeling of Biological Pattern Formation: Characterization, Applications, and Analysis.* Birkhäuser, 2005.

[68] M. Girvan, D. S. Callaway, M. E. J. Newman, and S. H. Strogatz, “Simple model of epidemics with pathogen mutation,” *Physical Review E*, vol. **65**, p. 031915, 2002.

[69] F. Rozenblit and M. Copelli, “Collective oscillations of excitable elements: order parameters, bistability and the role of stochasticity,” *Journal of Statistical Mechanics: Theory and Experiment*, vol. **2011**, p. P01012, 2011.

[70] R. Curtu and B. Ermentrout, “Oscillations in a refractory neural net,” *Journal of Mathematical Biology*, vol. **43**, pp. 81–100, 2001.

[71] N. Friedman, S. Ito, B. A. W. Brinkman, M. Shimono, R. E. L. DeVille, K. A. Dahmen, J. M. Beggs, and T. C. Butler, “Universal critical dynamics in high resolution neuronal avalanche data,” *Physical Review Letters*, vol. **108**, p. 208102, 2012.

[72] S. Papanikolaou, F. Bohn, R. L. Sommer, G. Durin, S. Zapperi, and J. P. Sethna, "Universality beyond power laws and the average avalanche shape," *Nature Physics*, vol. **7**, pp. 316–320, 2011.

[73] L. Xu, P. Kumar, S. V. Buldyrev, S. H. Chen, P. H. Poole, F. Sciortino, and H. E. Stanley, "Relation between the Widom line and the dynamic crossover in systems with a liquid-liquid phase transition," *Proceedings of the National Academy of Sciences*, vol. **102**, p. 16558, 2005.

[74] A. Zador, "Impact of synaptic unreliability on the information transmitted by spiking neurons," *Journal of Neurophysiology*, vol. **79**, pp. 1219–1229, 1998.

[75] H. Matsuda, K. Kudo, R. Nakamura, O. Yamakawa, and T. Murata, "Mutual information of Ising systems," *International Journal of Theoretical Physics*, vol. **35**, pp. 839–845, 1996.

[76] R. T. Wicks, S. C. Chapman, and R. O. Dendy, "Mutual information as a tool for identifying phase transitions in dynamical complex systems with limited data," *Physical Review E*, vol. **75**, p. 051125, 2007.

[77] C. Shannon and W. Weaver, *A Mathematical Theory of Communication.* University of Illinois Press, 1948.

[78] W. L. Shew, W. P. Clawson, J. Pobst, Y. Karimipanah, N. C. Wright, and R. Wessel, "Adaptation to sensory input tunes visual cortex to criticality," *Nature Physics*, vol. **11**, p. 659, 2015.

[79] J. Pearl, *Causality.* Cambridge University Press, 2009.

[80] G. Rebane and J. Pearl, "The recovery of causal poly-trees from statistical data," (Seattle, Washington), pp. 222–228, Proceedings of the Workshop on Uncertainty in Artificial Intelligence, 1987.

[81] F. James, *Statistical Methods in Experimental Physics.* World Scientific, 2006.

[82] S. Ito, M. E. Hansen, R. Heiland, A. Lumsdaine, A. M. Litke, and J. M. Beggs, "Extending transfer entropy improves identification of effective connectivity in a spiking cortical network model," *PloS ONE*, vol. **6**, p. e27431, 2011.

[83] M. Wibral, N. Pampu, V. Priesemann, F. Siebenhühner, H. Seiwert, M. Lindner, J. T. Lizier, and R. Vicente, "Measuring information-transfer delays," *PloS ONE*, vol. **8**, p. e55809, 2013.

[84] S. Nigam, M. Shimono, S. Ito, F. C. Yeh, N. Timme, M. Myroshnychenko, C. C. Lapish, Z. Tosi, P. Hottowy, W. C. Smith, S. C. Masmanidis, A. M. Litke, O. Sporns, and J. M. Beggs, "Rich-club organization in effective connectivity among cortical neurons," *The Journal of Neuroscience*, vol. **36**, p. 670, 2016.

[85] S. Ito, F. C. Yeh, N. M. Timme, P. Hottowy, A. M. Litke, and J. M. Beggs, "Spontaneous spiking activity of hundreds of neurons in mouse somatosensory cortex slice cultures recorded using a dense 512 electrode array," 2016. `https://crcns.org/data-sets/ssc/ssc-3/about-ssc-3`.

[86] A. M. Litke, N. Bezayiff, E. J. Chichilnisky, W. Cunningham, W. Dabrowski, A. A. Grillo, M. Grivich, P. Grybos, P. Hottowy, S. Kachiguine, R. S. Kalmar, K. Mathieson, D. Petrusca, M. Rahman, and A. Sher, "What does the eye tell the brain?," *IEEE Transactions on Nuclear Science*, vol. **51**, p. 1434, 2004.

[87] S. Ito, F. C. Yeh, E. Hiolski, P. Rydygier, D. E. Gunning, P. Hottowy, N. M. Timme, A. M. Litke, and J. M. Beggs, "Large-scale, high-resolution multielectrode-array recording depicts functional network differences of cortical and hippocampal cultures," *PloS ONE*, vol. **9**, p. e105324, 2014.

[88] A. V. Oppenheim, R. W. Schafer, and J. R. Buck, *Discrete-Time Signal Processing.* Prentice Hall, 1989.

[89] O. Vernet and L. Markenzon, "Hamiltonian problems for reducible flowgraphs," pp. 264–267, Proceedings of the 17th International Conference of the Chilean Computer Science Society.

[90] T. H. Cormen, C. E. Leiserson, R. L. Rivest, and C. Stein, *Introduction to Algorithms.* MIT Press and McGraw-Hill, 2001.

[91] M. Chiappalone, A. Vato, M. B. Tedesco, M. Marcoli, F. Davide, and S. Martinoia, "Networks of neurons coupled to microelectrode arrays: a neuronal sensory system for pharmacological applications," *Biosensors and Bioelectronics*, vol. **18**, pp. 627–634, 2003.

[92] I. Vajda, J. van Pelt, P. Wolters, M. Chiappalone, S. Martinoia, E. van Someren, and A. van Ooyen, "Low-frequency stimulation induces stable transitions in stereotypical activity in cortical networks," *Biophysical Journal*, vol. **94**, pp. 5028–5039, 2008.

[93] D. E. Gunning, J. M. Beggs, W. Dabrowski, P. Hottowy, C. J. Kenney, A. Sher, A. M. Litke, and K. Mathieson, "Dense arrays of micro-needles for recording and electrical stimulation of neural activity in acute brain slices," *Journal of Neural Engineering*, vol. **10**, p. 016007, 2013.

[94] D. A. Wagenaar, R. Madhavan, J. Pine, and S. M. Potter, "Controlling bursting in cortical cultures with closed-loop multi-electrode stimulation," *The Journal of Neuroscience*, vol. **25**, pp. 680–688, 2005.

[95] A. Mazzoni, F. D. Broccard, E. García-Pérez, P. Bonifazi, M. E. Ruaro, and V. Torre, "On the dynamics of the spontaneous activity in neuronal networks," *PLoS ONE*, vol. **2**, p. e439, 2007.

[96] V. Pasquale, P. Massobrio, L. L. Bologna, M. Chiappalone, and S. Martinoia, "Self-organization and neuronal avalanches in networks of dissociated cortical neurons," *Neuroscience*, vol. **153**, pp. 1354–1369, 2008.

[97] G. Hahn, T. Petermann, M. N. Havenith, S. Yu, W. Singer, D. Plenz, and D. Nikolić, "Neuronal avalanches in spontaneous activity in vivo," *Journal of Neurophysiology*, vol. **104**, pp. 3312–3322, 2010.

[98] T. L. Ribeiro, M. Copelli, F. Caixeta, H. Belchior, D. R. Chialvo, M. A. L. Nicolelis, and S. Ribeiro, "Spike avalanches exhibit universal dynamics across the sleep-wake cycle," *PloS ONE*, vol. **5**, p. e14129, 2010.

[99] F. Lombardi, H. J. Herrmann, C. Perrone-Capano, D. Plenz, and L. de Arcangelis, "Balance between excitation and inhibition controls the temporal organization of neuronal avalanches," *Physical Review Letters*, vol. **108**, p. 228703, 2012.

[100] F. N. Quandt and F. A. Davis, "Action potential refractory period in axonal demyelination: a computer simulation," *Biological Cybernetics*, vol. **67**, pp. 545–552, 1992.

[101] P. A. Felts, T. A. Baker, and K. J. Smith, "Conduction in segmentally demyelinated mammalian central axons," *The Journal of Neuroscience*, vol. **17**, pp. 7267–7277, 1997.

[102] Z. H. Luo, J. X. Chen, Y. M. Huang, H. Q. Yang, J. Q. Lin, H. Li, and S. S. Xie, "Characterization of signal conductance along demyelinated axons by action-potential-encoded second harmonic generation," *Journal of Innovative Optical Health Sciences*, vol. **7**, p. 1330003, 2014.

[103] B. J. Kelley and M. Rodriguez, "Seizures in patients with multiple sclerosis," *CNS Drugs*, vol. **23**, pp. 805–815, 2009.

[104] R. Dawkins and W. F. Sewell, "Afferent synaptic transmission in a hair cell organ: pharmacological and physiological analysis of the role of the extended refractory period," *Journal of Neurophysiology*, vol. **92**, pp. 1105–1115, 2004.

[105] A. Bragin, J. Engel, C. L. Wilson, I. Fried, and G. W. Mathern, "Hippocampal and entorhinal cortex high-frequency oscillations (100–500 Hz) in human epileptic brain and in kainic acid-treated rats with chronic seizures," *Epilepsia*, vol. **40**, pp. 127–137, 1999.

[106] W. van Drongelen, H. C. Lee, M. Hereld, Z. Chen, F. P. Elsen, and R. L. Stevens, "Emergent epileptiform activity in neural networks with weak excitatory synapses," *IEEE Transactions on Neural Systems and Rehabilitation Engineering*, vol. **13**, pp. 236–241, 2005.

[107] P. Jiruska, M. de Curtis, J. G. R. Jefferys, C. A. Schevon, S. J. Schiff, and K. Schindler, "Synchronization and desynchronization in epilepsy: controversies and hypotheses," *The Journal of Physiology*, vol. **591**, pp. 787–797, 2013.

[108] S. Bornholdt and T. Röhl, "Self-organized critical neural networks," *Physical Review E*, vol. **67**, p. 066118, 2003.

[109] A. Lazar, G. Pipa, and J. Triesch, "SORN: a self-organizing recurrent neural network," *Frontiers in Computational Neuroscience*, vol. **3**, p. 23, 2009.

[110] Z. Tosi and J. M. Beggs, "Building a microcircuit from scratch: Introducing the first complete self-organizing cortical model," unpublished.

[111] F. Vazquez, J. A. Bonachela, C. López, and M. A. Muñoz, "Temporal Griffiths phases," *Physical Review Letters*, vol. **106**, p. 235702, 2011.

[112] P. Moretti and M. A. Muñoz, "Griffiths phases and the stretching of criticality in brain networks," *Nature Communications*, vol. **4**, 2013.

[113] R. Zwanzig, "Dynamical disorder: Passage through a fluctuating bottleneck," *The Journal of Chemical Physics*, vol. **97**, p. 3587, 1992.

[114] M. Mézard and A. Montanari, *Information, physics, and computation.* Oxford University Press, 2009.

[115] D. Plenz and H. G. Schuster, *Criticality in Neural Systems.* Wiley Weinheim, 2014.

[116] T. F. Freund and G. Buzsáki, "Interneurons of the hippocampus," *Hippocampus*, vol. **6**, p. 347, 1996.

[117] H. Hu, J. Gan, and P. Jonas, "Fast-spiking, parvalbumin$^+$ GABAergic interneurons: From cellular design to microcircuit function," *Science*, vol. **345**, p. 1255263, 2014.

[118] P. Barthó, H. Hirase, L. Monconduit, M. Zugaro, K. D. Harris, and G. Buzsáki, "Characterization of neocortical principal cells and interneurons by network interactions and extracellular features," *Journal of Neurophysiology*, vol. **92**, p. 600, 2004.

[119] G. Winterer and D. R. Weinberger, "Genes, dopamine, and cortical signal-to-noise ratio in schizophrenia," *TRENDS in Neurosciences*, vol. **27**, p. 683, 2004.

[120] E. T. Rolls, M. Loh, G. Deco, and G. Winterer, "Computational models of schizophrenia and dopamine modulation in the prefrontal cortex," *Nature Reviews Neuroscience*, vol. **9**, p. e696, 2008.

[121] F. Weber, S. Chung, K. T. Beier, M. Xu, L. Luo, and Y. Dan, "Control of REM sleep by ventral medulla GABAergic neurons," *Nature*, vol. **526**, p. 435, 2015.

[122] M. Okun, N. A. Steinmetz, L. Cossell, M. F. Iacaruso, H. Ko, P. Barthó, T. Moore, S. B. Hofer, T. D. Mrsic-Flogel, M. Carandini, and K. D. Harris, "Diverse coupling of neurons to populations in sensory cortex," *Nature*, vol. **521**, p. 511, 2015.

[123] R. M. Anderson and R. M. May, "Population biology of infectious diseases: Part I," *Nature*, vol. **280**, p. 361, 1979.

[124] J. Ratkiewicz, M. D. Conover, M. Meiss, B. Gonçalves, S. Patil, A. Flammini, and F. Menczer, "Truthy: mapping the spread of astroturf in microblog streams," (New York, New York), p. 249, Proceedings of the 20th international conference companion on world wide web, 2011.

[125] B. R. Hunt and E. Ott, "Defining chaos," *Chaos*, vol. **25**, p. 097618, 2015.

[126] C. W. Shin and S. Kim, "Self-organized criticality and scale-free properties in emergent functional neural networks," *Physical Review E*, vol. **74**, p. 045101, 2006.

[127] S. S. Poil, R. Hardstone, H. D. Mansvelder, and K. Linkenkaer-Hansen, "Critical-state dynamics of avalanches and oscillations jointly emerge from balanced excitation/inhibition in neuronal networks," *The Journal of Neuroscience*, vol. **32**, p. 9817, 2012.

[128] N. Brunel, “Dynamics of sparsely connected networks of excitatory and inhibitory spiking neurons,” *Journal of Computational Neuroscience*, vol. **8**, p. 183, 2000.

[129] J. Urban-Ciecko, E. E. Fanselow, and A. L. Barth, “Neocortical somatostatin neurons reversibly silence excitatory transmission via GABAb receptors,” *Current Biology*, vol. **25**, p. 722, 2015.

[130] D. Mortimer, T. Fothergill, Z. Pujic, L. J. Richards, and G. J. Goodhill, “Growth cone chemotaxis,” *Trends in Neurosciences*, vol. **31**, pp. 90–98, 2008.

Curriculum Vitae

Rashid V. Williams-García
✉ rwgarcia@indiana.edu

Research Interests

- nonequilibrium statistical physics
- neural networks
- critical phenomena
- complex systems

Professional Affiliations

The American Physical Society. 2014–*present*

Education

Doctor of Philosophy, Physics, *Indiana University Bloomington*. 2008–2016

Bachelor of Science, Physics, *University of California Los Angeles*. 2003–2006

Doctoral Thesis

title: *Phase Transitions in Living Neural Networks*

advisors: Prof. John M. Beggs and Prof. Gerardo Ortiz

Research

Postdoctoral

Postdoctoral Scholar, *University of Pittsburgh*, 2016–*present*
Prof. G. Bard Ermentrout, Department of Mathematics,
Prof. Nathan N. Urban, Department of Neurobiology.

Graduate

Research Assistant, *University of Indiana Bloomington*, 2012–2016
Prof. Gerardo Ortiz, Department of Physics.

Research Assistant, *University of Indiana Bloomington*, 2009–2016
Prof. John M. Beggs, Department of Physics.

Post-Baccalaureate

Research Assistant, *University of California Los Angeles*, 2005–2008
Prof. Dolores Bozovic, Department of Physics & Astronomy.

Undergraduate

Research Assistant, *University of California Los Angeles*, 2005–2006
Prof. George Grüner, Department of Physics & Astronomy.

Research Assistant, *University of California Los Angeles*, 2004–2005
Prof. James Rosenzweig, Department of Physics & Astronomy.

Awards and Honors

Training in the Neurobiology of Neurological Disease T32, 2016
University of Pittsburgh, National Institutes of Health.

Grand-in-Aid of Doctoral Research, *Indiana University Bloomington*, 2015
The University Graduate School.

McCormick Science Grant, *Indiana University Bloomington*, 2015
College of Arts & Sciences.

Earl Studevant Graduate Fellowship, *Indiana University Bloomington*, 2014
Department of Physics.

Lilly Biocomplexity Fellowship, *Indiana University Bloomington*, 2009–2010
Biocomplexity Institute.

Graduate Scholars Fellowship, *Indiana University Bloomington*, 2008
The University Graduate School.

Post-Baccalaureate Research & Education Program, 2006-2008
University of California Los Angeles, National Institutes of Health.

Dean's Honors List, *University of California Los Angeles*, 2006
College of Letters & Science.

Fellows Award, *University of California Los Angeles*, 2006
Center for Academic & Research Experience.

Programming

- MATLAB
- C/C++
- TORQUE
- Mathematica
- Bash

Languages

English: C2 *Fluent*

Spanish: C1 *Native speaker*

German: A2

Publications

[1] R. V. Williams-García, J. M. Beggs, and G. Ortiz, "Unveiling causal activity of complex networks," *arXiv preprint:1603.05659*, 2016.

[2] R. V. Williams-García, M. Moore, J. M. Beggs, and G. Ortiz, "Quasicritical brain dynamics on a nonequilibrium Widom line," *Physical Review E*, vol. 90, p. 062714, 2014.

Posters

Criticality in Biology, *Quasicriticality and Optimal Brain Dynamics*, Dresden, Germany. Apr. 2015

Dynamics Days XXXIV, *Quasicriticality and Optimal Brain Dynamics*, Houston, Texas. Jan. 2015

Annual Biomedical Research Conference for Minority Students, *Overstimulation Recovery in Bullfrog Hair Cells*, Austin, Texas. Nov. 2007

Teaching

Grader: Computational Physics, *University of Indiana Bloomington.* 2014

Associate Instructor: General Physics I/II, *University of Indiana Bloomington.* 2010–2014

Associate Instructor: Physics for Elementary Teachers, *University of Indiana Bloomington.* 2009–2010

Outreach

Mentor: Groups Program STEM Initiative, *Indiana University Bloomington.* 2012–2014

Volunteer: Physics Department Open House, *Indiana University Bloomington.* 2008–2013

Mentor: URC-CARE Research Mentorship Program, *University of California Los Angeles.* 2007–2008

Vice President: Society of Physics Students, *University of California Los Angeles.* 2005